UNIVERSITY OF OKLAHOMA

GRADUATE COLLEGE

CHARACTERIZATION OF THE PROTEIN-PROTEIN INTERACTIONS OF THE TYPE-II TOXIN-ANTITOXIN SYSTEM PARDE1 FROM *PSEUDOMONAS AERUGINOSA*

A DISSERTATION

SUBMITTED TO THE GRADUATE FACULTY

in partial fulfillment of the requirements for the

Degree of

DOCTOR OF PHILOSOPHY

By

KEVIN SNEAD
Norman, Oklahoma
2023

CHARACTERIZATION OF THE PROTEIN-PROTEIN INTERACTIONS OF THE TYPE-II TOXIN-ANTITOXIN SYSTEM PARDE1 FROM *PSEUDOMONAS AERUGINOSA*

A DISSERTATION APPROVED FOR THE

DEPARTMENT OF CHEMISTRY AND BIOCHEMISTRY

BY THE COMMITTEE CONSISTING OF

Dr. Christina Bourne, Chair

Dr. Ann West

Dr. Rakhi Rajan

Dr. Handan Acar

Table of Contents

List of Figures

List of Tables

List of Abbreviations

TA	toxin-antitoxin
FTIR	Fourier-transform infrared
BLI	biolayer interferometry
SPR	surface plasmon resonance
ITC	isothermal titration calorimetry
mCh	fluorescent protein mCherry
BACTH	bacterial two-hybrid
K_d	equilibrium constant of dissociation
EDF	extracellular death factor
PaParDE	*Pseudomonas aeruginosa* ParDE
EcParDE	*E. coli* ParDE
MtParDE	*Mycobacterium tuberculosis* ParDE
VcParDE	*Vibrio cholerae* ParDE
CcParDE	*Caulobacter crescentus* ParDE
MoParDE	*Mesorhizobium opportunistum* ParDE
PPI	protein-protein interaction

Abstract

The emergence of multidrug-resistant bacteria has led to an ever-growing antibiotic resistance crisis. To combat this growing crisis, new strategies for controlling bacterial cell growth must be developed. An underdeveloped target for new antimicrobial therapeutics are toxin-antitoxin (TA) systems. TA systems are widely dispersed genetic operons in prokaryotes which consist of a non-secreted protein (toxin) which targets essential metabolic enzymes causing cell death. The toxin's cellular toxicity is neutralized by its cognate antitoxin (RNA or protein). In the case of type-II TA systems, the toxin protein is neutralized by directly binding to a protein antitoxin forming a toxin-antitoxin complex. The work presented within this dissertation aims to address several gaps in understanding how the protein-protein interactions of type-II TA systems are formed and maintained, with long term goals of targeting these protein-protein interactions to develop new means to control bacterial cell growth. This work focuses on the ParDE1 TA system from *Pseudomonas aeruginosa*, composed of the ParE toxin protein which targets DNA Gyrase.

Chapter II of this work utilized a combination of biochemical and biophysical techniques to characterize the protein-protein interactions of the chromosomally-encoded ParDE1 TA system from *Pseudomonas aeruginosa*. Antitoxin residues involved in the ParD1-ParE1 toxin-antitoxin interface were selected based on structural data from a ParDE1 complex structure solved by X-ray crystallography, and mutated to alanine (alanine-scanning) by site-directed mutagenesis to identify any "hot-spot" residues which significantly impact the protein-protein interaction. The alanine-scanning revealed an antitoxin residue (Ile68) which when mutated to alanine significantly decreases the equilibrium constant of dissociation (K_d) from 152 pM to 626 nM. This decrease in binding affinity was caused by a significantly increased dissociation rate of the I68A mutant relative to the wild-type interaction. The decrease in binding affinity of the I68A mutant coincided with a change in secondary-structure of the ParDE1 complex structure as measured by Fourier-Transform Infrared Spectroscopy (FTIR), which we contribute to a change in the disorder-to-order transition of the C-terminal alpha-helix of ParD. An *in vitro* protease degradation assay using the AAA+ protease Lon showed that the reduced binding affinity of the I68A mutant resulted in increased levels of antitoxin degradation relative to the wild-type ParD1 in the presence of ParE1.

Chapter III of this work investigated an identified instability of the ParD antitoxin from the ParDE1 TA system from *Pseudomonas aeruginosa*. We identified that purified ParD1 protein is degraded in a specific and reproduceable manner. The degradation showed a temperature-dependent relationship, with increasing amounts of degradation observed in protein stored at room temperature or incubated at 37°C relative to samples stored at 4°C. We tested a variety of different conditions to identify potential means to prevent degradation of ParD1. Common protease inhibitors were screened to prevent degradation by cellular proteases, while sodium azide was tested to ensure degradation was not caused by bacterial or fungal contamination. A single condition composed of a commercially available protease inhibitor cocktail supplemented with the metal-chelating compound EDTA was shown to prevent degradation of ParD1. A top-down mass spectrometry approach was utilized to characterize the degradation products of ParD1, and to identify any contaminating proteases. Direct infusion of undegraded ParD1 identified a mixture of monomeric and dimeric antitoxin, with no appreciable amounts of

contaminating proteins detected. When degraded ParD1 protein was tested, a series of ParD1 peptides were identified with masses corresponding to the N-terminus of ParD1 with cleavage occurring in a glutamine-rich region in alpha-helix 2 of ParD1.

Chapter IV of this work was performed to identify ways to disrupt the protein-protein interaction of the ParDE1 TA system from *Pseudomonas aeruginosa*. In order to determine the most critical regions of the ParDE1 protein-protein interface, we screened ParD1-derived peptides to determine the minimal antitoxin unit required for toxin binding. Various lengths of the ParD1 antitoxin corresponding to different parts of the toxin-binding domain were screened in a bacterial two-hybrid (BACTH) assay to determine their binding to ParE1 *in vivo*. The BATCH assay indicated that peptides corresponding to the C-terminal alpha-helix of ParD1 were sufficient for binding to ParE1 *in vivo*. These interactions were validated and quantified *in vitro* using biolayer interferometry of purified ParD1 peptides fused to the fluorescent protein mCherry. This work, in combination with the work performed in chapter II, indicates that the ParD1 residues 62-75 represent the minimal antitoxin unit required to bind to ParE1. The ParE1 surface area corresponding to the binding interface of this portion of ParD1 was used as the search box for *in silico* docking peptidomemetic compounds to identify potential protein-protein interaction inhibitors.

Overall, this work provides insights into the protein-protein interactions of type-II TA systems, providing evidence that despite the very strong protein-protein interactions, certain “hot-spots” significantly contribute to the overall interaction, and that the full-length toxin-binding domain of the antitoxin is not required for toxin binding. These results have identified a minimal antitoxin unit required for binding, which has provided a rationale for *in silico* protein-protein interaction inhibitor screening.

Chapter I

Protein-Protein Interactions as Drug Targets

Upon completion of the human genome project, it was suggested that complexity of life is not defined by the number of genes in an organism's genome.[1] Complexity is instead determined by the number of physiologically relevant protein-protein interactions making up the "interactome," the global network of all protein-protein interactions in an organism.[1] These protein-protein interactions are divided into protein-interaction networks (PINs) on local levels that contribute to normal cellular physiology.

Protein interaction networks are involved in vital cellular processes such as signal transduction, differentiation, and apoptosis.[1,2] Disruption of these protein interaction networks have been linked to various diseases. One of the most commonly studied protein interaction networks is the p53, tumor suppression pathway. Mutations in the tumor suppression protein, p53 have been identified in >50% of all tumors.[3] Mutations of p53 have been implicated in disruption of p53's ability to bind DNA or to other proteins within the tumor suppression pathway.[3] Many mutant forms of p53 are unable to bind to the apoptosis-stimulating protein (ASPP2), resulting in ASPP2 being unable to promote cellular apoptosis leading to tumor formation.[3] The implication of the importance of protein-protein interactions in various disease states have led to the idea of targeting protein-protein interactions as novel therapeutic methods.[4]

A common method in studying of protein-protein interactions is the so called "hotspot" approach. Protein-protein interaction hotspots are defined as small regions or single amino acids that significantly contribute to free energy of the greater protein-protein interface.[2] When mutations occur in these "hotspot" regions, significant weakening of the interface is observed relative to other mutations along the protein-protein interface. Hotspot regions are usually identified through mutation of amino acids along the protein-protein interface through random mutagenesis or alanine scanning.[2] These hotspots serve as potential targets for protein-protein inhibitors that would disrupt these "hotspot" interactions and inhibit the formation of the native protein-protein interaction. Several biochemical and biophysical techniques have been developed to identify and study protein-protein interactions, including surface plasmon resonance (SPR), isothermal titration calorimetry (ITC), biolayer interferometry (BLI), bacterial two-hybrid assays (BACTH), and many more.[2,5]

One of the biggest issues in developing protein-protein interaction inhibitors as drug targets is initial hit detection. Protein-protein interactions are made up of extensive solvent-exposed surfaces with unique topologies, which are unlike the well-defined enzyme binding pockets that are commonly targeted (Fig. 1.1).[5] Additionally, protein-protein interfaces, especially in the case of type-II toxin-antitoxin systems present in this work, are generally poorly conserved among homologous systems compared to active sites among enzymes, due the requirement of conserved catalytic residues required or enzyme activity. Thus, developing protein-protein interaction inhibitors requires extensive knowledge of the specific protein-protein interface in order to properly steer the initial screening process.[5] Protein-protein interaction "hotspots" serve as a strong starting point for such screening due to their significant contribution to the overall protein-protein interaction.[5]

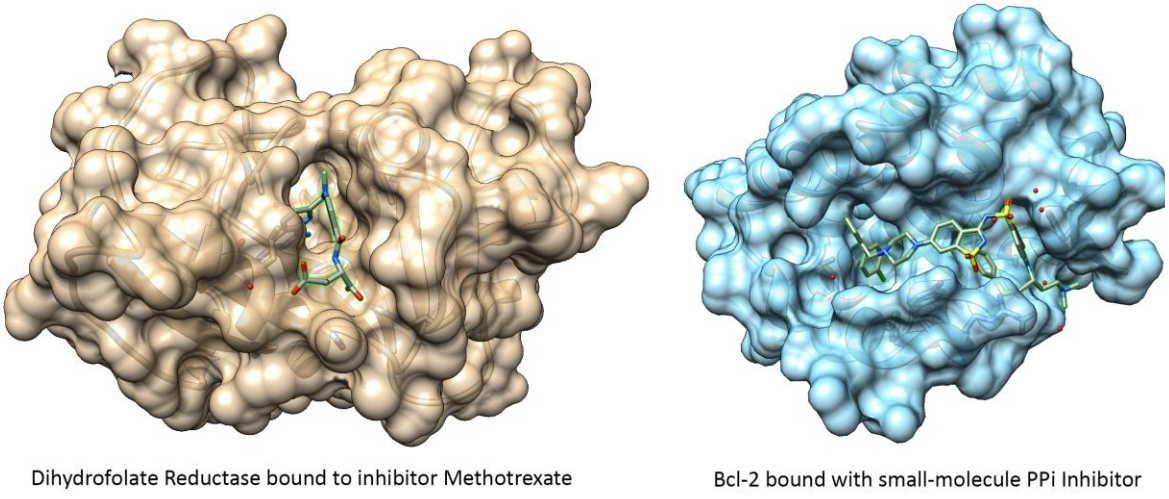

Figure 1.1. Comparison of binding sites for enzyme and protein-protein interaction inhibitors. *(Left)* Methotrexate bound to the active site of Dihyrdofolate reductase (DHFR) (PDB: 1RG7), Tan surface = DHFR, Gray = Methotrexate; *(Right)* Protein-protein interaction inhibitor of the Bcl-2/BH3 protein-protein interface (PDB: 4IEH), Blue surface = Bcl-2, Gray = small molecule inhibitor.

Toxin Antitoxin Systems

Toxin-antitoxin (TA) systems are bacterial operons are typically composed of two genes. One of the two genes of the TA system encodes a non-secreted metabolic regulator protein (toxin) which inhibits vital cellular processes resulting in growth suppression and cell death when expressed.[6-9] The cellular targets of toxin proteins vary widely, though DNA replication and translation are commonly targeted, with ribonucleases (both ribosome and non-ribosome dependent) being the most common function.[6-9] The toxin protein is either directly or indirectly neutralized by the second gene in the TA operon, with the second gene producing either an RNA or protein (antitoxin) that neutralizes the toxins activity.[6-9] In most cases, TA operons are oriented such that the antitoxin gene is transcribed first, with the toxin gene often having its ribosomal binding site overlapping with the end of the antitoxin gene. The first TA system identified was the CcdA-CcdB system from F-plasmid.[7,10,11] The F-plasmid CcdA-CcdB system was determined to control plasmid maintenance, through a post-segregational killing mechanism.[6-11] Toxin-antitoxin systems are currently subdivided into eight distinct classes based on the mechanism of toxin neutralization by the cognate antitoxin.[6-9]

Two of the most common TA systems are the Type-I and type-III TA systems which are defined by RNA-based antitoxins. Type-I antitoxins prevent toxin expression through a RNA interference mechanism, while type-III antitoxins form a protein-RNA pseudoknot complex which sequesters toxin protein.[6,8,9] Type-IV TA systems are composed of two genes encoding proteins which compete for binding to the same cellular target. Type-IV antitoxins bind to the same cellular target as type-IV toxins and protect the cellular target from the toxin protein either by preventing toxin binding, or through post-translational modification of the cellular target.[6,8,9] Type-V TA systems are defined by the presence of an antitoxin protein that serves as an endoribonuclease that preferentially targets the toxin mRNA.[6,9] Type-VI TA systems contain an

antitoxin that acts as a protease-adaptor protein that targets the toxin protein for degradation.[6,9] Type-VII TA systems utilize an antitoxin that directly inactivates the toxin protein via post-translational modification.[6] Type-VIII TA systems are uniquely composed of an RNA antitoxin which acts as a guide-RNA for a type-I CRISPR-Cas system, which transcriptionally represses the production of the RNA toxin.[6] Type-VIII TA systems are the only currently identified TA systems that do not produce protein toxins. These systems instead produced an RNA toxin that inhibit cell growth by binding to and sequestering tRNA.[6] TA systems belonging to types IV-VIII are poorly characterized, with most only have a few identified systems discovered to date.[6]

The final class of TA systems is the type-II TA systems which are similar to type-VI TA system in that they both require direct binding of an antitoxin protein to the toxin protein.[6-9] Unlike the type-VI TA system of which only a single system has been identified, type-II TA systems are highly abundant and widely studied. The type-II TA systems are composed of an antitoxin protein that directly binds to and neutralizes the toxin protein through the formation of a toxin-antitoxin complex.[6-9]

DNA Gyrase

DNA topoisomerases are essential enzymes required for maintaining the topology of DNA. Topoisomerases play a role in both DNA replication and transcription by controlling the DNA topology through introduction or relaxation of DNA supercoiling.[12,13] Topoisomerases are classified into two classes (type-I or type-II) based on their mechanism. Topoisomerase I creates a transient break in a single DNA strand, while Topoisomerase II make double-strand breaks in DNA.[12,13] Bacteria contain two homologous type-II topoisomerases, DNA Gyrase and Topoisomerase IV.[13,14]

DNA gyrase is composed of two protein subunits, termed Gyrase A (GyrA) and Gyrase B (GyrB).[12-14] The GyrA subunit is responsible for creating the double-strand breaks in DNA through an active-site tyrosine in the winged-helix domain (WHD) of GyrA. The GyrB subunit acts as ATPase which provides the energy required for completion of the DNA gyrase catalytic cycle.[12-14] DNA gyrase contains a unique function of creating negative supercoils in DNA compared to other type-II topoisomerases. The primary role of gyrase is to remove torsional strain created by replication forks during replication, and to remove torsional strain created by transcription.[14]

Homologous type-II topoisomerases are also found in eukaryotes, including humans, such as human Topoisomerase IIα and Topoisomerase IIβ.[14] While eukaryotic and bacterial topoisomerase share high sequence similarity, eukaryotic type-II topoisomerases are composed of a single subunit resulting from a fusion of the homologous genes from bacteria.[14] Small differences in sequence allow for preferential targeting of bacterial type-II topoisomerase.[14]

A combination of the essential nature of DNA gyrase, and its role in creating double-stranded breaks in DNA makes it a popular target for the development of novel antibiotics.[14] One mechanisms developed to take advantage of the double-stranded breaks created is the development of "poisons" of DNA gyrase.[14] DNA gyrase "poisons" such as quinolones act by binding to DNA gyrase active site after the double-strand break is made but before re-ligation occurs.[14] Quinolones intercalate into the DNA breaks and prevent gyrase from re-ligating the

DNA, resulting in accumulation of gyrase trapped in the cleavage-complex.[14] Quinolone binding to DNA gyrase is mediated by a water-metal ion bridge that provides the specificity of quinolones to bacteria (this water-metal ion bride is not present human type-II topoisomerases), with most common quinolone-resistant mutants in bacteria arising from disruption of this water-metal ion bridge.[14] The emergence of quinolone-resistant bacteria, has opened the door for the need to develop new DNA gyrase inhibitors that are not susceptible to the same resistance mechanism.

The ParDE Toxin-antitoxin System

The type-II TA system named ParDE is a potential target or model for the development of new antimicrobial therapeutics. ParDE systems are composed of a DNA gyrase targeting toxin protein (ParE) and a cognate antitoxin (ParD) which directly binds to and neutralizes ParE toxicity.[15,17] Like the related CcdA-CcdB type-II TA system, the ParDE system controls bacterial cell growth through inhibition of DNA gyrase. ParDE systems are particularly of interest as while the molecular mechanism of DNA gyrase inhibition is not yet known, it has been shown that ParE toxins are still active against DNA gyrase mutants which are resistant to CcdB or fluoroquinolones.[15] This indicates that ParE inhibits DNA gyrase may occur through a novel mechanism.[15] With DNA gyrase being a well validated antibacterial target (fluoroquinolones, aminocoumarins) for controlling bacterial cell growth, development of novel DNA gyrase inhibitors would be a beneficial avenue of research to pursue.[16]

Experimental evidence for the ParE mechanism is limited, but it has been shown to differ from fluoroquinolones such as ciprofloxacin and other DNA gyrase targeting toxins such as ccdB.[15] The most well characterized ParE systems is the ParDE2 system from *Vibrio cholerae*.[15,18] ParDE2 denotes that the system is composed of two proteins, the antitoxin ParD2, and the toxin ParE2. Due to bacteria often contain multiple homologous toxin-antitoxin systems, a number is added to denote the specific system, in this case, the number denotes that this is the second ParDE system identified in the *Vibrio cholerae* chromosome. The same naming scheme is used for all homologous toxin-antitoxin systems. Utilizing pull-down assays using his-tagged VcParE2, western blot analysis with anti-GyrA and anti-GyrB showed that both DNA gyrase subunits co-purified with VcParE2.[15] When VcParD2 was co-expressed with VcParE2, no co-purification of either DNA gyrase subunit was detected, indicating that VcParD2 is capable of preventing binding of VcParE2 to DNA gyrase.[15]

To further determine the binding region of VcParE2 to DNA gyrase, surface plasmon resonance was utilized. VcParE2 binding to various *E. coli* GyrA fragments as well as full-length *E. coli* GyrBA was investigated. VcParE2 was shown to bind to both full-length *E. coli* GyrBA, as well as GyrA59, a 59-kDa fragment, which lacks the c-terminal DNA binding domain of GyrA.[15] Unlike ccdB, which had been shown to bind to GyrA14, a 14-kDA fragment that forms the C-gate of GyrA, VcParE2 was unable to bind to GyrA14.[15,19] Additional SPR experiments were performed to determine if CcdB binding to GyrA precluded VcParE2 binding. Full-length GyrA was coupled to the SPR chip and then washed with *Vibrio fischeri* CcdB. After CcdB was successfully bound to GyrA, VcParE2 was washed over the CcdB-GyrA complex, and binding was detected, indicating that the binding site for CcdB and ParE do not overlap.[15]

The anti-gyrase activity of VcParE2 was also studied. DNA gyrase supercoiling assays were used to determine which DNA gyrase activities were inhibited by ParE. Relaxed or supercoiled DNA substrate in the presence of DNA gyrase was treated with either VcParE2 or the quinolone antibiotic nalidixic acid.[15] When starting with a relaxed DNA substrate, VcParE2 prevented DNA gyrase-mediated supercoiling similar to nalidixic acid, but VcParE2 was unable to inhibit DNA gyrase-mediated relaxation of supercoiled DNA, unlike nalidixic acid.[15] In the case of supercoiling of relaxed DNA substrate, VcParE2 was unable to inhibit DNA gyrase in the presence of VcParD2.[15] Additional experiments determined that VcParE2 inhibition of DNA gyrase was dependent on ATP hydrolysis.[15]

Like the VcParDE2 system, the ParDE2 system from *Mycobacterium tuberculosis* H37Rv has also been well characterized. Growth inhibition assay of MtParE2 was carried out in *E. coli* using a pBAD vector to overexpress MtParE2. When MtParE2 was overexpressed in the absence of MtParD2, a 5-log reduction in colony forming units was observed.[20] MtParE2-mediated growth inhibition was alleviated by the co-expression of the cognate MtParD2 antitoxin.[20] Due to differing toxicity of ParE toxins against Gyrase enzymes from different bacterial species, expression plasmids harboring native MtParE2 could not be transformed into *Mycobacterium smegmatis*, but a truncated version of MtParE2 with the last ten c-terminal amino acids of MtParE2 could be successfully transformed without significant impact on cell growth.[20] These results suggest that MtParE2 is a potent inhibitor, with enhanced toxicity against mycobacterial species.[20]

MtParE2 was further characterized by examining the effect of its overexpression on cell viability and cellular morphology in *E. coli*. Live-dead assays were carried out using Sybr Green / propidium iodide to determine the percentage of viable cells after MtParE2 overexpression. Our lab performed the same assay to compare several ParE proteins from different bacteria.[21] Assays were carried out a 0, 2, 4, 8, 12, and 20 hours post-induction of either MtParE2 (toxin-alone), or MtParDE2 (toxin-antitoxin complex). Overexpression of MtParDE2 showed no significant decrease in the amount of live cells (>90% viable), compared to the overexpression of MtParE2 alone.[20] When MtParE2 was overexpressed, the cell viability dropped to roughly 50% at 4 hours post-induction, with cell viability slowly recovering up to 85% at 20 hours post-induction.[20] To observe any changes in cell morphology, scanning electron microscopy (SEM) was utilized to view intact cells. Cells overexpressing MtParE2 showed an elongated phenotype when observed by SEM, characteristic of DNA gyrase inhibition.[20]

The anti-gyrase activity of MtParE2 was determined by *in vitro* gyrase supercoiling assays in the presence and absence of MtParE2. Recombinantly expressed MtGyrA and MtGyrB were mixed to reconstitute the MtGyrBA complex and incubated with MtParE2, MtParD2, or MtParDE2 in the presence of a relaxed pBR322 plasmid.[20] When MtGyrBA was treated with MtParE2, an accumulation of cleaved DNA bands were observed compared to a heat-inactivated MtParE2 control. The addition of MtParD2 could prevent ParE-mediated inhibition, when co-incubated, but could not reverse the inhibition if added later.[20]

To further study the mechanism, a combination of isothermal titration calorimetry (ITC) and surface plasmon resonance (SPR) were used to determine how MtParE2 binds to DNA gyrase. ITC data suggested an endothermic binding event between MtParE2 and MtGyrB, but the data

suggested only a weak interaction due to a lack of saturation. SPR confirmed a weak interaction between MtParE2 and MtGyrB ($K_d = 4.75x10^{-6}$ M).[20] No binding of MtParE2 to MtGyrA was observed using either method.[20] These results differ from those observed for VcParE2, suggesting that the mechanism of action is not identical for all ParE proteins.

In addition to mechanistic studies of ParE such as those from *Vibrio cholera* and *Mycobacterium tuberculosis*, the relationship between ParE toxins and other gyrase-targeting antibiotics has also been investigated. An attenuated ParE toxin from *Pseudomonas aeruginosa* PaParE1, was shown to provide protection to cells against anti-gyrase antibiotics.[22] Like the previously reported papers, the PaParE1 was shown to inhibit gyrase-mediated supercoiling of both its native *Pseudomonas aeruginosa* gyrase as well as *E. coli* gyrase, with differing IC_{50} values for each gyrase enzyme.[22] Like the MtParE2 toxin, PaParE1 was shown to significantly reduce colony forming units when overexpressed in *E. coli*, as well as inducing a filamentous cellular morphology, consistent with what was observed for MtParE2.[22]

To determine how overexpression of PaParE1 may impact the efficacy of other antibiotics, disk diffusion assays were utilized to determine effect of PaParE1 on various antibiotics. When *E. coli* cells overexpressing PaParE1 were challenged with non-gyrase targeting antibiotics such as gentamycin, tobramycin, chloramphenicol, or nitrofurantoin, no significant impact in antibiotic effectiveness was observed.[22] When the same experiments were performed using anti-gyrase inhibiting antibiotics such as novobiocin, ciprofloxacin, or levofloxacin, the zone of clearing was reduced by an average of 80%, suggesting that overexpression of PaParE1 provides protection against gyrase-targeting antibiotics regardless of their mechanism of action.[22]

Despite the anti-gyrase activity of ParE toxins being well characterized,[15,20] multiple gaps still exist in our understanding of how ParE toxins inhibit DNA gyrase. One of the major gaps in our understanding of inhibition mechanism arises from the ambiguous nature of how ParE toxins bind to DNA gyrase. Interaction studies of different ParE systems have indicated that the binding site of ParE toxins may not be consistent between homologous systems, with some papers indicating ParE binds to GyrA, such as in the case of VcParE2,[15] while other papers indicate ParE binds to GyrB, such as the case with MtParE2.[20] This ambiguity makes it difficult to create a unified model for ParE-mediated gyrase inhibition. Additionally, CFU measurements of cells overexpressing ParE toxins often show a rapid decrease in the amount of viable cells immediately after induction of ParE toxins, which is usually followed by recovering of cultures after extended time periods, suggesting that the cells may be able to overcome ParE-mediated toxicity through random mutagenesis caused by activation of error-prone DNA polymerases from the SOS pathway as a result of DNA-gyrase mediated double-stranded breaks in the chromosomal DNA.

To date, seven unique ParDE complex crystal structures have been deposited in the PDB. The seven structures represent ParDE systems from six different bacterial species: *Caulobacter crescentus* (ParDE1, PDB ID: 3KXE), *Mesorhizobium opportunistum* (ParDE2, PDB ID: 6X0A and ParDE3, PDB ID: 5CEG), *E. coli* (PaaA2-ParE2, PDB ID: 5CZE), *Pseudomonas aeruginosa* (ParDE1, PDB ID: 6XRW; this work, Chapter II), *Vibrio cholerae* (ParDE2, PDB ID: 7R5A), and *Shewanella oneidensis* (ParE-CopA, PDB ID: 7ETR).[23-29] Comparisons of these structures (Chapter II) illustrates that the toxin proteins form a well-defined fold despite low sequence

similarity, and that the ParD-ParE interface are structurally similar buy contain low sequence similarity in agreeance with the insulated nature (low cross-interaction) of homologous TA systems previously reported.[27]

Targeting PPIs of Toxin-Antitoxin Systems

Due to their widespread abundance in bacteria, TA systems have become a prospective target for the development of PPI inhibitors. Protein-protein interaction inhibitors which would selectively block the formation of the TA complex found in type-II toxin antitoxin systems, resulting in accumulation of "free" toxin protein. The PPI inhibitors are designed to compete with the native protein-protein interaction between the toxin and antitoxin to increase the amount of "free" toxin available within the cell. These protein-protein interaction inhibitors of TA systems can be used to develop new narrow-spectrum antibiotics by tailoring them to specific TA systems within a bacteria.

I. VapBC

The most widely studied type-II TA system for the development of PPI inhibitors is the virulence associated proteins VapBC system.[30-34] VapBC is composed of the PIN domain containing VapC toxin, and the associated VapB antitoxin. The VapC toxin acts as a ribonuclease, degrading mRNA resulting in inhibition of translation. Like all type-II TA systems, VapC toxicity is neutralized by direct binding with its cognate VapB antitoxin resulting in the formation of a non-toxic VapC-VapB protein-protein complex. Several studies have been published looking at the feasibility of using peptides derived from these proteins to develop competitive inhibitors of the native protein-protein interaction.

The VapBC TA system is one of the most widely abundant type-II TA systems currently identified. Bioinformatic analysis of bacterial genomes identified 47 VapBC systems in the pathogenic bacterium *Mycobacterium tuberculosis*, of which six of these systems (VapBC3, VapBC5, VapBC11, VapBC15, VapBC26, and VapBC30) have been targeted for the development of VapBC-derived peptide PPI inhibitors.[30-34]

For the VapBC30 system from *M. tuberculosis*, a 2.7 Å x-ray crystal structure of the VapBC30 complex was determined. The VapC30 toxin forms homodimer with an interface of 1100 $Å^2$, made up of residues from VapC α3, α4, α5, and α6.[31] Two different crystal forms were identified, which contain different interfaces between the cognate TA pair.[31] The VapB30 antitoxin interacts with the VapC30 toxin through two distinct sites, the N-terminal region spanning VapB30 residues 49-69, which forms an alpha-helix, and the C-terminal region spanning residues 71-81.[31] The protein-protein interface primarily involves interactions between VapB α1 (residues 49-62) with VapC30 α2 (residues 17-27) and VapC30 α4 (residues 52-65) (Fig. 1.2).[31]

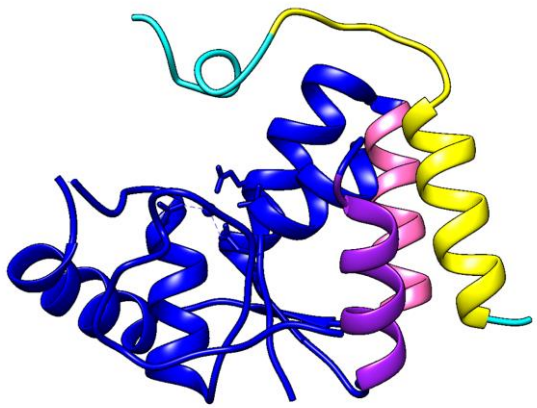

VapB30-VapC30 Dimer (PDB: 5XGR)

Figure 1.2. VapBC30-derived peptides for disrupting the protien-protein interaction of VapBC30 from *M. tuberculosis*. VapC30 (toxin) = blue; VapB30 (antitoxin) = cyan. VapC30-derived peptides (Peptide II, VapC30 α2 = pink and Peptide III, VapC30 α3 = purple); VapB30-derived peptide (Peptide I, VapB30 α4 = yellow). Peptides corresponding to the protein-protein interface of the VapBC30 dimer were developed and tested for their ability to disrupt the native protein-protein interaction.

In order to disrupt this interaction, peptides were derived from either VapB30 or VapC30 to competitively inhibit the formation of the native protein-protein interaction while maintaining VapC30 toxicity.[31] Three peptides were designed to mimic the three interacting regions and were tested for their ability to disrupt the native protein-protein interaction. The peptides' ability to activate the TA system was determined by performing mRNA cleavage assays using the VapBC30 complex incubated with increasing concentrations of VapBC30-derived peptides.[31] Of the three peptides tested, peptide I, derived from α1 of VapB30 showed the lowest disruption of complex as evidence by observing roughly 45% of activity compared to wild-type VapC30 when using 4-fold molar excess of the peptide.[31] Peptides II and III which correspond to VapC30 α2 (peptide II) and α4 (peptide III), which showed roughly 55% and 75% activity compared to wild-type respectively at a 4-fold molar excess.[31] These results indicate that targeting either side of the TA interface (at least in the case of VapBC) is a viable strategy for disrupting the native protein-protein interaction without impacting toxin activity.

Follow-up studies have been conducted on different VapBC systems from *M. tuberculosis* (VapBC3, VapBC5, VapBC11, VapBC15, VapBC26) in which VapB- and VapC-derived peptides as well as *de novo* peptides have been tested to activate the VapC toxin in each system.[32-37] A study of the VapBC26 system resulted in the generation of VapB- and VapC-derived peptides capable of directly disrupting the native protein-protein interaction of VapBC26 without disrupting VapC26 toxin function.[32] Study of the VapBC11 system resulted in the generation of VapB- and VapC- derived peptides which inhibited VapC toxin activity despite binding away from the toxin active site, showing the first case of peptide inhibitors of toxin proteins.[33] An additional study of the VapBC3, VapBC5, VapBC15, VapBC26, and VapBC30 systems was performed in which peptides-memetics were designed *in silico* and screened against each VapBC system to identify unique peptides capable of binding to and inhibit the formation of the protein-protein interaction of the VapBC systems.[34]

The results of the studies of targeting VapBC TA systems with toxin- or antitoxin-derived peptides, or *in silico* designed peptdies provides insight into how TA systems can be directly manipulated. The identification of peptides that can directly compete with antitoxins for toxin binding and disrupt the native protein-protein interaction is a major step towards developing new therapeutics utilizing toxin-antitoxins systems.

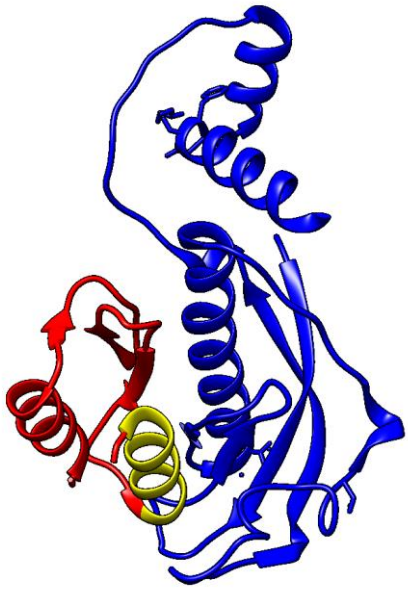

Figure 1.3. HicBA-derived peptide for disrupting the protien-protein interaction of HicBA from *S. pneunomia*. HicA (toxin) = red; HicB (antitoxin) = blue. HicA-derived peptides, α2 = yellow.

II. HicBA

Toxin-antitoxin interface-mimicking peptides have also been studied for the HicBA TA system from *Streptococcus pneumonia* strain TIGR4.[38] The HicBA TA system is composed a ribonuclease toxin HicA, and a cognate immunity protein HicB, which neutralizes HicA through direct binding to the HicB antitoxin.[38] Using a structure-guided approach aided by a 2.3 Å x-ray crystal structure (PDB ID: 5YRZ), the group identified a key active site residue His36 to be critical to the ribonuclease activity of HicA.[38] Structural analysis revealed that this active site residue makes close contacts with two residues of HicB, Thr33 and Glu47.[38] In order to liberate free toxin, HicA-derived peptides were generated to compete with wild-type HicA for binding to HicB, thus generating excess "free" toxin.[38] A peptide mimicking the HicA-HicB interface corresponding to α2 of HicA (Fig. 1.3) was shown to disrupt wild-type complex formation by 80% when present at a 4-fold excess relative to the wild-type HicBA heterodimer.[38] The peptide's disrupting ability was determined using similar protocols used for VapBC.[38] At equimolar concentrations of HicA-derived peptide relative to the heterodimer, a 50% increase in ribonuclease activity was observed.[38] The results suggest that toxin-derived peptides of the HicBA system are sufficient in competing with wild-type toxin to disrupt pre-formed complex, thus liberating "free" toxin protein that is active as evident by the increase in ribonuclease activity of HicBA in the presence of a HicA-derived peptide.

III. MazEF and the Extracellular Death Factor (EDF)

Enhancement of type-II toxin activity by peptides has been reported in the *MazEF* TA system from *E. coli*.[39] The quorum-sensing extracellular death factor peptide (EDF), a five amino acid long linear peptide (asn-asn-trp-asn-asn), was determined to be required for activation of the endoribonuclease toxin MazF.[39] The addition of EDF was shown to increase the endoribonuclease activity of MazF in a concentration-dependent manner.[39] The addition of full-

length EDF was also shown to reverse MazE-mediated inhibition of MazF. When EDF was added to the reaction simultaneously with MazE, MazF activity was similar to MazF alone.[39]

Mutational studies of EDF were performed and determined that the central amino acid (tryptophan) was required to alleviate MazE-mediated neutralization of MazF, while mutations at any other position did not significantly reduce EDF-mediated activation.[39] Binding assays were performed to determine whether EDF binds to MazF or MazE, and showed that EDF binds to MazF but not MazE.[39] Molecular modeling was used to predict how EDF could compete with MazE for MazF binding, and determined that EDF competes with $MazE_{71\text{-}75}$ (Ile-Asp-Trp-Gly-Glu), by mimicking critical MazE-MazF interactions.[39] These results indicate that EDF directly binds to MazF, and directly prevents antitoxin binding.

A follow-up study of EDFs from other bacteria (*Bacillus subtilis* and *Pseudomonas aeruginosa*) showed that EDFs could activate not only the homologous MazF toxins of their respective species, but also EcMazF.[40] MazF-mediated endoribonuclease activity was determined in the presence of the EDFs from *B. subtilis* and *P. aeruginosa*, and each EDF was shown to increase EcMazF activity. However, unlike EcEDF, the EDFs from *P. aeruginosa* were unable to alleviate EcMazE-mediated neutralization of EcMazF, indicating that they may activate MazF toxicity through different sites.[40] These results indicate that activiation of TA systems can be achieved through multiple mechanisms, either by directly inhibiting the formation of the toxin-antitoxin complex, or by directly increasing toxin activity in the presence of antitoxin.

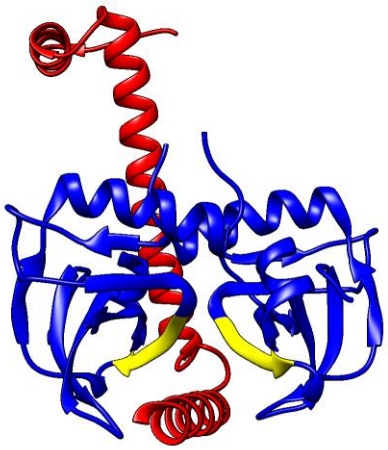

Figure 1.4. EDF binding site mapped to the MazEF4 toxin-antitoxin complex. MazF4 homodimer (toxin) = blue; MazE (antitoxin) = red. EDF binding site of MazF4 = yellow.

Additional studies of MazEF activation by EDFs were determined for the three (of seven) previously characterized MazEF TA systems from Mycobacterium tuberculosis.[41] Of the three MtMazEF TA systems tested, only MtMazEF3 and MtMazEF6 were shown to be activated by EcEDF as well as three PaEDFs. Both MtMazF3 and MtMazF6 endoribonuclease activity was significantly increased in the presence of EDFs from both *E. coli* and *P. aeruginosa*, but unlike EcMazF, both MtMazE3 and MtMazE6-mediated neutralization of their respective MazF toxins was alleviated by the three PaEDFs.[41] Unlike EcMazF, the previously identified EDF from *B. subtilis* did not increase the endoribonuclease activity for any of the three tested MtMazF toxins.[41] These results indicate that specific peptides are capable of binding to and activating homologous TA systems despite no known cross-talk between the tested TA systems.

An additional study of the MazEF4 TA system from *Mycobacterium tuberculosis* utilized x-ray crystallography and NMR to determine the binding site of a EDF to MazF4.[42] The study

identified a unique EDF homolog derived from *M. tuberculosis* and utilized $^{1}H,^{15}N$ HSQC NMR to determine the binding site of the EDF on MazF4.[42] The results indicated that the EDF binding site overlapped with the MazF4-MazE4 protein-protein interface corresponding to α3 of MazE4 (Fig. 1.4). The results of the MazEF-EDF studies indicate that peptides are capable of activating multiple homologous TA systems from different bacteria, indicating it may be possible to develop broad-spectrum therapeutics targeting TA systems.

IV. MoxXT

Another well-characterized toxin-antitoxin system in regard to the development of new antibiotics is the pemK/pemI (MoxXT) system from *Bacillus anthracis*. The toxin MoxT (a pemK-like toxin) was determined to be a potent ribonuclease. Based on homology modeling, structural similarity predictions showed BaMoxT had a 96% structural similarity to the endoribonuclease YdcE from *B. subtilis*, suggesting that BaMoxT would exhibit similar activity.[43]

A follow-up study of the *B. anthracis* MoxX-MoxT system was conducted to develop peptide inhibitors of the MoxX-MoxT protein-protein interaction.[44] Using extensive homology modeling, structures of the MoxT homodimer, the MoxX homodimer, and the MoxX-MoxT heterotetramer were predicted.[44] The MoxX-MoxT heterotetramer complex was predicted using rigid-body docking (GRAMMX protein docking server) of a truncated MoxX model to the predicted MoxT homodimer. After docking, the resulting heterotetramer was compared to the structure of the homologous EcMazEF to validate surface complementarity and similarity of binding.[44] The MoxX-MoxT structure indicated that the MoxX-MoxT interface is composed of two binding sites, denoted as site 1 and site 2.[44] Using the predicted complex structure, peptides were designed to target the MoxX-MoxT interface.[44] To determine the binding of the designed peptides to MoxT, flexible docking was performed using FlexPepDock (Rosetta). The top scoring model was selected as the most probable docking position. Binding of the predicted peptide (SKIGAWAS) was validated *in vitro* against MoxT. In addition to directly binding to MoxT, the peptide was also capable of disrupting the MoxX-MoxT complex formation.[44] The peptides reduced MoxT toxin activity, likely due to the predicted binding of the peptide close to the MoxT active site at site 2.[44] The results suggest that peptides targeting site 1 may yield better results of preventing MoxX binding without impacting MoxT activity.[44]

Additional peptides were designed to inhibit the MoxX-MoxT protein-protein interaction by targeting site 1 of the MoxX-MoxT interface.[45] To improve their rational design of peptides to inhibit the protein-protein interaction, an x-ray crystal structure of MoxT was determined to 1.8Å.[45] Structure comparison of the BaMoxT structure to the homologous EcMazEF structure resulted in the suggestion that the conserved site 1 binding pocket could be targeted by variety of peptide sequences.[45] It was predicted that EDF or EDF-like peptides would bind to site 1 of MoxT and allosterically activate it like in MazEF. Peptides were designed to mimic either EDF, MoxX, or MazE, and were then tested for their ability to disrupt the MoxX-MoxT protein-protein interaction. The two peptides which showed the greatest disruption of the MoxX-MoxT interaction were peptide II (an EDF-like peptide) and peptide VII (derived from MoxX residues 61-67.[45] The peptides were also tested to determine if they can enhance MoxT activity, and increased MoxT activity was shown in the presence of peptide I (an EDF-like peptide) and

peptide IV (derived from G6PDH from *B. anthracis*).[45] These results suggest that peptides can both inhibit antitoxin neutralization of their cognate toxin, as well as increasing toxin activity.

V. HipAB

Another translation inhibiting TA system HipAB from *E. coli* has been used in protein-protein interaction studies focused on disrupting the wild-type interaction and liberating "free" toxin.[46] The HipAB TA system is composed of a protein-kinase protein HipA, which inhibits translation through phosphorylation of glutamyl-tRNA synthetase.[47] Activation of HipA has been linked to the formation of multi-drug tolerant persister cells.[46-48] For the HipAB system, *in silico* docking was used to screen the Chemdiv kinase library and the SPECS compound library to identify potential novel inhibitors of HipA.[46] Compounds were screened for binding to the HipA D309Q x-ray crystal structure using Glide.[46,48] For the *in silico* screening, the D309Q mutation was reverted.[46] The *in silico* screening identified 190 potential compounds, which were selected for *in vitro* screening.[46] Identified compounds were screened for binding to HipA using surface plasmon resonance (SPR), and of the 190 tested compounds, 30 were shown to binding HipA *in vitro*.[46] The identified compounds were further narrowed by screening for antipersistence effects consistent with HipA deactivation.[46,48] Of the 30 compounds tested, 20 compounds decreased persister cell formation, while 6 of the 20 also showed cytotoxicity, and were excluded from additional testing.[46] Of the remaining 14 compounds, the top 4 performing antipersistence compounds were selected for additional testing. Binding affinities (K_d) were determined for each of the compounds to HipA, with values ranging from 0.27 uM to 54 uM.[46] These results are the first reported usage of compounds other than the cognate antitoxin to directly bind and neutralize toxin activity, indicating that these systems may be suitable for development of new therapeutics.

VI. ε-ζ

In addition to the previous studies involving type-II TA systems which alter cell growth via inhibition of translation, similar studies have been performed on TA systems targeting other critical cellular processes. One such system is the cell wall synthesis targeting ζ (zeta) toxin from the ε-ζ (epsilon-zeta) TA system from the broad-host range plasmid pSM19035 found in *Streptococcus pyogenes*.[49] The Zeta toxin causes cell lysis through inhibiting cell wall synthesis by phosphorylating uridine diphosphate-*N*-acetylglucosamine (UNAG), a peptidoglycan precursor.[50] The ε-ζ heterodimer interface is composed of α1, α2, α3, and α7 of the ζ toxin, and α1 of the ε antitoxin.[51] In this study, *S. pyogenes* ζ toxin-derived peptides were synthesized based on three of the four alpha-helices shown to contact the antitoxin as determined by the ε-ζ x-ray crystal structures (ζ toxin α3 was excluded due to its buried nature making it a poor target).[51] Zeta toxin-derived peptides were screened for binding against the epsilon antitoxin using a high-throughput fluorescence polarization assay.[47]

Binding affinities (K_d) were determine for peptides corresponding to ζ α1 (peptides Ia-c), ζ α2 (peptides IIa-c) and ζ α7 (peptides IIIa-c), and were compared to the K_d of the native ε-ζ complex.[49,51] The native complex was determined to have a K_d of 1 uM by fluorescence polarization.[49] Peptides Ia-c and IIa-c were shown to bind to ε with K_d values ranging from 74.5 nM (peptide Ia) to 169.5 nM (peptide IIa), which is significantly stronger than the wild-type interaction, indicating that these peptides could serve as a strong starting point for the development of competitive inhibitors of the native interaction.[49] While these peptides appear promising, the authors note that the peptide binding was limited to salt concentrations of less

than 100 mM sodium chloride, with higher salt concentrations significantly reduced the binding affinity.[49] Peptides corresponding to ζ α7 (peptides IIIa-c) were unable to bind to the ε antitoxin by fluorescence polarization.[49] Mutagenic studies were performed in which point mutants were introduced to the ζ toxin-derived peptides to determine "hot-spots" critical to the protein-protein interaction, which identified Asp18 of the ζ toxin α1 to be critical to the interaction.[49] When Asp18 was mutated to alanine, interaction with ε was completely abolished.[49]

Additional peptide-based therapeutics have been studied for Type VI secretion system (T6SS) effector-immunity (E-I) pairs, composed of a toxic effector protein which is secreted by the T6SS and a cognate immunity protein which protects the host cell from the toxicity of the effector protein, analogous to TA systems.[53]

The result of the previously mentioned studies indicates that TA systems can be directly manipulated by both toxin- or antitoxin-derived peptides as well as *de novo* peptide memetics in order to activate toxin-antitoxin sytems through either disrupting the toxin-antitoxin complex formation, or through direct activation of toxin proteins in the presence of cognate antitoxin protein.

The background outlined in Chapter I of this dissertation setup the rationale for the importance of research presented in following chapters. The major gaps in the field of toxin-antitoxin systems to be addressed in this work include: (1) How is "free" toxin protein generated in response to activation of toxin-antitoxin systems? (2) How does the protein-protein interactions of type-II TA systems impact antitoxin stability? (3) How can we manipulate TA systems to artificially activate them through generation of "free" toxin protein.

The subsequent chapters of this work sets out to characterize the type-II TA system ParDE1 from *Pseudomonas aeruginosa*. Chapter II is comprised of work published in the journal Biochemistry (American Chemical Society).[18] This work characterized the *Pseudomonas aeruginosa* ParD1-ParE1 protein complex, including extensive "hotspot" analysis using site-directed mutagenesis to probe the ParD1-ParE1 protein-protein interaction as well as determination of a 1.7 Å x-ray crystal structure of the ParDE1 complex. Chapter III is comprised of data disseminated as a bioRxiv, focusing on the instability of *Pseudomonas aeruginosa* ParD1.[54] Chapter IV is comprised of currently unpublished data probing the minimal antitoxin unit required for toxin binding, as well as probing the artificial activation of the ParE1 toxin from the ParDE1 complex using ParD1-derived peptides.

References

1. Stumpf, M. P., Thorne, T., de Silva, E., Stewart, R., An, H. J., Lappe, M., and Wiuf, C. (2008) Estimating the size of the human interactome. *Proc Natl Acad Sci U S A* **105**, 6959-6964
2. Lu, H., Zhou, Q., He, J., Jiang, Z., Peng, C., Tong, R., and Shi, J. (2020) Recent advances in the development of protein–protein interactions modulators: mechanisms and clinical trials. *Signal Transduction and Targeted Therapy* **5**, 213
3. Joerger, A. C., and Fersht, A. R. (2007) Structure–function–rescue: the diverse nature of common p53 cancer mutants. *Oncogene* **26**, 2226-2242

4. Kuzmanov, U., and Emili, A. (2013) Protein-protein interaction networks: probing disease mechanisms using model systems. *Genome Medicine* **5**, 37
5. Milroy, L.-G., Grossmann, T. N., Hennig, S., Brunsveld, L., and Ottmann, C. (2014) Modulators of Protein–Protein Interactions. *Chemical Reviews* **114**, 4695-4748
6. Jurėnas, D., Fraikin, N., Goormaghtigh, F., and Van Melderen, L. (2022) Biology and evolution of bacterial toxin–antitoxin systems. *Nature Reviews Microbiology* **20**, 335-350
7. Fraikin, N., Goormaghtigh, F., and Van Melderen, L. (2020) Type II Toxin-Antitoxin Systems: Evolution and Revolutions. *Journal of Bacteriology* **202**, e00763-00719
8. Harms, A., Brodersen, D. E., Mitarai, N., and Gerdes, K. (2018) Toxins, Targets, and Triggers: An Overview of Toxin-Antitoxin Biology. *Molecular Cell* **70**, 768-784
9. Page, R., and Peti, W. (2016) Toxin-antitoxin systems in bacterial growth arrest and persistence. *Nature Chemical Biology* **12**, 208-214
10. Gerdes, K., Rasmussen, P. B., and Molin, S. (1986) Unique type of plasmid maintenance function: postsegregational killing of plasmid-free cells. *Proceedings of the National Academy of Sciences* **83**, 3116-3120
11. Ogura, T., and Hiraga, S. (1983) Mini-F plasmid genes that couple host cell division to plasmid proliferation. *Proceedings of the National Academy of Sciences* **80**, 4784-4788
12. Wang, J. C. (2002) Cellular roles of DNA topoisomerases: a molecular perspective. *Nature Reviews Molecular Cell Biology* **3**, 430-440
13. Dighe, S. N., and Collet, T. A. (2020) Recent advances in DNA gyrase-targeted antimicrobial agents. *European Journal of Medicinal Chemistry* **199**, 112326
14. Aldred, K. J., Kerns, R. J., and Osheroff, N. (2014) Mechanism of Quinolone Action and Resistance. *Biochemistry* **53**, 1565-1574
15. Yuan, J., Sterckx, Y., Mitchenall, L. A., Maxwell, A., Loris, R., and Waldor, M. K. (2010) Vibrio cholerae ParE2 poisons DNA gyrase via a mechanism distinct from other gyrase inhibitors. *J Biol Chem* **285**, 40397-40408
16. Collin, F., Karkare, S., and Maxwell, A. (2011) Exploiting bacterial DNA gyrase as a drug target: current state and perspectives. *Appl Microbiol Biotechnol* **92**, 479-497
17. Fiebig, A., Castro Rojas, C. M., Siegal-Gaskins, D., and Crosson, S. (2010) Interaction specificity, toxicity and regulation of a paralogous set of ParE/RelE-family toxin-antitoxin systems. *Mol Microbiol* **77**, 236-251
18. Yuan, J., Yamaichi, Y., and Waldor Matthew, K. (2011) The Three Vibrio cholerae Chromosome II-Encoded ParE Toxins Degrade Chromosome I following Loss of Chromosome II. *Journal of Bacteriology* **193**, 611-619
19. Dao-Thi, M.-H., Van Melderen, L., De Genst, E., Afif, H., Buts, L., Wyns, L., and Loris, R. (2005) Molecular Basis of Gyrase Poisoning by the Addiction Toxin CcdB. *Journal of Molecular Biology* **348**, 1091-1102
20. Gupta, M., Nayyar, N., Chawla, M., Sitaraman, R., Bhatnagar, R., and Banerjee, N. (2016) The Chromosomal parDE2 Toxin-Antitoxin System of Mycobacterium tuberculosis H37Rv: Genetic and Functional Characterization. *Front Microbiol* **7**, 886
21. Ames, J. R., Muthuramalingam, M., Murphy, T., Najar, F. Z., and Bourne, C. R. (2019) Expression of different ParE toxins results in conserved phenotypes with distinguishable classes of toxicity. *Microbiologyopen* **8**, e902
22. Muthuramalingam, M., White, J. C., Murphy, T., Ames, J. R., and Bourne, C. R. (2019) The toxin from a ParDE toxin-antitoxin system found in Pseudomonas aeruginosa offers

protection to cells challenged with anti-gyrase antibiotics. *Molecular Microbiology* **111**, 441-454
23. Snead, K. J., Moore, L. L., and Bourne, C. R. (2022) ParD Antitoxin Hotspot Alters a Disorder-to-Order Transition upon Binding to Its Cognate ParE Toxin, Lessening Its Interaction Affinity and Increasing Its Protease Degradation Kinetics. *Biochemistry* **61**, 34-45
24. Zhou, J., Du, X.-J., Liu, Y., Gao, Z.-Q., Geng, Z., Dong, Y.-H., and Zhang, H. (2021) Insights into the Neutralization and DNA Binding of Toxin-Antitoxin System ParESO-CopASO by Structure-Function Studies. *Microorganisms* **9**
25. Lite, T.-L. V., Grant, R. A., Nocedal, I., Littlehale, M. L., Guo, M. S., and Laub, M. T. (2020) Uncovering the basis of protein-protein interaction specificity with a combinatorially complete library. *eLife* **9**, e60924
26. Sterckx, Y. G. J., Jové, T., Shkumatov, A. V., Garcia-Pino, A., Geerts, L., De Kerpel, M., Lah, J., De Greve, H., Van Melderen, L., and Loris, R. (2016) A unique hetero-hexadecameric architecture displayed by the Escherichia coli O157 PaaA2–ParE2 antitoxin–toxin complex. *Journal of Molecular Biology* **428**, 1589-1603
27. Aakre, Christopher D., Herrou, J., Phung, Tuyen N., Perchuk, Barrett S., Crosson, S., and Laub, Michael T. (2015) Evolving New Protein-Protein Interaction Specificity through Promiscuous Intermediates. *Cell* **163**, 594-606
28. Dalton, K. M., and Crosson, S. (2010) A Conserved Mode of Protein Recognition and Binding in a ParD−ParE Toxin−Antitoxin Complex. *Biochemistry* **49**, 2205-2215
29. Garcia-Rodriguez, G., Girardin, Y., Singh, R. K., Volkov, A. N., Konijnenberg, A., Sobott, F., Charlier, D., and Loris, R. (2021) Vibrio cholerae ParE2 toxin modulates its operon transcription by stabilization of an antitoxin DNA ruler. *bioRxiv*, 2021.2003.2022.436508
30. Ramage, H. R., Connolly, L. E., and Cox, J. S. (2009) Comprehensive functional analysis of Mycobacterium tuberculosis toxin-antitoxin systems: implications for pathogenesis, stress responses, and evolution. *PLoS Genet* **5**, e1000767-e1000767
31. Lee, I.-G., Lee, S. J., Chae, S., Lee, K.-Y., Kim, J.-H., and Lee, B.-J. (2015) Structural and functional studies of the Mycobacterium tuberculosis VapBC30 toxin-antitoxin system: implications for the design of novel antimicrobial peptides. *Nucleic Acids Res* **43**, 7624-7637
32. Kang, S.-M., Kim, D.-H., Lee, K.-Y., Park, S. J., Yoon, H.-J., Lee, S. J., Im, H., and Lee, B.-J. (2017) Functional details of the Mycobacterium tuberculosis VapBC26 toxin-antitoxin system based on a structural study: insights into unique binding and antibiotic peptides. *Nucleic Acids Res* **45**, 8564-8580
33. Deep, A., Tiwari, P., Agarwal, S., Kaundal, S., Kidwai, S., Singh, R., and Thakur, K. G. (2018) Structural, functional and biological insights into the role of Mycobacterium tuberculosis VapBC11 toxin-antitoxin system: targeting a tRNase to tackle mycobacterial adaptation. *Nucleic Acids Res* **46**, 11639-11655
34. Sundar, S., Rajan, M. P., and Piramanayagam, S. (2019) *In silico* Derived Peptides for Inhibiting the Toxin–Antitoxin Systems of Mycobacterium tuberculosis: Basis for Developing Peptide-Based Therapeutics. *International Journal of Peptide Research and Therapeutics* **25**, 1467-1475

35. Sedan, Y., Marcu, O., Lyskov, S., and Schueler-Furman, O. (2016) Peptiderive server: derive peptide inhibitors from protein-protein interactions. *Nucleic Acids Res* **44**, W536-W541
36. Kozakov, D., Hall, D. R., Xia, B., Porter, K. A., Padhorny, D., Yueh, C., Beglov, D., and Vajda, S. (2017) The ClusPro web server for protein–protein docking. *Nature Protocols* **12**, 255-278
37. Ahn, D.-H., Lee, K.-Y., Lee, S. J., Park, S. J., Yoon, H.-J., Kim, S.-J., and Lee, B.-J. (2017) Structural analyses of the MazEF4 toxin-antitoxin pair in Mycobacterium tuberculosis provide evidence for a unique extracellular death factor. *Journal of Biological Chemistry* **292**, 18832-18847
38. Kim, D.-H., Kang, S.-M., Park, S. J., Jin, C., Yoon, H.-J., and Lee, B.-J. (2018) Functional insights into the Streptococcus pneumoniae HicBA toxin-antitoxin system based on a structural study. *Nucleic Acids Res* **46**, 6371-6386
39. Belitsky, M., Avshalom, H., Erental, A., Yelin, I., Kumar, S., London, N., Sperber, M., Schueler-Furman, O., and Engelberg-Kulka, H. (2011) The Escherichia coli Extracellular Death Factor EDF Induces the Endoribonucleolytic Activities of the Toxins MazF and ChpBK. *Molecular Cell* **41**, 625-635
40. Kumar, S., and Engelberg-Kulka, H. (2014) Quorum sensing peptides mediating interspecies bacterial cell death as a novel class of antimicrobial agents. *Current Opinion in Microbiology* **21**, 22-27
41. Nigam, A., Kumar, S., and Engelberg-Kulka, H. (2018) Quorum Sensing Extracellular Death Peptides Enhance the Endoribonucleolytic Activities of Mycobacterium tuberculosis MazF Toxins. *mBio* **9**, e00685-00618
42. Ahn, D.-H., Lee, K.-Y., Lee, S. J., Park, S. J., Yoon, H.-J., Kim, S.-J., and Lee, B.-J. (2017) Structural analyses of the MazEF4 toxin-antitoxin pair in Mycobacterium tuberculosis provide evidence for a unique extracellular death factor. *Journal of Biological Chemistry* 292, 18832-18847
43. Agarwal, S., Mishra, N. K., Bhatnagar, S., and Bhatnagar, R. (2010) PemK toxin of Bacillus anthracis is a ribonuclease: an insight into its active site, structure, and function. *J Biol Chem* **285**, 7254-7270
44. Chopra, N., Agarwal, S., Verma, S., Bhatnagar, S., and Bhatnagar, R. (2011) Modeling of the structure and interactions of the B. anthracis antitoxin, MoxX: deletion mutant studies highlight its modular structure and repressor function. *Journal of Computer-Aided Molecular Design* **25**, 275-291
45. Verma, S., Kumar, S., Gupta, V. P., Gourinath, S., Bhatnagar, S., and Bhatnagar, R. (2015) Structural basis of Bacillus anthracis MoxXT disruption and the modulation of MoxT ribonuclease activity by rationally designed peptides. *Journal of biomolecular structure & dynamics* **33**, 606-624
46. Li, T., Yin, N., Liu, H., Pei, J., and Lai, L. (2016) Novel Inhibitors of Toxin HipA Reduce Multidrug Tolerant Persisters. *ACS Med Chem Lett* **7**, 449-453
47. Germain, E., Castro-Roa, D., Zenkin, N., and Gerdes, K. (2013) Molecular mechanism of bacterial persistence by HipA. *Mol Cell* **52**, 248-254
48. Schumacher, M. A., Piro, K. M., Xu, W., Hansen, S., Lewis, K., and Brennan, R. G. (2009) Molecular mechanisms of HipA-mediated multidrug tolerance and its neutralization by HipB. *Science (New York, N.Y.)* **323**, 396-401

49. Fernández-Bachiller, M. I., Brzozowska, I., Odolczyk, N., Zielenkiewicz, U., Zielenkiewicz, P., and Rademann, J. (2016) Mapping Protein-Protein Interactions of the Resistance-Related Bacterial Zeta Toxin-Epsilon Antitoxin Complex ($\varepsilon_2\zeta_2$) with High Affinity Peptide Ligands Using Fluorescence Polarization. *Toxins* **8**, 222
50. Mutschler, H., Gebhardt, M., Shoeman, R. L., and Meinhart, A. (2011) A novel mechanism of programmed cell death in bacteria by toxin-antitoxin systems corrupts peptidoglycan synthesis. *PLoS Biol* **9**, e1001033-e1001033
51. Meinhart, A., Alonso, J. C., Sträter, N., and Saenger, W. (2003) Crystal structure of the plasmid maintenance system epsilon/zeta: functional mechanism of toxin zeta and inactivation by epsilon 2 zeta 2 complex formation. *Proc Natl Acad Sci U S A* **100**, 1661-1666
52. Kenny, C. H., Ding, W., Kelleher, K., Benard, S., Dushin, E. G., Sutherland, A. G., Mosyak, L., Kriz, R., and Ellestad, G. (2003) Development of a fluorescence polarization assay to screen for inhibitors of the FtsZ/ZipA interaction. *Analytical Biochemistry* **323**, 224-233
53. Gao, X., Mu, Z., Qin, B., Sun, Y., and Cui, S. (2017) Structure-Based Prototype Peptides Targeting the Pseudomonas aeruginosa Type VI Secretion System Effector as a Novel Antibacterial Strategy. *Front Cell Infect Microbiol* **7**, 411-411
54. Snead, K. J., and Bourne, C. R. (2021) Intrinsic Degradation of the Type-II Antitoxin ParD from Pseudomonas aeruginosa. *bioRxiv*, 2021.2003.2029.437564

Chapter II: ParD Antitoxin Hotspot Alters a Disorder-to-Order Transition upon Binding to Its Cognate ParE Toxin, Lessening Its Interaction Affinity and Increasing Its Protease Degradation Kinetics

Kevin J. Snead, Landon L. Moore, and Christina R. Bourne

Biochemistry 2022, 61, 34−45

Reprinted with permission from *Biochemistry* 2022, 61, 1, 34–45
Publication Date: December 16, 2021 https://doi.org/10.1021/acs.biochem.1c00584.

I collected and processed all of the data for the manuscript with the exception of the bacterial two-hybrid assay (figure 2.5) which was performed by Dr. Landon Moore. All figures were produced by me with some edits performed by Dr. Christina Bourne. Writing of the manuscript was performed by me with the exception of the discussion section which was written with assistance from Dr. Christina Bourne. Editing and feedback on all writing was provided by Dr. Christina Bourne.

Abstract

Type-II toxin−antitoxin (TA) systems are comprised of two tightly interacting proteins, and operons encoding these systems have been identified throughout the genomes of bacteria. In contrast to secretion system effector−immunity pairs, TA systems must remain paired to protect the host cell from toxicity. Continual depletion of the antitoxin results in a shorter half-life than that of the toxin, though it is unclear if antitoxins can be effectively degraded when complexed with toxins. The current work probed the protein−protein interface of the PaParDE1 TA system, guided by an Xray crystal structure, to determine contributions of antitoxin amino acids to interaction kinetics and affinity. These studies identified a "hotspot" position that alters the binding mode and resulting affinity (K_d) from 152 pM for a 1:1 model for wild type to 25.5 and 626 nM for a 2:1 model with mutated antitoxin. This correlates with an altered induced secondary structure upon complexation with PaParE1 and increased kinetics of Lon protease digestion of the antitoxin despite the toxin presence. However, the decreased affinity at this hotspot was essentially reversed when the antitoxin dimerization region was deleted, yielding insights into complex interactions involved in the tight association. Removal of the antitoxin C-terminal seven amino acids, corresponding to the site of a disorder-to-order transition, completely prevents association. These studies combine to provide a model for the initiation of the TA interaction and highlight how manipulation of the sequence can impact the antitoxin disorder-to-order transition, weakening the affinity and resulting in increased antitoxin susceptibility to degradation.

Introduction

Protein−protein interactions mediate essential functions for life, and understanding the molecular basis of their specificity can provide valuable insights into their functions.[1] Interactions between effectors and cognate immunity proteins, such as those found in toxin−antitoxin (TA) systems, type-VI secretion systems, and contact-dependent inhibition systems, determine the protection of host cells and, in some cases, the targeting of other cells. The type-II TA systems are composed of a non-secreted toxin protein that is neutralized by a highly specific cognate antitoxin protein that serves an "immunity" function.[2,3] In other effector−immunity pairs, the neutralizing immunity proteins are known to be extremely stable and provide constant protection to the host as toxins are secreted.[4] Remarkable similarity has been noted among these different effector−immunity pairs, in particular among toxin mechanisms of cell death involving nuclease activity.[4,5] In contrast to immunity proteins of effector−immunity pairs, antitoxins of TA systems are continuously depleted by ATP-dependent AAA+ proteases. This results in a shorter half-life of the antitoxin relative to the non-secreted toxin protein, such that continual translational replenishment of antitoxin is needed to maintain toxin neutralization.[6−13]

TA systems were originally identified as mediators of plasmid inheritance through a post-segregational killing (PSK) mechanism that is predicated on the shorter half-life of antitoxin molecules and the subsequent liberation of toxin activity.[3] However, TA systems are also integrated into the genomes of bacteria and archaea; the role of these systems within their host cells is an issue of active debate.[2,3,7,8,10,14,15] For secreted effectors, the interaction with cognate immunity proteins in host cells is prevented by chaperones that deliver the effector to the secretion apparatus.[16] Presumably in these cases, the interaction with a cognate immunity protein should be essentially irreversible to maintain host protection. For TA systems, the two protein components associate directly, and it is unclear if the tightly interacting antitoxin proteins can be degraded directly from a complex with toxin, as is implied for the PSK model of TA system function.

Among a given TA system family, individually encoded antitoxins have low sequence similarity at the sites of these interactions, leading to high specificity for their cognate toxins with only limited "cross-talk" between homologous TA systems.[18−21] Type-II TA systems form extensive protein− protein interfaces, typically with nanomolar affinity and spanning surface areas of more than 1400 Å2.[19,21−25] A recent study detected the degradation of TA system antitoxins without an accompanying gain of toxin activity for ribonucleic acid (RNA) cleaving toxins within Escherichia coli, consistent with a lack of antitoxin degradation from pre-formed complexes.[26] This appears to contrast the canonical PSK model, which requires the generation of free toxin after loss of the plasmid encoding TA system genes,[17] leading to questions of how tightly interacting TA proteins could be parted as antitoxin is degraded. This led us to further question if there might be "hot spots" within these TA interactions, such that interruption at one specific site could facilitate antitoxin removal from a TA complex. We hypothesized that the identification of such "hot spots" would provide insights into the vulnerable regions of interactions amenable to interruption by cellular components or by intentional external manipulation.[20,27−31]

The type-II TA system ParDE was first identified on the broad-range plasmid RK2 as a plasmid stabilization element that causes growth inhibition upon plasmid loss.[32] ParE toxins are structural

homologs of the TA system RelE-superfamily of RNase enzymes, as well as colicin and barnase nucleases.[33] However, ParE toxins have been well-documented as causing growth inhibition through the inhibition of deoxyribonucleic acid (DNA) gyrase.[22,34,35] The ParE1 toxin from Pseudomonas aeruginosa (PaParE1) used in this study has been shown to inhibit DNA gyrase-mediated supercoiling, and its attenuated toxicity could provide target protection to cells treated with anti-gyrase antibiotics.[22] Other ParE toxins, such as three ParE proteins from Vibrio cholerae, have been shown to select for chromosome II of V. cholera in a PSK-type function.[36] It has been demonstrated that ATP-driven proteases Lon and ClpP degrade intracellular antitoxins *in vivo*, including for the plasmid-derived RK2−ParDE system.[9,11,13,37] Given the overlap of ParE activity with the well-validated gyrase antibacterial target, there is interest in the manipulation of toxin activation via liberation from antitoxin.

The current study examined the ParD−ParE interactions of the chromosomally encoded PaParDE1 system with an aim of characterizing the important molecular determinants of complex formation and stability. Guided by a crystallographic structure of the PaParDE1 complex (PDB ID: 6XRW), site-directed mutagenesis experiments identified an amino acid change that was sufficient to decrease the interaction affinity (K_d) from picomolar to high nanomolar, concomitant with a change in the mode of binding. Further, C-terminal truncations identified that the last seven amino acids of the PaParD1 antitoxin are required for initiation of the interaction with the PaParE1 toxin. The interaction with the PaParE1 toxin proved critical for the protection of PaParD1 from *in vitro* Lon protease degradation. Overall, these results yield insights into how the complex formation is initiated, individual PaParD1 interfacial amino acid contributions to a disorder-to-order transition and thus to the strength of interaction, and how this in turn impacts protease degradation of antitoxin.

Experimental Details

Expression and Purification of P. aeruginosa PaParDE1

The cloning and expression of the genes encoding PaParD1 and PaParE1 have been previously described.[22] Mutants were generated using the QuikChange (Stratagene) or Q5 (NEB) mutagenesis kits (sequences and primers are given in Table S2.1). In brief, these genes were separately cloned into the pET-15b plasmid in frame with an N-terminal 6× his-tag and thrombin cleavage site. Protein expression was induced by the addition of 1 mM IPTG to the media; PaParD1 was expressed at 25 °C for 4−6 h to minimize in situ degradation, while PaParE1 was expressed at 16 °C overnight (possible due to its limited toxicity) prior to harvesting by centrifugation.

Protein purification was carried out by closely following previously reported procedures.[22] In short, cell pellets were resuspended in a 50 mM Tris-HCl pH 8.5, 300 mM NaCl, 40 mM imidazole buffer and lysed using a high-pressure homogenizer (Emulsiflex). The clarified lysate was passed through a HisTrap FF Ni-NTA column (GE Healthcare) and eluted using a linear gradient with a 50 mM Tris-HCl pH 8.5, 300 mM NaCl, 500 mM imidazole buffer. The eluted protein was desalted in a 50 mM Tris-HCl pH 8.5, 300 mM NaCl buffer using a HiPrep 26/10 desalting column (GE Healthcare) and concentrated using a 3 kDa molecular weight cut-off (MWCO) Ultra-15 concentrator (Amicon) prior to separation by size-exclusion chromatography

using a Superdex 75 10/300 GL (GE Healthcare) column pre-equilibrated with a 50 mM Tris-HCl pH 8.5, 300 mM NaCl buffer.

When necessary, cleavage of affinity (6×-his) tags was performed prior to size-exclusion chromatography using thrombin. Proteins were buffer-exchanged into 50 mM HEPES pH 7.5, 150 mM NaCl. Cleavage was performed using 1 U thrombin (bovine, Sigma) per 1 mg protein overnight at 4 °C. The uncleaved protein was separated from the cleaved protein using a HisTrap FF Ni-NTA column according to the method described above. Gel-filtration was then carried out using a Superdex 75 10/300 GL column (GE Healthcare) pre-equilibrated in 50 mM Tris-HCl pH 8.5, 300 mM NaCl.

The PaParDE1 complex was formed by first buffer exchanging purified PaParD1 and purified PaParE1 into 50 mM MES pH 6.0, 300 mM NaCl, 5% glycerol, prior to mixing 1:1 for 30 min to 1 h at 4 °C. After mixing, the complex was concentrated (if necessary) prior to purification using a HiLoad 16/600 Superdex 75 pg column (GE Healthcare) or Superdex 75 10/300 GL column (GE Healthcare) preequilibrated in a 25 mM MES pH 6.0, 150 mM NaCl, 5% glycerol buffer. Protein purity and integrity were assessed under denaturing and reducing conditions with 12% acrylamide gels in a Tris-HCl−tricine buffer system.[38]

Structure Determination and Analysis of PaParDE1

Initial broad screening of the PaParDE1 complex (10.5 mg/ mL in 25 mM MES pH 6.0, 150 mM NaCl, 5%, glycerol) was carried out at 293 K in a 96-well plate using sitting drop vapor diffusion crystallography with the aid of a mosquito crystallization robot (TPP LabTech). Optimization screens were performed in 24-well plates using sitting drop vapor diffusion. Diffraction quality crystals were obtained after 72 h in a condition of 7.5% (v/v) 2-methyl-2,4-pentanediol (MPD), 20% PEG 6000, 25 mM ammonium sulfate, and 100 mM TrisHCl pH 7.0. Prior to data collection, PaParDE1 crystals were plunged in liquid nitrogen directly from the crystallization mother liquor. X-ray diffraction was collected on a MicroMax 007HF microfocus X-ray generator (Rigaku) with a Pilatus 200K silicon pixel detector (Dectris). Data processing and scaling were performed using HKL3000R (HKL Research Inc.). Phasing was solved using the program phaser,[39] as implemented in the package Phenix, for molecular replacement. Many starting models were screened, with satisfactory solutions only arising using a hybrid template of a ParE−ParD dimer, lacking the ParD DNA binding domain, generated through manual inspection and curation of regions and loops; two of these dimer models were placed. Refinement of phases was initiated with AutoBuild (Phenix package) that placed missing protein regions, followed with iterative cycles with Phenix refine and manual adjustments in coot.[39,40] Statistics for data collection and refinement are presented in Table S2.2. Subsequent structure-based sequence alignments and visualization of PDB structures were performed using UCSF Chimera;[41] sequence alignment figures were prepared using the ESPript 3 webserver.[42] Surface area values and energetics were obtained using the PDBePISA webserver from EMBL.[43]

Biolayer Interferometry

Prior to biolayer interferometry (BLI), samples were desalted into a 50 mM Tris-HCl pH 8.5, 300 mM NaCl, 0.5% BSA, 0.05% Tween-20 buffer, and all solutions were matched to these buffer conditions. BLI was performed at 25 °C using an Octet RED96 interferometer (Pall ForteBio) by coupling 100 nM WT or mutant His-tagged ParD1 proteins to Ni-NTA BLI sensor

pins. WT-untagged PaParE1 was serially diluted (10 to 0.3125 nM; I68A PaParD1 required 10× higher concentrations) and incubated with ParD1-coupled pins until the association approached saturation, and then the dissociation rates were measured. Rates were calculated by fitting the curves to a 1:1 Langmuir binding model, except for I68A which required a 2:1 binding model to be fitted, as performed with manufacturer-provided BioAnalysis software (v 8.2). Individual curves were analyzed to ensure high quality fits with R2 values greater than 0.95 (see Figure S2.1); individual assays were repeated at least three times to obtain average K_d values, where possible, as calculated from the ratio of the dissociation rate to the association rate; in the absence of dissociation rates, the association rates were compared (the summary of replicates is given in Table S2.3).

Size Exclusion Chromatography-Multiangle Light Scattering

Size exclusion chromatography−multiangle light scattering (SEC−MALS) experiments were carried out at room temperature using the flow cell of a Wyatt miniDAWN Treos system integrated with a refractive index (RI) detector. Samples were introduced from a liquid chromatography system and separated over Superdex 200 Increase 10/30 GL (GE Healthcare) equilibrated in 50 mM MES buffer, pH 6.0, 300 mM NaCl, 5% (v/v) glycerol. The analysis followed the manufacturer's recommendations using the ASTRA software package (Wyatt Technologies, v. 6.1) to calculate the weight-averaged molecular weight; protein concentrations were determined from the RI signal (see Figure S2.2). Data were exported from ASTRA and re-plotted in GraphPad Prism (v. 6.0d) for graphic presentation.

Fourier-Transform Infrared Spectroscopy

The protein secondary structure was measured via amide I and amide II stretching from wavenumbers between 1700 and 1500 cm−1 measured at room temperature using a Tensor II Fourier transform infrared (FTIR) CONFOCHECK (Bruker) equipped with a BioATR unit. All samples were desalted into 50 mM MES pH 6.5, 300 mM NaCl, 5% glycerol and concentrated to 1 mg/mL prior to analysis. A blank run of buffer was performed and subtracted from each sample to eliminate the background buffer signal, and three technical replicates were performed for each measurement (see Table S2.4). The protein secondary structure values reported were calculated using the predefined α helix and β sheet methods for secondary structure determination provided with the CONFOCHECK software.

Bacterial Two-Hybrid Assay

Plasmids and controls were purchased from Euromedex; cloning utilized a Q5-mediated gene amplification and HiFi DNA assembly mix (NEB). Competent *E. coli* BTH101 cultures were co-transformed with 30 ng each of pUT18C or pKT25 plasmids using a standard heat shock protocol. LB supplemented with kanamycin (50 μg/mL) and carbenicillin (100 μg/mL) was used to select for the two plasmids. Additionally, X-Gal (40 μg/mL) and IPTG (0.5 mM) were included in the plated media to assess the interactions via reconstitution of the adenylate cyclase activity, evident by the blue colony. Plates were incubated 24 h at 30 °C and then scored for the colony color, with blue indicating a positive interaction between bait and prey fusion proteins. Incubation was continued for 2−3 days longer at room temperature to look for weak or transient interactions. Miller units were determined using the Miller assay, as previously described44 (see Figure S2.3). In brief, liquid cultures with both kanamycin and carbenicillin selection were grown overnight at 30 °C. Standardized volumes of these cultures were lysed using BugBuster

(Sigma), and the absorbance at 420 nm arising from the β-galactosidase cleavage of ortho-nitrophenyl-β-galactosidase was monitored. The calculation of the resulting Miller units were performed following previously published methods.[44] Independent replicates were carried out by repeating the initial transformation with independently selected clones for each construct and following the subsequently described methods.

Expression and Purification of E. coli Lon

E. coli Lon protease (pBAD33::EcLon) was obtained from Addgene (pBAD33.Lon was a gift from Robert Sauer, Addgene plasmid # 22145; http://n2t.net/addgene:22145; RRID/Addgene_22145) and expressed and purified essentially as previously described.[45] EcLon was expressed in E. coli strain DH5α, which was grown to an OD600 of 0.8−1 prior to induction by the addition of arabinose to a final concentration of 0.2%. Protein expression was performed at 23 °C with moderate shaking for 4−8 h prior to harvesting by centrifugation. Cell pellets were resuspended in ice-cold 100 mM phosphate buffer pH 6.4, 1 mM EDTA, 1 mM DTT, 20% glycerol and lysed using a high-pressure homogenizer (Emulsiflex). Purification was performed using a batch affinity method with phosphocellulose resin (Whatman). Washing buffers used increasing phosphate concentrations until elution with 400 mM phosphate buffer pH 6.4, 1 mM EDTA, 1 mM DTT, 20% glycerol. The eluted protein was concentrated using a 30 kDa MWCO concentrator (Amicon) and further purified by SEC on a HiPrep 16/60 Sephacryl S400 HR column (GE Healthcare) pre-equilibrated in 50 mM HEPES pH 7.5, 1 mM DTT, 1 mM EDTA, 20% glycerol.

***In vitro* Degradation of the ParDE1 Complex by EcLon**

Purified EcLon activity was confirmed by monitoring the degradation of casein (data not shown), essentially as previously described.[45] A 5× Lon assay buffer was prepared composed of 125 mM Tris-HCl pH 7.5, 500 mM KCl, 50 mM MgCl2 10 mM DTT, 50 mM ATP. Casein protein was prepared at 4.5 mg/mL in 50 mM HEPES pH 7.5, 50 mM NaCl. 100 μL assays were incubated at 37 °C with final concentrations of 5 μM EcLon, 0.5 mg/mL casein, 1× Lon assay buffer and monitored by gel electrophoresis.

Lon degradation of both WT and I68A PaParD1 and PaParDE1 complexes was performed in both the presence and absence of an ATP regeneration system utilizing pyruvate kinase and phosphoenolpyruvate (PEP).[45] A 5× ATP regeneration assay buffer was prepared composed of 125 mM Tris-HCl pH 7.5, 500 mM KCl, 50 mM MgCl2, 10 mM DTT, 10 mM ATP, 50 U/mL pyruvate kinase, 50 mM PEP. 100 μL reactions for both WT and I68A ParDE1 complexes (final concentration 0.5 mg/mL) were incubated with 5 μM EcLon at 37 °C, and degradation was monitored by gel electrophoresis at 30 min, 1 h, and 24 h (see Figure S2.4).

RESULTS

Structural Similarities of ParDE Complexes and Their Interaction Surfaces

The structure of the P. aeruginosa PaParDE1 complex was determined by X-ray crystallography to a resolution of 1.77 Å (PDB ID: 6XRW, see Table S2.2). The crystallographic asymmetric unit consists of two PaParD1−PaParE heterodimers, but these are not paired into the relevant tetrameric biological unit (Figure 2.1A). Instead, the biological heterotetramer is generated by a crystallographic two-fold axis of symmetry and consists of a PaParD1 dimer, with each PaParD1

bound to a single PaParE1 molecule, resulting in an overall Par(E1)1-(D1)2-(E1)1 architecture (Figure 2.1B). Within the asymmetric unit, a ParE1−ParE1 interface is bridged by a well-ordered 28-atom long polyethylene glycol (PEG) molecule (Figure 2.1C). This PEG molecule is associated with a small cavity formed from the interaction of two PaParD1 α3 helices and two PaParE1 N-terminal helices. This small cavity has an additional small molecule with well-defined electron density modeled as a benzamidine molecule, likely present from the initial steps of protein purification (Figure 2.1D). At this time, no biological role for these specific crystallization molecules is expected, although they appear essential to crystal packing.

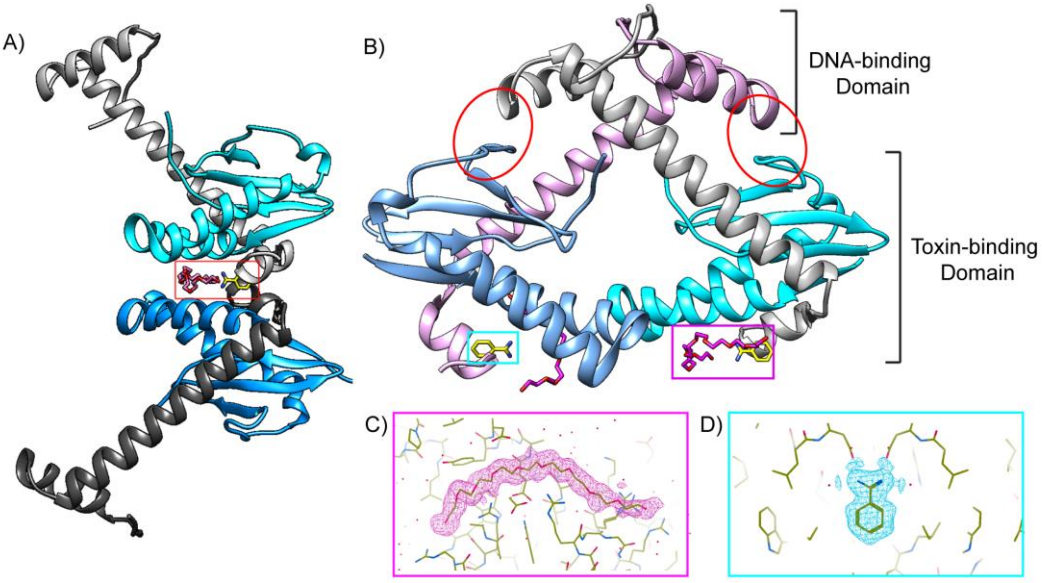

Figure 2.1. Structure of *Pseudomonas aeruginosa* PaParDE1 heterotetramer. A. The asymmetric unit of the PaParDE1 complex contains two PaParD1 chains (grey ribbons) and two PaParE1 chains (blue and cyan ribbons). The red box highlights the presence of polyethylene glycol and benzamidine ligands at a ParE-ParE crystal packing interface. **B.** The biologically relevant heterotetramer of the PaParDE1 complex. Regions of functional significance are noted, including the red circles highlighting a cross-interaction between a PaParE1 toxin with the other PaParD1 chain found in the dimeric antitoxin. **C-D.** A composite OMIT map (contoured at 1σ) of ordered small molecules observed at the PaParE1 crystal packing interface. **C.** polyethylene glycol, **D.** benzamidine.

Comparison of the ParD antitoxins in the four available canonical structures reveals a conservation of dimerization through the N-terminal ribbon-helix-helix (RHH) DNA-binding domain, consistent with the classification as CopG-type transcriptional repressors, but with differences in the overall lengths of the α2 and α3 helices.[19,25,46–48] Both PaParD1 (PDB ID: 6XRW) and *Caulobacter crescentus* (Cc) ParD1 (PDB ID: 3KXE) have considerably shorter α2 helices (48.1 and 46.8 Å, respectively) compared to the two *Mesorhizobium opportunistum* (Mo) ParD structures (PDB ID: 5CEG and a chimeric ParD in PDB ID: 6X0A), which share the same DNA binding domains and have α2 helices of 53.5 Å.[46] Differences in the length of the α3 helices are also noted, with PaParD1 among the shortest at 13.3 Å; *E. coli* (Ec) ParDE (PDB ID: 5CW7) has the longest, measuring just over 30 Å, with CcParDE1 at approx. 17 Å; and MoParD molecules at 21 and 23 Å. This places PaParD1 as the most compact ParD antitoxin structure

known to date. Further, PaParD1 appears to have an unstructured C-terminus, with three amino acids in contact with the toxin beyond the α3 helix (Figures S2.5 and S2.6).

In all structures, the long helix (α2) of the antitoxin and the short C-terminal helix (α3) form the interaction interface with the toxin. Among all the complexes, the antitoxin slots into a surface channel to wrap around the toxin molecule, burying at least 1400 $Å^2$ between the two interacting partners. The complexes from Mo and Ec, however, have a larger buried surface of ≥1500 $Å^2$ mediated largely through a longer ParD α3 helix (Table S2.5, Figures S2.5 and S2.6). The interactions of ParD with ParE all have a generalized hydrophobic nature of the antitoxin-binding path, a property conserved among the RelE/ParE TA family, and of note, there are no water molecules within any of these protein−protein interfaces.[19,25] There are specificity imparting polar interactions, including salt bridges, interspersed along the edges of this hydrophobic path, as was originally identified in the first reported structure (PDB ID: 3KXE).[25] In general, approximately half of the buried surface area is hydrophobic (Table S2.5, Figure S2.5), with the two extremes being the complex from Ec (PDB ID: 5CZE) with only ∼40% of the buried area on ParD being hydrophobic and one of the Mo complexes (PDB ID: 6X0A) at ∼57%.

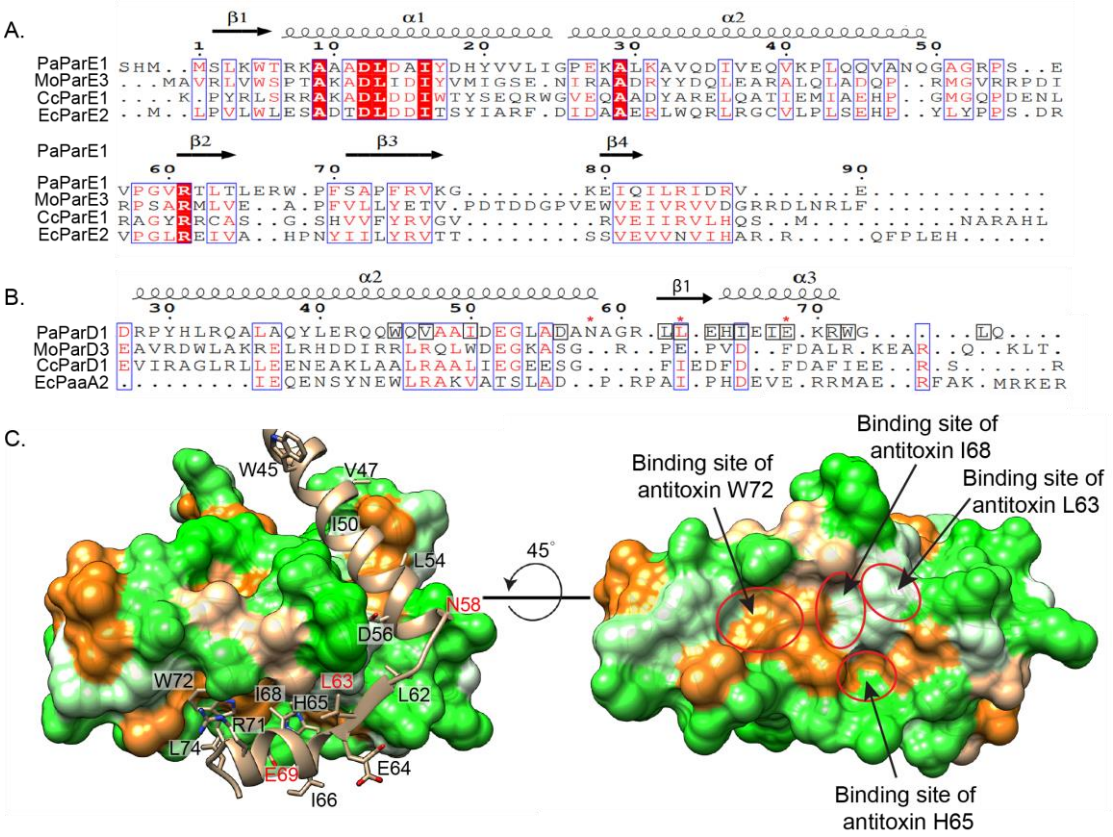

Figure 2.2. Sequence conservation and comparison to the contacting amino acids between PaParE1 and PaParD1. Structure-based sequence alignments of **A.** PaParE1 and **B.** PaParD1 as compared to other ParDE complexes with experimentally determined structures [19,23,25]. Completely conserved amino acids are denoted as white text on a red background, while conservation in 3 of the 4 sequences are in red text. The ParD1 sequence is annotated by black boxes to indicate the amino acids chosen for mutation, and a red asterisk is placed above the amino acid selected for substitution with a stop codon to generate C-terminally truncated PaParD1 proteins. **C.** The molecular surface of a PaParE1 toxin is colored by Kyte-Doolittle hydrophobicity (orange, phobic; green, polar). The PaParD1 antitoxin ribbon is colored tan, and amino acid side chains chosen for alanine substitution are shown and labeled. Labels with red text indicate PaParD1 truncation mutants.

Comparison of the structure-based sequence alignments demonstrates that the ParE toxins contain higher sequence similarity than their cognate ParD antitoxins (Figure 2.2A). The ParE toxins each encode a highly conserved sequence in helix 1 (consensus: AXADLDDI), of which an Asp amino acid is observed to participate in a salt bridge with a C-terminal arginine (or lysine) conserved in the cognate ParD antitoxin in each structure (Figures 2.2B and S2.6). An additional absolutely conserved residue in ParE is an arginine at the start of β2, which is observed to be relatively solvent exposed in each structure.

The interactions between ParE toxins and their cognate ParD antitoxins place the face of the ParE β sheet against the α2 helix of ParD; this interaction appears to be supported by Tyr or Phe amino acids found on ParE β3. ParE β3 and β4 are also enriched with smaller hydrophobic

amino acids, many of which comprise the core of the ParE-like fold (Figure S2.6). The loop in ParD that connects α2 and α3 passes over one edge of the toxin β sheet (Figure S2.5). The α3 helix of ParD sits against the surface generated by the two helices of the toxin (Figure S2.5); and as noted above, this antitoxin α3 helix is significantly shorter in PaParD1 (Figures S2.5 and S2.6). We note prominent cavities are conserved on this surface of the toxins that face the antitoxin α3 helix of ParD molecules, and the volume and distributions appear tailored for interactions with side chains from cognate ParD antitoxins (Figure S2.5).

While the PaParE1 toxin is tightly wrapped by the C-terminus of a PaParD1 molecule, the PaParE1 toxin also makes limited interactions with the other PaParD1 molecule in the biological unit. Two points of contact are evident, one between PaParD1 α1 with a loop in PaParE1 that connects the two α helices with the β strands in the toxin (Figure 2.1B, red circled region) and another with PaParD1 α2 and the C-terminus of PaParE1. Together, these previously unrecognized interactions form an interface with ~360 $Å^2$ of the buried surface per copy in the PaParDE1 complex.

Interaction with PaParE1 Has a Hotspot at PaParD1 Ile68

The PaParDE1 complex structure was used to identify potentially important sites on the α2 and α3 helices of the antitoxin for interactions with the toxin (Figure 2.2). To evaluate their individual contributions, site-directed mutagenesis was employed to exchange 10 hydrophobic residues of PaParD1 (in α2: W45, V47, I50, L54, in the linker region: L62, L63, and in α3: I66, I68, W72, and L74, Figure 2) to alanine, although poor expression of the antitoxin containing L54A substitution precluded further analysis. Five additional alanine substitutions were made at polar amino acids (in the linker region: D56, E64, and in α3: H65, E69, and R71, Figure 2.2), yielding a total of fourteen positions probed along the PaParD1 protein. These mutated antitoxin proteins were used to evaluate the kinetics of binding and thus derive an equilibrium dissociation constant (K_d) for interaction with PaParE1. These were compared to the previously published values for the WT antitoxin, with a K_d value of 152 pM (Table S2.3).[22]

The tight interaction of these proteins approaches the limit of detection for k-off; however, thirteen of the fourteen single point mutants showed no significant difference in binding kinetics (p-value < 0.05, one-way ANOVA) from that obtained with the WT PaParD1 (traces and analysis, Figures 2.3 and S2.7, Table S2.3). Further, size-exclusion elution profiles of these PaParD1 point mutants in complex with PaParE1 were identical to WT (data not shown), verifying that a stable complex was formed. The point mutation at Ile68 (I68A), however, has altered the binding behavior that both weakens the interaction and no longer conforms to a 1:1 Langmuir model of binding (Figure S2.8). The binding is instead parsed into two binding conformations per PaParD1 chain (a 2:1 heterogeneous ligand model), where one type of interaction has a considerably faster off-rate (p-value < 0.0001) compared to the WT interaction (Figures 2.3 and S2.7, Table S2.3) and thus a K_d value of 626 ± 468 nM, while the other has a slower on-rate, resulting in a K_d value of 25.5 ± 2.2 nM.

PaParD1 I68A Hotspot Has a Minimal Effect on Affinity When Antitoxin Is Rendered Monomeric

We reasoned that additional contributions to binding may arise from some uncharacterized cooperativity within the dimeric ParD, or potentially from cross-interactions of the PaParE1

toxin with the other PaParD1 monomer in the biologically relevant tetramer noted in the crystallographic packing (Figure 2.1B). To address this, N-terminal truncations of PaParD1 were produced, removing residues 1−41 encompassing the DNA-binding and dimerization domains of PaParD1; however, the resulting PaParD1$_{42–75}$ construct was insoluble. Therefore, both WT and I68A PaParD1 were fused to the C-terminus of the fluorescent protein mCherry to generate mCh-ParD1$_{42–75}$ and mCh-I68A ParD1$_{42–75}$ (Figure 2.3). These were both confirmed to be monomeric by SEC analysis (not shown). A lack of contributions from the mCherry fusion was verified by repeating the BLI assays with mCherry fused to full length ParD1, resulting in K_d values approximating the unfused WT PaParD1 interaction profile (225 ± 6.8 pM) (Figures 3 and S2.1, Table S2.3), as well as the mCherry protein alone, which demonstrated a lack of interaction. The equilibrium dissociation constant (K_d) for the truncated monomeric mCh-PaParD1$_{42–75}$ was determined to be essentially equivalent to the WT full length protein, at 828 ± 550 pM (Figures 3 and S1, Table S3). Like the full-length I68A PaParD1 mutant, the monomeric mCh-I68A PaParD1$_{42–75}$ mutant required fitting using a 2:1 heterogeneous ligand model. Two equilibrium constants of dissociation were determined for the mCh-I68A PaParD1$_{42–75}$ mutant: K_{d1} was determined to be 29.06 ± 9.39 nM, while K_{d2} was determined to be 2.23 ± 1.95 nM (Figures 2.3 and S2.1, Table S2.3). While these values are still increased relative to the WT values, they are not statistically significant. However, the K_{d1} value of mCh-I68A ParD1$_{42–75}$ is significantly different from the full-length I68A ParD1 mutant. This indicates that the impact of the I68A mutant on affinity is likely most attributable to altering the nature of the interactions within the heterotetramer rather than the loss of specific atomic contacts.

C-Terminal Seven Amino Acids of PaParD1 Are Required to Form a Complex with PaParE1

Concomitant with our analysis of individual amino acid contributions to the interaction affinity, C-terminal truncations of the antitoxin were made to determine if it was required to establish a stable complex with PaParE1. Using site-directed mutagenesis, stop codons were created to replace residues N58, L63, or E69 (Figure 2.2). Based on BLI experiments and confirmed by SEC, none of these truncation mutants were able to form a complex with WT PaParE1 (Figure 2.4). For the truncation at amino acid 58, this was not surprising, as all of the last interacting helix were removed (α3, Figure 2.2). However, the abolishment of interaction with a truncation at amino acid 69 removes only a minimal part of the last helix. Of the truncated amino acids of E69X PaParD1, W72 and L74 form hydrophobic interactions with PaParE1. Additional contacts within this truncated region of PaParD1 are a polar interaction between E69 of ParD1 and K41 of PaParE1, as well as a polar interaction between R71 of PaParD1 with D14 of PaParE1. Single point mutations of each of these antitoxin residues had no impact on affinity by BLI (Figures 2.3 and S2.1, Table S2.3).

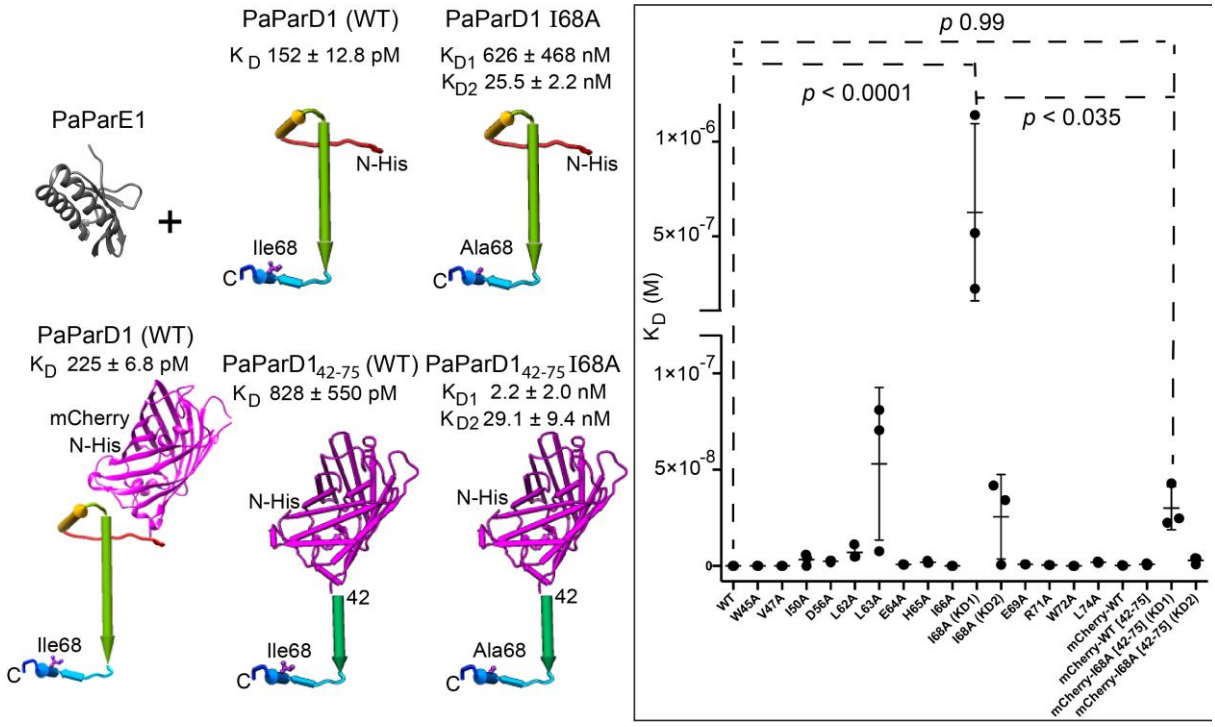

Figure 2.3. Mutation of antitoxin PaParD1 amino acid Ile68 to Ala decreases the interaction affinity, while no other individual antitoxin amino acids alter the affinity of interaction with PaParE. Comparison of equilibrium values for K_d, as determined by BLI experiments, reveals that PaParD1 I68A decreases the affinity and is statistically significant, even when the dimeric region of PaParD1 is removed (replaced by mCherry to maintain solubility of constructs). The binding of PaParE1 to I68A PaParD1, however, is parsed into two different types of interactions. Removal of the dimeric region of ParD, however, restores both I68A binding interactions to within the range for WT. Kinetic on and off rates are graphed in **Fig. S2.7**, average values ($n \geq 3$) for each parameter are given in **Table S2.3**, and traces with residuals for each BLI experiment are given in **Fig. S2.1**.

Altered Interactions with PaParD1 Are Recapitulated in Bacterial Cells

To assess the potential impacts of other cellular contents on the interactions of PaParD1 and PaParE1, the I68A and E69X constructs were generated for testing in a bacterial two-hybrid (BACTH) system. Each construct contained either the T25 or T18 fragments of the adenylate cyclase protein at the N-terminus of PaParD1 (WT, mutant, or truncation) and/or of PaParE1 (Figure 2.5). As we previously noted,[22] the PaParE1 toxin is attenuated with respect to toxicity, which allows for expression in the absence of antitoxin in the BACTH system. Each construct was tested by spotting onto media with a colorimetric indicator (X-Gal) and by measurement of the Miller units of β-galactosidase activity resulting from an overnight induction. To ensure the detected interactions were protein-specific, each construct was also screened against an "empty" vector control, and this routinely yielded white colonies, as well as in the opposite vector orientation (fused to either T18 or T25 fragments) (Figure S2.3).

BACTH revealed that WT PaParD1 interacts strongly with PaParE1, evident by blue colonies and Miller units of 3600− 4000, as expected for an *in vitro* apparent K_d of 152 pM. The interaction of I68A PaParD1 with WT PaParE1 results in a lighter blue colony than the WT

interaction. Quantitation of Miller units reveals an approximately 2- to 4-fold decrease of the PaParE1 interaction with I68A PaParD1, as compared to the WT PaParD1 interaction with PaParE1 (Figures 2.5 and S2.3), which is consistent with the biophysical measurements. This demonstrates that the observed *in vitro* impact on binding of mutating amino acid Ile 68 of PaParD1 has an equivalent impact within a cellular environment, albeit in *E. coli* rather than the native host *P. aeruginosa*.

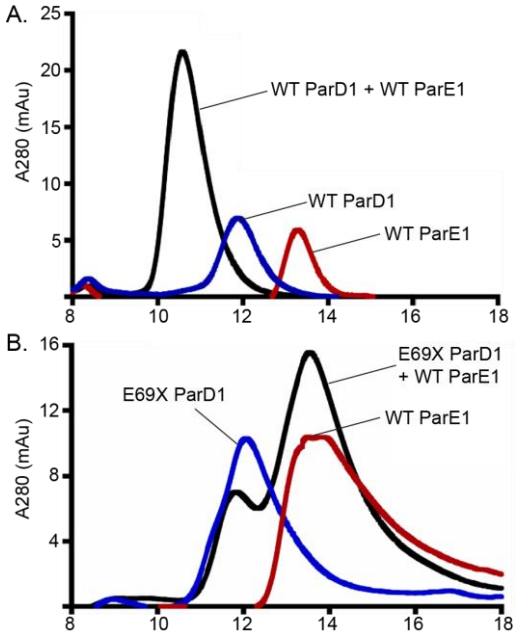

Figure 2.4. Size exclusion chromatography confirms a lack of interaction with PaParD1 antitoxin lacking the C-terminal seven amino acids. The black trace demonstrates the resulting profile when PaParE1 is mixed with either **A.** wild type (WT) or **B.** truncated (E69X) PaParD1. Corresponding traces for either component alone are also shown.

The lack of complexation between PaParE1 and the E69X PaParD1 antitoxin was verified in the BACTH assay format, which revealed white colonies and no Miller units above background (Figures 2.5 and S2.3). Therefore, the interactions of the E69X PaParD1 antitoxin truncation mutant with PaParE1 are also blocked within this cellular environment. Further, these results indicate that the last seven amino acids lacking in E69X PaParD1, which removes all amino acids after the Ile68 amino acid, are required to initiate the interaction with PaParE1.

PaParD1 "Hotspot" Mutation I68A Affects the Secondary Structure and Stability of the Resulting PaParDE1 Complex

To further probe the impact of the PaParD1-I68A mutation's effect on the antitoxin structure and complexation, we determined the secondary structures using FTIR.[49] Secondary structure measurements were performed for each component, as well as purified WT and I68Acontaining complexes (Figure 2.6A, Table S2.4). In the absence of PaParE1, both WT and I68A PaParD1 have essentially identical secondary structure, containing approx. 35−36% α-helical and 28% β-sheet content, indicating that the I68A mutant does not impact the native structure. Upon binding to PaParE1, the WT PaParD1 undergoes a transition, resulting in an increase in α-helical content wherein each PaParD1 monomer contributes six amino acids, and this is consistent with a disorder-to-order transition at the C-terminal α3 helix of PaParD1 (Figure 2.6A, Table S2.4). Interestingly, upon complexation with PaParE1, the PaParD1-I68A mutant shows a larger increase in α-helical content relative to the WT complex (approx. 14 amino acids per PaParD1 monomer), indicating that it adopts an extended α-helical structure upon toxin binding. While we cannot preclude changes to the secondary structure of the ParE molecule, as was previously shown in the structurally related RelE toxin from *E. coli*, ParE toxins lack the region corresponding to the RelE gain of the helical content, and no available structures or models for association support such a change in the ParE structure.[50] The PaParD1 antitoxin is noted to contain a short β strand (L62, L63, E64); however, due to the limitations of FTIR only measuring β sheets, we cannot

speculate whether this region is structured in the absence of or induced by the toxin. Given that few amino acids in the WT complexed PaParD1 antitoxin are not in an α helix, or part of the well-ordered RHH motif, it appears that the additional helical nature of the I68A antitoxin comes from the loop region between α2 and α3, as well as the short β strand (L62, L63, E64).

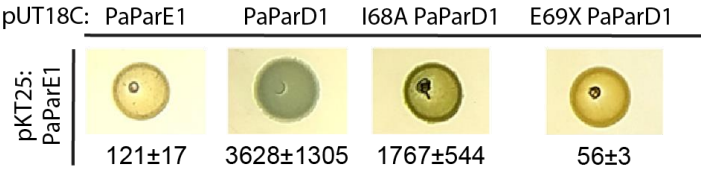

Figure 2.5. A Bacterial Two-Hybrid assay confirms the effects of PaParD1 mutations on complex formation within a cellular environment. Representative images of growth on indicator media are shown, and corresponding Miller units are indicated below each spot. These represent at least three independent transformations with subsequent measurements after an overnight induction. Additional measurements and control samples are given in **Fig. S2.3.**

We verified the association of the I68A PaParD1 mutant with PaParE1 using SEC, which indicates I68A is able to form a complex with PaParE1 *in vitro*. However, a small shift was observed in the elution volume for the I68A containing complex, as compared to the WT complex, suggesting a potential change in interaction (Figures 2.6B and S2.8). The data fitting results of the BLI experiments also suggest a change in binding for the PaParD1-I68A antitoxin (Figures 2.3 and S2.1), including faster off-rates resulting in weaker affinity. To further measure the impacts on the overall structures, we utilized SEC (Figure 2.4). SEC confirms a lack of interaction with PaParD1 antitoxin lacking the C-terminal seven amino acids. The black trace demonstrates the resulting profile when PaParE1 is mixed with either (A) WT or (B) truncated (E69X) PaParD1. Corresponding traces for either component alone are also shown (Figure 2.5). A bacterial two-hybrid assay confirms the effects of PaParD1 mutations on complex formation within a cellular environment. Representative images of growth on indicator media are shown, and corresponding Miller units are indicated below each spot. These represent at least three independent transformations with subsequent measurements after an overnight induction. Additional measurements and control samples are given in Figure S2.3. coupled to MALS to determine the absolute molecular mass of the components and the resulting complexes (Figure 2.6B).

We have previously characterized the PaParDE1 system, identifying a dimeric ParD antitoxin (14.74 ± 1.30 kDa, no affinity tag present) and monomeric toxin (13.5 ± 0.64 kDa) which form a heterotetrameric complex (44.5 ± 1.10 kDa).22 The SEC−MALS results recapitulated these previous measurements for monomeric PaParE1 (13.65 ± 0.18 kDa) and dimeric PaParD1, including for the PaParD1-I68A mutant (22.37 ± 0.38 kDa, with affinty tag, Figure 6B).[22] In addition, a heterotetrameric complex of the WT proteins was measured as 47.15 ± 0.16 kDa, also consistent with previous measurements.[22]

However, the PaParE1 toxin and the PaParD1-I68A mutant antitoxin complex consist of a 38.43 ± 0.38 kDa complex. The light scattering signal clearly indicates a shift in the molecular mass as compared to the WT complex and is interpreted as comprising a mixture of dimeric I68A antitoxin bound to either one or two PaParE1 toxin molecules. The loss of binding to one toxin results from the increased off-rate, which can re-equilibrate as the chromatography progresses. This provides orthogonal BLI and SEC−MALS supporting an impact on the loss of affinity

between the PaParD1 antitoxin and its cognate PaParE1 toxin, likely resulting from altered dynamics and C-terminal antitoxin ordering (measured by FTIR) due to the I68A mutation.

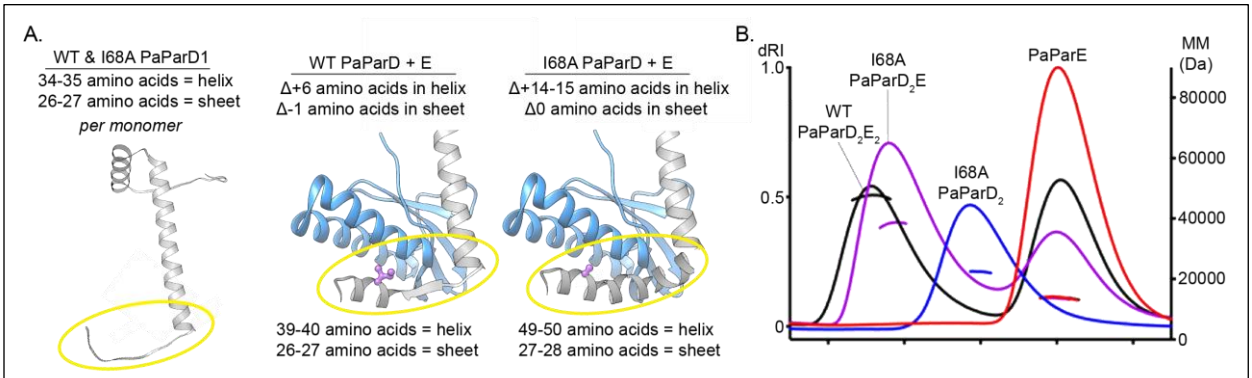

Figure 2.6. The PaParD1 I68A mutation impacts the gain of secondary structure as a function of binding to PaParE1, and results in altered occupancy of PaParE1 within the overall complex. **A.** FTIR measurements were carried out using buffer-matched samples and repeated in triplicate (see Table S2.5 for individual measurements). **B.** SEC-MALS analysis of complex formation with I68A antitoxin and compared to complexes containing wild type PaParD1 antitoxin. The absolute molecular mass (right y-axis, dotted lines overlayed with peak traces) of the complexes were determined in the presences of excess PaParE1 toxin to ensure saturation. Peak traces are plotted from the Refractive Index (dRI) signal. Replicate measurements are shown in **Fig. S2.2**.

Conservation of PaParD1 Ile68 Interaction Site on the Surfaces of ParE Toxins

Of note, this hydrophobic amino acid Ile68 sits in a well-defined hydrophobic cavity on the surface of PaParE1 (Figures 2.2C and S2.9). The I68 binding pocket is formed by the ParE1 residues Trp5, Ala10, Leu13, and Val37 (Figure S2.9). This binding pocket is conserved in two of the other four published structures (PDB ID: 5CZE, 5CEG) (Figure S2.9A,C) and contains conserved hydrophobic interactions. The *E. coli* ParDE complex (PDB ID: 5CZE) contains an additional conserved binding pocket that accommodates a conserved histidine residue ($PaParD1_{His65}$) (Figures 2.2C and S2.9A). In a recently posted description of the ParDE2 complex from V. cholerae, this same pocket is also highlighted as a conserved feature, although coordinates are not yet available to permit a more detailed comparison.[48] The I68 binding pocket on PaParE1 is flanked by two additional well-defined cavities that accommodate the ParD1 residues W72 and H65, neither of which have an apparent role in complex formation as evident by a lack of impact on binding when mutated to alanine (Figures 2.2B, 2.3 and S2.9, Table S2.3).

Altered TA Interaction Increases Accessibility for Lon-Mediated Antitoxin Degradation

A pervasive feature of functional models for type II TA systems is the degradation of the antitoxin protein by the AAA+ ATPases Lon and ClpP.[2,3,13] However, it has been questioned if this degradation is of only the free antitoxin or if antitoxin could also be pulled from a tightly interacting complex with toxin.51 We further extended this question by testing if the Lon protease from *E. coli* (EcLon) was able to degrade PaParD1 *in vitro* when it was complexed to the PaParE1 toxin, and further, if the PaParD1- I68A mutant with weakened interaction affinity could be more readily degraded.

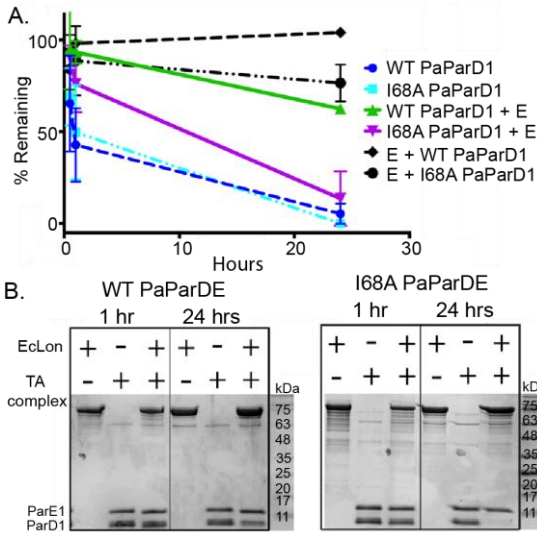

Figure 2.7. The weakened affinity and altered interactions between PaPar1 and PaParD1 I68A permit a more efficient degradation by EcLon *in vitro*. A. The PaParE1 toxin is not degraded, while the free antitoxins (wild type or I68A) are readily degraded. Complexation of antitoxin with toxin, however, offers protection from EcLon cleavage. This protection is directly correlated with the interaction affinity, as the I68A mutant is depleted much more quickly than the wild type antitoxin. **B.** Stained gels of *in vitro* EcLon digestions used for A. Replicates gel images are provided in **Fig. S2.4**.

When the un-complexed "free" PaParD1 antitoxins (WT or I68A) are incubated in the EcLon reaction, they are degraded almost completely by 24 h and appear to have the same kinetics of degradation (Figure 2.7A, blue lines). When a purified complex of PaParDE1 was incubated with EcLon, degradation of the PaParD1 component was evident (Figure 2.7A, green line), but only when an ATP regeneration system was also included in the reaction. This indicates that the relatively slow kinetics of *in vitro* degradation likely arise, in part, due to autoinhibition of EcLon by ADP,[52] while under more ideal *in vitro* conditions, EcLon can access the antitoxin despite its tight interaction (Figure 2.7). When the PaParD1 I68A mutant is used in place of the WT antitoxin in the TA complex, the degradation kinetics increases such that by 24 h almost all of the antitoxin has been consumed (Figure 2.7, magenta line, Figure S2.4). No evidence of degradation of the PaParE1 toxin is observed when bound to either WT or I68A PaParD1 (Figures 2.7 and S2.4). This demonstrates that binding to toxin protects the antitoxin from degradation, such that a higher off rate (resulting from weaker affinity) such as noted for the antitoxin I68A mutation greatly decreases protection and increases the susceptibility of this antitoxin to degradation.

Discussion

Toxin Surface Is Topologically Matched to the Cognate Antitoxin, Including a Conserved Central Cavity Comprised of Toxin Helices 1 and 2

A comparative analysis of the available ParD−ParE interfaces reveals diversity throughout the cognate interactions (Figures 2.2, S2.5 and S2.6). Among these, however, the ParD antitoxins bind to a generally hydrophobic canyon with some specific polar interactions at the periphery of this canyon. These polar interactions include a highly conserved salt bridge between an acidic amino acid in the first helix of the toxin with a basic side chain at the C-terminus of the antitoxin. There are topological features on the ParE toxins that appear to complement the shape of hydrophobic side chains at the most C-terminal part of the cognate ParD antitoxins. A conserved surface cavity on the PaParE1 toxin surface is the binding site for the Ile68 antitoxin residue, which we demonstrate is critically important for both induced structural changes and initiation of binding of the PaParD1 to PaParE1. In addition, we identified a cross-interaction of the PaParE1 toxin with the antitoxin chain of the PaParD1 dimer that is not wrapped around the extensive

hydrophobic interface. These interactions are facilitated by a shortened α2 helix which allows for contacts between the RHH motif of one antitoxin with the C-terminal loop of the opposite ParE toxin. While the *in vivo* impact of these specific interactions is not clear, removal of the dimeric nature of the ParD antitoxin, and thus the potential for these interactions to form, lessens the impact of the I68A mutation on affinity while maintaining the presence of two distinct types of binding.

Kinetics of Interaction Support a Disorder-to-Order Transition upon Binding and Suggest How a Form of Conditional Cooperativity May Rely on Dimeric Antitoxin Within a TA Complex

The association rates for the PaParE1 toxin with the PaParD1 antitoxin and mutants thereof are relatively slow, consistent with a conformational change at the antitoxin C-terminus during association.[53] For related types of effector immunity pairs, such as used in type VI secretion systems, they typically have comparable overall affinity to the ParDE systems but with much faster on-rates; this may relate directly to the functional need to quickly and tightly interact with cognate toxins as protection from assault.[4,54] In contrast, TA systems must essentially be initiating interactions co-translationally.[3,6] Our data further support this model by localization of the "seeding" portion of interaction to the C-terminal of the antitoxin and the N-terminal of the toxin, which follows the order of the encoding operon. It is the folding of the antitoxin C-terminus upon binding that results in the high shape complementarity (CSS value) for the TA complexes, calculated as ≥0.9 for the ParDE structures, and where a value of 1.0 indicates a perfect fit.[55]

The WT interaction has very slow, to essentially unmeasurable, off rates of binding. In earlier studies, we were able to capture this rate for the WT antitoxin protein likely due to a now recognized intrinsic degradation of purified PaParD1.[56] Some minor content of degraded PaParD1 in the reaction would facilitate changes in binding kinetics; however, the tight interaction in either situation is in the approx. 150 pM K_d range. While essentially non-exist off rates favor the model of irreversible interactions, such that an antitoxin is unlikely to be degraded from a complex with its cognate toxin,[51] the I68A antitoxin point mutation is able to reduce affinity from pM to nM by altering the induced structural transition. Further, this effect is only present in a dimeric ParD antitoxin, as rendering the antitoxin monomeric essentially reduces the effect to a non-significant modest change. A reasonable interpretation is that the binding of a toxin molecule to one of the chains of a ParD dimer impacts the ability of the other antitoxin chain to undergo a structural transition and thus weakening the binding to the second ParE toxin. This highlights that external factors that perturb the interaction could feasibly alter or tune the interaction strength by similarly impacting this transition required for tight association.

While the PaParE1 Toxin Protects the PaParD1 Antitoxin from Degradation, the Kinetics of Their Interaction Ultimately Dictates Antitoxin Accessibility to Protease Digestion

The altered conformations upon binding imparted by the I68A mutation is also strongly supported by our *in vitro* Lon protease degradation assays, which demonstrates an increased removal of the I68A PaParD1 antitoxin from complexation with toxin, relative to the WT antitoxin. Under these idealized *in vitro* conditions, PaParD1 was eventually digested even in the presence of PaParE1 toxin. It is tempting to speculate that the protease system was powerful enough to pull apart the picomolar interaction with the PaParE1 toxin, and more so that the

weakened interaction with I68A was more easily parted. However, a simplified calculation using only the measured off rates (ignoring reassociation, which must be occurring, albeit slowly) and the number of molecules in the reaction results in theoretically essentially full removal of even WT antitoxin over the 24 h incubation time. The altered binding of the I68A antitoxin mutant, then, becomes critically important to the interpretation of this assay. While we note altered on rates and differences in the secondary structure associated with a disorder-to-order transition during association, the altered conformations adopted upon binding are also responsible for faster off rates, resulting in less toxin-mediated protection for I68A. Therefore, the increased degradation of the I68A antitoxin most likely results from the impact on the disorder-to-order transition that propagates to faster off-rates for this interaction.

It has been previously reported that toxin molecules can protect their cognate antitoxins from degradation, although the DinJ−YafQ system appears to be an exception.[27] Protection was identified in the kis−kid system and in the ParDE system from the RK2 plasmid, both of which are targeted for degradation by the ClpAP protease.[9,37] Interestingly, for the RK2 ParDE system, the chaperone ClpA could bind to the antitoxin even when it was complexed with toxin, and over longer time scales the antitoxin could be degraded,[9] very similar to what we observe for PaParDE1. For RK2 ParD, signature sequences for ClpA targeting were identified; some weak similarity may be present in the PaParD1 sequence but are located in the DNA binding region (not shown).[9] Another difference in these ParD molecules is that the RK2 ParD toxin binding region was demonstrated to be highly unstructured (PDB ID: 2AN7),[57] as is the ParD2 from *V. cholerae*,[48] in contrast to our measurements of the secondary structure for PaParD1 that indicate a modest gain of α-helical content (6 amino acids out of 75 total) upon complexation with PaParE1. The ParD from the CcParDE1 complex was also noted to be structured in the absence of ParE.[25] This intrinsic feature of ParD antitoxin may dictate the recognition and subsequent binding by specific proteases in the cell. The protease that natively degrades the PaParD1 antitoxin has not been identified, and we cannot exclude recognition by multiple proteases as found for the tripartite paaA−ParE systems in E. coli.[23] Our experiments using the Lon protease from E. coli, therefore, may not represent the kinetics of the native cellular environment but do support a direct correlation with toxin protection and thus TA affinity.

Molecular Model for ParD Antitoxin−ParE Toxin Interactions

For PaParDE1, we have determined that the last seven amino acids are critical to initiate the interaction, although when we individually mutate each of the contacting residues to Ala in the context of the full length PaParD1, they did not significantly impact complexation or affinity. Within this region is a conserved electrostatic interaction between ParE α1 (Asp14) and ParD α3 (Arg71). We systematically mutated each of the contacting positions of PaParD1 in these C-terminal seven amino acids (E69A, R71A, W72A, and L74A), and no single point mutant affected the kinetic rates or overall affinity. Therefore, the loss of association upon C-terminal truncation of PaParD1 must be from the loss of multiple required interactions. It is striking, however, that the remaining 20 sites for interaction in this truncation mutant were not able to mediate any association, even at a weakened affinity.

Overall, it is clear for the PaParDE1 complex that the C-terminus of PaParD1, including part of α3 and the most C-terminal coil, initiates the association reaction. A similar requirement for the antitoxin C-terminus in assembly was previously identified for the DinJ−YarQ system from *E.*

coli.[27] For the unique truncated antitoxin, called paaA, which is comprised only of the equivalent of a truncated α2 and the connecting loop with α3, interaction specificity was found to be encoded in the C-terminal α3.[23] Other studies have examined the specificity of interactions in ParDE systems through the lens of protein sequence co-evolution.[19,46] Critical positions for specificity in the ParD antitoxin of two M. opportunism systems were identified in the last four amino acids of α2 as well as in the unstructured linker.[19,46] Extrapolating from these previous publications and our current results, then, we reason that in a cellular setting, the PaParD1 antitoxin must be essentially completely translated prior to any interaction with the PaParE1 toxin.

This leads us to suggest that the PaParD1 interaction with PaParE1 undergoes a disordered-to-ordered sequential binding, initiated perhaps by the noted conserved electrostatic interaction within the C-terminal seven antitoxin residues. The interaction is stabilized or further directed by other contacts with the C-terminal seven amino acids that culminate at the hotspot position Ile 68. This site appears to serve as a "positioning factor", concomitant with the induced helical formation for the antitoxin C-terminus. Given the tight interaction of WT proteins, such an order or cooperativity of antitoxin binding to toxin may be hidden within the speed of association. By diminishing the interaction strength, we have slowed the association and allowed capturing of these discrete events. Specifically for PaParD1, our data suggest that (1) the interaction is seeded by the C-terminal antitoxin amino acids, although the contribution of each individual contact is limited; (2) Ile68 is a critical position for interaction with a conserved toxin surface topology, triggering a subsequent gain in the secondary structure, whereas a less ideal contact with toxin perhaps allows more torsional freedom to gain additional secondary structure for PaParD1; (3) antitoxin α2 is secondary to the interaction affinity and is not involved in initiating the interaction or in the disorder to order transition; and (4) the dimeric nature of the antitoxin exacerbates the requirement for precise interactions associated with the disorder to order transition.

The identification of a hotspot for TA interactions demonstrates that vulnerable sites for interfering with preformed complexes exist, such that a small molecule could be designed to intercalate into the identified toxin crevices and artificially weaken the interaction of complexes. The current work contributes to an overall model of type-II TA system complex formation and subsequent stability, which directly correlates to protection from proteases, and that is contingent on the antitoxin C-terminus. Further, the high shape complementarity between cognate ParDE pairs combined with the essential role indicated for the equivalent of antitoxin I68 position permits the prediction of interactions of noncognate pairs, an area of active and on-going interest in TA system functionality.[14]

Data Availability

All data are included in this manuscript and supplement document; DNA clones for constructs made in this work are available upon request.

Associated Content

Supporting Information

The Supporting Information is available free of charge at https://pubs.acs.org/doi/10.1021/acs.biochem.1c00584. Additional details on experimental methods (primer sequences), as well as tables of specific values for results and images and replicates for experiments (PDF).

Accession Codes

Information for the proteins used in this work is available online (PaParD1, UniProtKB Q91707 and PaParE1, UniProtKB Q91708); the coordinates and structure factors have been deposited and assigned the Protein Databank identifier 6XRW.

Author Contributions

K.J.S. collected all data except the BACTH, L.L.M. collected BACTH data; K.J.S. and C.R.B. participated in the project design, data analysis, manuscript drafting, and editing. All authors have approved the submitted version. Funding Research reported in this publication was supported by an Institutional Development Award (IDeA) from the National Institute of General Medical Sciences of the National Institutes of Health under grant number P20GM103640 (PI: A West, Project Leader: CRB) and an award for project number HR17- 099 from the Oklahoma Center for the Advancement of Science and Technology (to CRB). The content is solely the responsibility of the authors and does not necessarily represent the official views of the National Institutes of Health. Financial support was also provided from the Office of the Vice President for Research and the Office of the Provost, University of Oklahoma. Notes The authors declare no competing financial interest.

Acknowledgments

We appreciate the assistance of Tamiko Murphy in generating and analyzing a sub-set of PaParD1 mutants, as well as lab members for helpful discussions. We are grateful for the Price Family Foundation Institute of Structural Biology for providing access to the Biolayer Interferometry unit, and to the Rajan lab (OU) for access to the Multiangle Light scattering equipment. We appreciate the assistance of the OU Protein Production and characterization core facility for assistance with purification. The OU Protein Production and Characterization Core facility is supported by an Institutional Development Award (IDeA) from the National Institute of General Medical Sciences of the National Institutes of Health under grant number P20GM103640. We appreciate the expert assistance of Dr. Leonard Thomas for X-ray data collection and analysis, which was carried out at the Biomolecular Structure Core-Norman facility. The BSC-Norman is supported in part by an Institutional Development Award (IDeA) from the National Institute of General Medical Sciences of the National Institutes of Health (award P20GM103640), the National Science Foundation (award 0922269), and the University of Oklahoma Department of Chemistry and Biochemistry.

References

(1) De Las Rivas, J.; Fontanillo, C. Protein-protein interactions essentials: key concepts to building and analyzing interactome networks. PLoS Comput. Biol. 2010, 6, No. e1000807.
(2) Harms, A.; Brodersen, D. E.; Mitarai, N.; Gerdes, K. Toxins, Targets, and Triggers: An Overview of Toxin-Antitoxin Biology. Mol. Cell 2018, 70, 768−784.
(3) Page, R.; Peti, W. Toxin-antitoxin systems in bacterial growth arrest and persistence. Nat. Chem. Biol. 2016, 12, 208−214.

(4) Li, M.; Le Trong, I.; Carl, M. A.; Larson, E. T.; Chou, S.; De Leon, J. A.; Dove, S. L.; Stenkamp, R. E.; Mougous, J. D. Structural Basis for Type VI Secretion Effector Recognition by a Cognate Immunity Protein. PLoS Pathog. 2012, 8, No. e1002613.
(5) Benz, J.; Meinhart, A. Antibacterial effector/immunity systems: it's just the tip of the iceberg. Curr. Opin. Microbiol. 2014, 17, 1−10.
(6) Ramisetty, B. C. M. Regulation of Type II Toxin-Antitoxin Systems: The Translation-Responsive Model. Front. Microb. 2020, 11, 895.
(7) Ronneau, S.; Helaine, S. Clarifying the Link between ToxinAntitoxin Modules and Bacterial Persistence. J. Mol. Biol. 2019, 431, 3462−3471.
(8) Goormaghtigh, F.; Fraikin, N.; Putrins, M.; Hallaert, T.;ˇHauryliuk, V.; Garcia-Pino, A.; Sjödin, A.; Kasvandik, S.; Udekwu, K.; Tenson, T.; Kaldalu, N.; Van Melderen, L. Reassessing the Role of Type II Toxin-Antitoxin Systems in Formation of Escherichia coli Type II Persister Cells. mBio 2018, 9, No. e00640.
(9) Dubiel, A.; Wegrzyn, K.; Kupinski, A. P.; Konieczny, I. ClpAP protease is a universal factor that activates the parDE toxin-antitoxin system from a broad host range RK2 plasmid. Sci. Rep. 2018, 8, 15287.
(10) Van Melderen, L.; Wood, T. K. Commentary: What Is the Link between Stringent Response, Endoribonuclease Encoding Type II Toxin-Antitoxin Systems and Persistence? Front. Microb. 2017, 8, 191.
(11) Muthuramalingam, M.; White, J.; Bourne, C. Toxin-antitoxin modules are pliable switches activated by multiple protease pathways. Toxins 2016, 8, 214−229.
(12) Loris, R.; Garcia-Pino, A. Disorder- and dynamics-based regulatory mechanisms in toxin-antitoxin modules. Chem. Rev. 2014, 114, 6933−6947.
(13) Brzozowska, I.; Zielenkiewicz, U. Regulation of toxin-antitoxin systems by proteolysis. Plasmid 2013, 70, 33−41.
(14) Tu, C.-H.; Holt, M.; Ruan, S.; Bourne, C. Evaluating the Potential for Cross-Interactions of Antitoxins in Type II TA Systems. Toxins 2020, 12, 422.
(15) Fraikin, N.; Goormaghtigh, F.; Van Melderen, L. Type II Toxin-Antitoxin Systems: Evolution and Revolutions. J. Bacteriol. 2020, 202, No. e00763.
(16) Ahmad, S.; Tsang, K. K.; Sachar, K.; Quentin, D.; Tashin, T. M.; Bullen, N. P.; Raunser, S.; McArthur, A. G.; Prehna, G.; Whitney, J. C. Structural basis for effector transmembrane domain recognition by type VI secretion system chaperones. eLife 2020, 9, No. e62816.
(17) Gerdes, K.; Rasmussen, P. B.; Molin, S. Unique type of plasmid maintenance function: postsegregational killing of plasmid-free cells. Proc. Natl. Acad. Sci. U. S. A. 1986, 83, 3116−3120.
(18) Tandon, H.; Melarkode Vattekatte, A.; Srinivasan, N.; Sandhya, S. Molecular and Structural Basis of Cross-Reactivity in M. tuberculosis Toxin-Antitoxin Systems. Toxins 2020, 12, 481.
(19) Aakre, C. D.; Herrou, J.; Phung, T. N.; Perchuk, B. S.; Crosson, S.; Laub, M. T. Evolving new protein-protein interaction specificity through promiscuous intermediates. Cell 2015, 163, 594−606.
(20) Połom, D.; Boss, L.; Węgrzyn, G.; Hayes, F.; Kędzierska, B. Amino acid residues crucial for specificity of toxin-antitoxin interactions in the homologous Axe-Txe and YefM-YoeB complexes. FEBS J. 2013, 280, 5906−5918.
(21) Fiebig, A.; Castro Rojas, C. M.; Siegal-Gaskins, D.; Crosson, S. Interaction specificity, toxicity and regulation of a paralogous set of ParE/RelE-family toxin-antitoxin systems. Mol. Microbiol. 2010, 77, 236−251.

(22) Muthuramalingam, M.; White, J. C.; Murphy, T.; Ames, J. R.; Bourne, C. R. The toxin from a ParDE toxin-antitoxin system found in Pseudomonas aeruginosa offers protection to cells challenged with anti-gyrase antibiotics. Mol. Microbiol. 2018, 111, 441−454.
(23) Sterckx, Y. G.-J.; Jové, T.; Shkumatov, A. V.; Garcia-Pino, A.; Geerts, L.; De Kerpel, M.; Lah, J.; De Greve, H.; Van Melderen, L.; Loris, R. A unique hetero-hexadecameric architecture displayed by the Escherichia coli O157 PaaA2-ParE2 antitoxin-toxin complex. J. Mol. Biol. 2016, 428, 1589−1603.
(24) Goeders, N.; Van Melderen, L. Toxin-antitoxin systems as multilevel interaction systems. Toxins (Basel) 2014, 6, 304−324.
(25) Dalton, K. M.; Crosson, S. A conserved mode of protein recognition and binding in a ParD-ParE toxin-antitoxin complex. Biochemistry 2010, 49, 2205−2215.
(26) LeRoux, M.; Culviner, P. H.; Liu, Y. J.; Littlehale, M. L.; Laub, M. T. Stress Can Induce Transcription of Toxin-Antitoxin Systems without Activating Toxin. Mol. Cell 2020, 79, 280−292.
(27) Ruangprasert, A.; Maehigashi, T.; Miles, S. J.; Dunham, C. M. Importance of the E. coli DinJ antitoxin carboxy terminus for toxin suppression and regulated proteolysis. Mol. Microbiol. 2017, 104, 65− 77.
(28) Walling, L. R.; Butler, J. S. Structural Determinants for Antitoxin Identity and Insulation of Cross Talk between Homologous Toxin-Antitoxin Systems. J. Bacteriol. 2016, 198, 3287−3295.
(29) Chan, W. T.; Espinosa, M.; Yeo, C. C. Keeping the Wolves at Bay: Antitoxins of Prokaryotic Type II Toxin-Antitoxin Systems. Front. Mol. Biosci. 2016, 3, 9.
(30) Jin, G.; Pavelka, M. S., Jr.; Butler, J. S. Structure-function analysis of VapB4 antitoxin identifies critical features of a minimal VapC4 toxin-binding module. J. Bacteriol. 2015, 197, 1197−1207.
(31) Williams, J. J.; Hergenrother, P. J. Artificial activation of toxinantitoxin systems as an antibacterial strategy. Trends Microbiol. 2012, 20, 291−298.
(32) Roberts, R. C.; Ström, A. R.; Helinski, D. R. The parDE operon of the broad-host-range plasmid RK2 specifies growth inhibition associated with plasmid loss. J. Mol. Biol. 1994, 237, 35−51.
(33) Gucinski, G. C.; Michalska, K.; Garza-Sánchez, F.; Eschenfeldt, W. H.; Stols, L.; Nguyen, J. Y.; Goulding, C. W.; Joachimiak, A.; Hayes, C. S. Convergent Evolution of the Barnase/EndoU/Colicin/ RelE (BECR) Fold in Antibacterial tRNase Toxins. Structure 2019, 27, 1660−1674.
(34) Yuan, J.; Sterckx, Y.; Mitchenall, L. A.; Maxwell, A.; Loris, R.; Waldor, M. K. Vibrio cholerae ParE2 poisons DNA gyrase via a mechanism distinct from other gyrase inhibitors. J. Biol. Chem. 2010, 285, 40397−40408.
(35) Jiang, Y.; Pogliano, J.; Helinski, D. R.; Konieczny, I. ParE toxin encoded by the broad-host-range plasmid RK2 is an inhibitor of Escherichia coli gyrase. Mol. Microbiol. 2002, 44, 971−979.
(36) Yuan, J.; Yamaichi, Y.; Waldor, M. K. The Three Vibrio cholerae Chromosome II-Encoded ParE Toxins Degrade Chromosome I following Loss of Chromosome II. J. Bacteriol. 2011, 193, 611.
(37) Karlowicz, A.; Wegrzyn, K.; Dubiel, A.; Ropelewska, M.; Konieczny, I. Proteolysis in plasmid DNA stable maintenance in bacterial cells. Plasmid 2016, 86, 7−13.
(38) Schägger, H. Tricine-SDS-PAGE. Nat. Protoc. 2006, 1, 16−22.

(39) Liebschner, D.; Afonine, P. V.; Baker, M. L.; Bunkóczi, G.; Chen, V. B.; Croll, T. I.; Hintze, B.; Hung, L.-W.; Jain, S.; McCoy, A. J.; Moriarty, N. W.; Oeffner, R. D.; Poon, B. K.; Prisant, M. G.; Read, R. J.; Richardson, J. S.; Richardson, D. C.; Sammito, M. D.; Sobolev, O. V.; Stockwell, D. H.; Terwilliger, T. C.; Urzhumtsev, A. G.; Videau, L. L.; Williams, C. J.; Adams, P. D. Macromolecular structure determination using X-rays, neutrons and electrons: recent developments in Phenix. Acta Crystallogr., Sect. D: Struct. Biol. 2019, 75, 861− 877.
(40) Emsley, P.; Lohkamp, B.; Scott, W. G.; Cowtan, K. Features and development of Coot. Acta Crystallogr., Sect. D: Biol. Crystallogr. 2010, 66, 486−501.
(41) Pettersen, E. F.; Goddard, T. D.; Huang, C. C.; Couch, G. S.; Greenblatt, D. M.; Meng, E. C.; Ferrin, T. E. UCSF Chimera–a visualization system for exploratory research and analysis. J. Comput. Chem. 2004, 25, 1605−1612.
(42) Robert, X.; Gouet, P. Deciphering key features in protein structures with the new ENDscript server. Nucleic Acids Res. 2014, 42, W320−W324.
(43) Krissinel, E.; Henrick, K. Inference of macromolecular assemblies from crystalline state. J. Mol. Biol. 2007, 372, 774−797.
(44) Zhang, X.; Bremer, H. Control of the Escherichia coli rrnB P1 promoter strength by ppGpp. J. Biol. Chem. 1995, 270, 11181−11189.
(45) Gur, E.; Sauer, R. T. Recognition of misfolded proteins by Lon, a AAA(+) protease. Genes Dev. 2008, 22, 2267−2277.
(46) Lite, T.-L. V.; Grant, R. A.; Nocedal, I.; Littlehale, M. L.; Guo, M. S.; Laub, M. T. Uncovering the basis of protein-protein interaction specificity with a combinatorially complete library. eLife 2020, 9, No. e60924.
(47) Ni, S.; Li, B.; Tang, K.; Yao, J.; Wood, T. K.; Wang, P.; Wang, X. Conjugative plasmid-encoded toxin−antitoxin system PrpT/PrpA directly controls plasmid copy number. Proc. Natl. Acad. Sci. 2021, 118, No. e2011577118.
(48) Garcia-Rodriguez, G.; Girardin, Y.; Singh, R. K.; Volkov, A. N.; Konijnenberg, A.; Sobott, F.; Charlier, D.; Loris, R. Vibrio cholerae ParE2 toxin modulates its operon transcription by stabilization of an antitoxin DNA ruler, 2021. bioRxiv:10.1101/2021.03.22.436508.
(49) Wilcox, K. E.; Blanch, E. W.; Doig, A. J. Determination of Protein Secondary Structure from Infrared Spectra Using Partial Least-Squares Regression. Biochemistry 2016, 55, 3794−3802.
(50) Bøggild, A.; Sofos, N.; Andersen, K. R.; Feddersen, A.; Easter, A. D.; Passmore, L. A.; Brodersen, D. E. The crystal structure of the intact E. coli RelBE toxin-antitoxin complex provides the structural basis for conditional cooperativity. Structure 2012, 20, 1641−1648. London, England:1993
(51) Guegler, C. K.; Laub, M. T. Shutoff of host transcription triggers a toxin-antitoxin system to cleave phage RNA and abort infection. Mol. Cell 2021, 81, 2361−2373.
(52) Thomas-Wohlever, J.; Lee, I. Kinetic Characterization of the Peptidase Activity of Escherichia coli Lon Reveals the Mechanistic Similarities in ATP-Dependent Hydrolysis of Peptide and Protein Substrates. Biochemistry 2002, 41, 9418−9425.
(53) Schreiber, G.; Haran, G.; Zhou, H.-X. Fundamental Aspects of Protein−Protein Association Kinetics. Chem. Rev. 2009, 109, 839− 860.
(54) Hood, R. D.; Singh, P.; Hsu, F.; Güvener, T.; Carl, M. A.; Trinidad, R. R. S.; Silverman, J. M.; Ohlson, B. B.; Hicks, K. G.; Plemel, R. L.; Li, M.; Schwarz, S.; Wang, W. Y.; Merz, A. J.; Goodlett, D. R.; Mougous, J. D. A type VI secretion system of Pseudomonas aeruginosa targets a toxin to bacteria. Cell Host Microbe 2010, 7, 25− 37.

(55) Krissinel, E.; Henrick, K. Inference of Macromolecular Assemblies from Crystalline State. J. Mol. Biol. 2007, 372, 774−797.
(56) Snead, K. J.; Bourne, C. R. Intrinsic Degradation of the Type-II Antitoxin ParD from Pseudomonas aeruginosa, 2021. bioRxiv:10.1101/2021.03.29.437564
(57) Oberer, M.; Zangger, K.; Gruber, K.; Keller, W. The solution structure of ParD, the antidote of the ParDE toxin−antitoxin module, provides the structural basis for DNA and toxin binding. Protein Sci. 2007, 16, 1676−1688.

Chapter III: Intrinsic Degradation of the Type-II Antitoxin ParD from *Pseudomonas aeruginosa*

Kevin J. Snead, Christina R. Bourne

Department of Chemistry and Biochemistry, University of Oklahoma, Norman OK USA

Reprinted from bioRxiv 2021.03.29.437564
Posted March 29, 2021 doi: https://doi.org/10.1101/2021.03.29.437564

The following work was submitted as a preprint to bioRxiv (biology preprint server) and has been reprinted here with minor revisions.

I collected and processed all of the data for the manuscript. All figures were produced by myself. Writing of the manuscript was performed by myself. Editing and feedback was provided by Dr. Christina Bourne.

Abstract

Type-II Toxin Antitoxin (TA) systems are regulated by differential half-lives of the resulting non-secreted proteins, such that the neutralizing antitoxin undergoes continual degradation and replenishment to maintain neutralization of its cognate toxin. Antitoxin proteins are widely reported as labile, including upon purification and *in vitro* storage. During the course of studies on a ParDE TA system we noted a prevalent *in vitro* degradation of the ParD antitoxin. In efforts to combat this for practical use in assays, we characterized parameters impacting the degradation as well as the resulting products. These revealed a mechanism likely mediated by a serine or metal-dependent protease. Using Direct Infusion Mass Spectrometry, the cleavage products were identified as an essentially intact DNA binding region of the antitoxin and with the toxin binding domain completely removed. No other species were identified in the solution, such as a contaminant that may mediate such cleavage. Therefore, while our studies revealed viable strategies to mitigate the *in vitro* degradation they did not identify any protease, leaving open the possibility of a potential auto-catalytic proteolytic activity of the antitoxin proteins.

Introduction

Type-II toxin antitoxin (TA) systems are composed of two proteins that impact of bacterial growth. The toxin is a non-secreted protein that inhibits essential cellular processes, resulting in disruption of normal cell growth. During normal growth conditions, the toxin is neutralized by the formation of a protein-protein complex with a cognate antitoxin protein, which sequesters the toxin from its cellular target.[1,2] TA systems were first identified on plasmids, and were shown to control plasmid inheritance through post-segregational killing of daughter cells lacking the plasmid harboring the TA system.[3-5] Post-segregational killing of plasmid free daughter cells is based on the susceptibility of antitoxins to degradation, resulting in shorter half-lives relative to their cognate toxins, allowing for accumulation of excess free toxin over time.[1] The AAA+ proteases Lon and Clp have been shown to be involved in antitoxin turnover *in vivo*.[6-8]

The antitoxin ParD belongs to the MetJ/Arc transcriptional repressor family (Pfam clan CL0057), and is composed of an N-terminal ribbon-helix-helix (RHH) DNA-binding motif and a C-terminal toxin-binding domain consisting of two alpha-helices (helix 2 and 3) which wrap around the ParE toxin resulting in an extensive protein-protein interaction.[9-14] ParD antitoxins were originally shown to be disordered in the absence toxin binding, resulting in an unstructured toxin binding region, as shown in the NMR structure of the ParD antitoxin from the plasmid RK2.[10] In contrast, a chromosomal ParD from Caulobacter crescentus was shown by circular dichroism to be well-ordered in the absence of its cognate ParE.[9] Secondary structure analysis by Fourier transform infrared spectroscopy of a chromosomal ParD from Pseudomonas aeruginosa indicates the C-terminal alpha-helix (helix 3) is unstructured in the absence of ParE binding (unpublished data). In addition to its intrinsic disorder, the RK2 ParD was shown to undergo *in vitro* degradation upon storage, resulting in highly specific degradation products.[15] It remains unclear as to whether the degradation of RK2 ParD was caused by contamination of co-purifying cellular proteases, or an auto-catalytic function of ParD itself.[15]

The current study examined a similar *in vitro* degradation upon storage of the antitoxin ParD (PA0125) from Pseudomonas aeruginosa with the aim of identifying the role of antitoxin stability in TA system regulation. During these studies we identified that Pseudomonas aeruginosa ParD undergoes highly specific degradation, similar to previous observations of the RK2 plasmid-derived ParD antitoxin.[15] Assays were carried out in the presence of different protease inhibiting reagents, which revealed a moderate impact of an irreversible serine protease inhibitor (PMSF) or in the presence of EDTA. Inclusion of a "complete cocktail" of protease inhibitors, supplemented with EDTA was able to totally block the observed degradation. Based on the cocktail components, and the partial blockage with PMSF or EDTA, it appears the proteolytic cleavage may be mediated by either a serine or metal-dependent protease. Using direct infusion mass spectrometry, we mapped the specific site of antitoxin cleavage and determined that the ParD toxin-binding region is degraded in the absence of ParE toxin, leaving behind the intact DNA-binding domain of ParD.

Experimental procedures

Expression and purification of *Pseudomonas aeruginosa* ParD and ParE

Purified ParD and ParE protein were obtained by following a previously published protocol.[19] To obtain ParDE complex, ParD and ParE were buffered exchanged into 50 mM MES pH 6.0, 300 mM NaCl, 5% glycerol, then mixed in equimolar ratios. The mixed proteins were incubated on ice for 30 minutes prior to purification by size-exclusion chromatography using a Superdex 75 10/300 GL column (GE Healthcare) pre-equilibrated with a 50 mM MES pH 6.0, 300 mM NaCl, 5% glycerol buffer.

In vitro degradation Assay

Purified samples at 300 μM in 50 mM Tris pH 8.5, 300 mM NaCl buffer were incubated as indicated; at designated time points 25 μL was removed, combined with reducing SDS loading dye, and heated at 95°C for 5 minutes. For samples treated with PMSF (1 mM), or protease inhibitor cocktail (Sigma, used at a final 1x concentration), the compounds were added during lysis. EDTA was added to samples after the initial Ni-NTA purification step. PMSF and EDTA were also maintained in purification buffers, while additional protease inhibitor cocktail was

added after the final size-exclusion step. Once all time points for a series were collected, samples were loaded onto 12% acrylamide gels with a Tris-Tricine buffer system[20], separated by electrophoresis, and visualized by staining with Coomassie blue. Relative band intensities were measured using ImageJ[21] (see Figs 3.1-3).

Direct Infusion Mass Spectrometry

Mass spectrometry of intact and degraded WT ParD was performed with a Orbitrap Fusion Tribrid Mass Spectrometer (Thermo Fisher Scientific). Prior to analysis by mass spectrometry, samples were desalted into a 50mM Ammonium bicarbonate pH 6.0 buffer and concentrated to 1 mg/ml. Samples were mixed 1:1 with a solution of 30% methanol, 0.1% acetic acid prior to direct injection into the electrospray ionization source. Data collection was performed using both the ion trap and Orbitrap mass analyzers. Mass spectra were analyzed using the Xcalibur software package (Thermo Fisher Scientific) (see Figs 3.5-6).

Results

Pseudomonas aeruginosa ParD is unstable and prone to *in vitro* degradation

Antitoxins have been reported as disordered or unfolded at the toxin-binding region and, as such, are prone to degradation in the cell; however, there are also observations of an inherent instability of the antitoxin protein even in a purified form.[10,16,17] Throughout the course of these experiments, a marked instability of the purified wild-type ParD antitoxin *in vitro* was noted. To better understand the kinetics of this instability, wild-type ParD was assessed for degradation as a function of storage time by Tris-Tricine PAGE analysis (Fig. 3.1). Monitoring wild-type ParD over a 10-day timeframe reveals that ParD is intrinsically unstable and degrades over time. The rate of degradation is modestly affected by temperature, resulting in a shortened half-life of approximately 2.5 days at both 23°C and 37°C relative to ParD samples stored at 4°C with a half-life of approximately 6 days (Fig. 3.1).

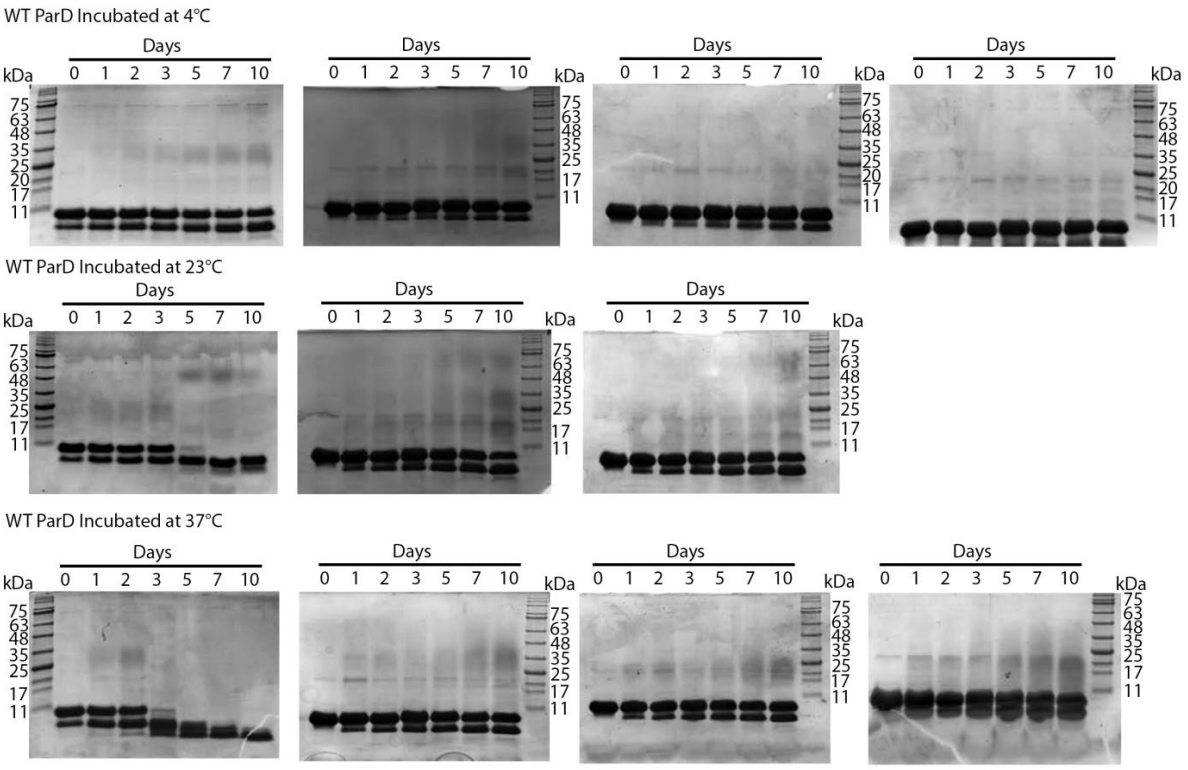

	Day	0	1	2	3	5	7	10
4°C	Normalized	0.0	9.2	15.5	18.1	24.0	28.7	34.2
	Normalized	0.0	3.0	10.0	13.3	21.0	26.0	32.0
	Normalized	0.0	2.4	8.5	14.3	21.9	27.0	33.0
	Normalized	0.0	3.9	2.2	9.8	12.6	22.0	29.7
	Average	**0.0**	**4.6**	**9.1**	**13.9**	**19.9**	**25.9**	**32.2**
	Std Dev	**0.0**	**3.1**	**5.5**	**3.4**	**5.0**	**2.8**	**1.9**
23°C	Normalized	0.0	17.1	23.8	27.8	85.9	100.0	100.0
	Normalized	0.0	17.4	29.0	32.6	41.0	47.0	55.1
	Normalized	0.0	18.2	28.6	33.5	41.6	45.5	52.7
	Average	**0.0**	**14.0**	**21.7**	**24.3**	**43.4**	**48.8**	**52.4**
	Std Dev	**0.0**	**0.6**	**2.9**	**3.1**	**25.8**	**31.0**	**26.6**
37°C	Normalized	0.0	29.7	47.2	100.0	100.0	100.0	100.0
	Normalized	0.0	18.3	26.1	30.4	27.8	44.2	47.1
	Normalized	0.0	16.7	25.2	29.4	36.8	40.5	41.5
	Normalized	0.0	2.4	21.4	23.0	37.5	42.2	40.8
	Average	**0.0**	**16.8**	**30.0**	**45.7**	**50.5**	**56.7**	**57.4**
	Std Dev	**0.0**	**11.2**	**11.7**	**36.3**	**33.3**	**28.9**	**28.6**

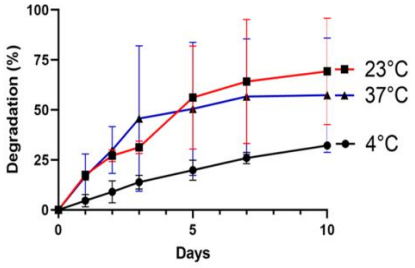

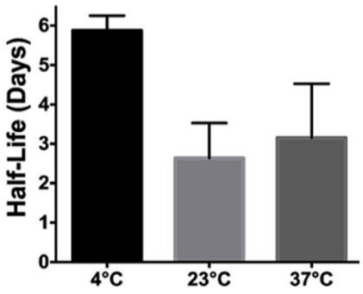

Figure 3.1. ParD degradation shows temperature and time dependence. *In vitro* degradation of ParD was monitored during storage at the indicated temperatures. Band intensities were measured using ImageJ, and degradation was calculated as a percentage of total intensity for each lane, and normalized to account for degradation present in the initial "Day 0" sample. A plot of the resulting values is also given.

Degradation of ParD is blocked by inclusion of EDTA and protease inhibitor cocktail

To gain insight into the catalytic mechanism(s) of ParD degradation, we undertook a series of experiments to characterize potential inhibitors of the observed protein degradation when stored in a 50 mM Tris pH 8.5, 300 mM NaCl buffer. To ensure the observed degradation was not the

result of contamination by fungal or bacterial cells, purified ParD was treated with 0.02% (w/v) sodium azide (NaN3). Addition of sodium azide had a small impact (~ 28% reduction relative to the control sample) when assessed ten days post-purification (Fig. 3.2). While sodium azide had a small impact, the concentration of sodium azide used is sufficient for preventing both fungal and bacterial growth; indicating the degradation is unlikely to be caused by contamination. The metal-chelating compound EDTA was also tested to potentially block the activity of any metal-dependent proteases. The addition of EDTA caused a significant decrease (~ 50% reduction relative to the control sample) in ParD degradation when assessed ten days post-purification (Fig. 3.2). The irreversible serine protease inhibitor partially blocked degradation (~ 40% reduction relative to control sample), while a commercially available protease inhibitor cocktail containing AEBSF, Bestatin, E-64, Pepstatin A, Phosphoramidon, Leupeptin, Aprotinin, and supplemented with EDTA blocked all degradation, showing no increased degradation after the initial "Day 0" time point (Fig. 3.2).

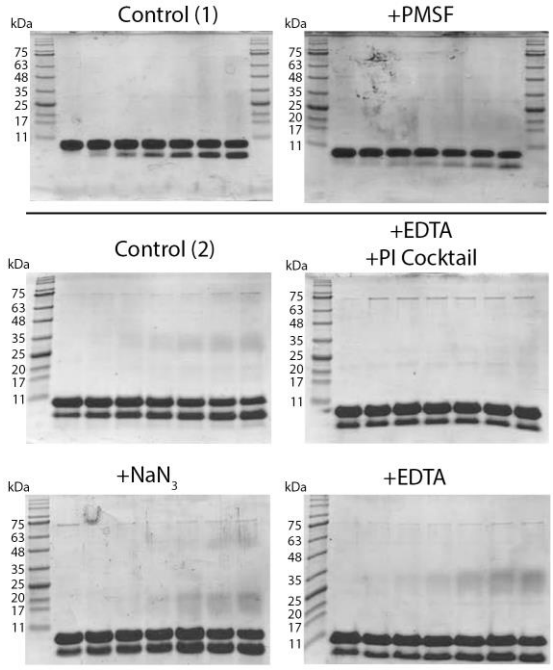

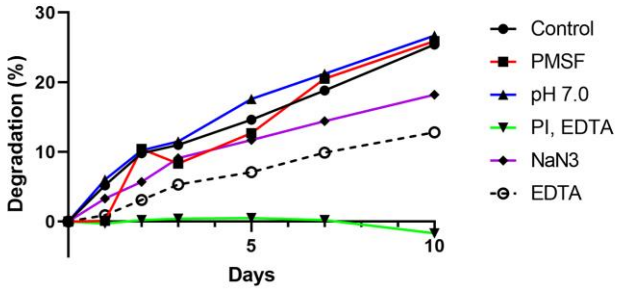

	Day	0	1	2	3	5	7	10	% Reduction
Control (1)	Normalized	0.0	7.3	19.2	24.0	33.4	38.5	43.8	
+PMSF	Normalized	0.0	0.1	10.4	8.3	12.7	20.5	25.9	40.9
Control (2)	Normalized	0.0	5.2	9.8	11.0	14.6	18.8	25.4	
+PI, + EDTA	Normalized	0.0	-0.3	0.2	0.4	0.5	0.2	-1.7	106.7
+NaN3	Normalized	0.0	3.3	5.7	9.1	11.7	14.4	18.2	28.3
+EDTA	Normalized	0.0	0.9	3.1	5.3	7.1	9.9	12.8	49.6

Figure 3.2. ParD degradation is blocked by a protease inhibitor (PI) cocktail. *In vitro* degradation of WT ParD was monitored during storage at 4°C, in the presence of inhibitors of protein degradation. Band intensities for ParD were calculated as a percentage of total intensity for each lane, and normalized to account for degradation present in the initial "Day 0" sample. A plot of the resulting values is also given.

The toxin-binding region of wild-type ParD is degraded in the absence of ParE

Direct-infusion mass spectrometry (DIMS) was utilized to identify the remaining wild-type ParD fragment after degradation. Both degraded and non-degraded samples were directly injected into the ionization source and analyzed by mass spectrometry. Non-degraded wild-type ParD contained two prominent molecular weight species (10731.5 Da and 21462.98 Da), corresponding to ParD monomer and dimer respectively (Fig. 3.3). In comparing the mass spectrum of intact ParD to the resulting spectra of degraded ParD (over the same m/z window), multiple molecular weight species were evident and correlate to cleavage occurring in the region

corresponding to ParD residues 42-47 (42RQQWQV75) (Fig. 3.4), which are located immediately after the ParD dimerization region. The most prevalent species (100% relative abundance) observed is a 5809.5 Da fragment resulting from cleavage at glutamine 46 of ParD (Fig. 3.4). Two additional high abundant species (60% relative abundance) were also observed with molecular weights of 5908.5 Da and 5266.4 Da (Fig. 3.4). The 5908.5 Da fragment results from cleavage at valine 47 of ParD. The 5266.4 Da fragment and an additional 5365.0 Da fragment (30% relative abundance) both result from cleavage at glutamine 43, with the smaller fragment resulting from the loss of the neighboring arginine 42 side chain (Fig. 3.4). These fragments indicate a relatively specific degradation pattern and implies that it could take place in a sequential manner. Further, it appears that the toxin-binding region of ParD is completely degraded, as no peaks corresponding to amino acids after residue 47 were evident, leaving only the ribbon-helix-helix (RHH) DNA binding domain of the antitoxin. These results are consistent with the gel analysis (Figs. 3.1-2), which shows accumulation of a single band of degraded protein, with no other detectable ParD fragments.

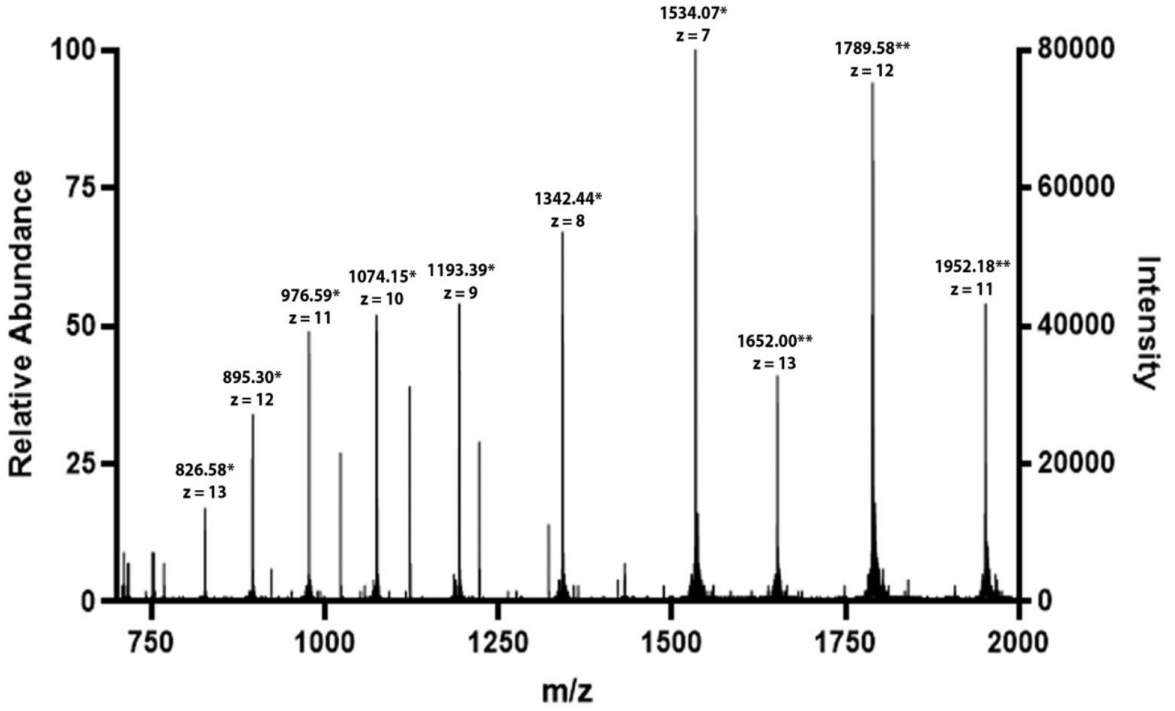

Figure 3.3. Direct infusion mass-spectrometric analysis of wild-type ParD before degradation reveals the major species are monomer and dimer. *Indicates monomeric ParD; **Indicates dimeric ParD. No additional species are evident within this mass window and ionization mode.

Discussion

Inherent instability of antitoxins *in vivo* is a key rationale for the differing half-lives between toxins and antitoxins; however, the explanation for this instability relies on cellular proteases that are presumed absent in our *in vitro* storage experiments.[10,16-18] Wild-type ParD from *Pseudomonas aeruginosa* shows discrete degradation products visible only a few days after purification (Figs. 3.1-2). Similar observations of *in vitro* degradation have been reported for the ParD antitoxin from the RK2 plasmid, where three prominent masses were identified when

analyzed by MALDI-TOF mass spectrometry.[15] Sequence alignment of RK2 ParD and Pseudomonas aeruginosa ParD indicates RK2 ParD contains a homologous sequence (^{43}DQAWQ^{47}) to the cleavage sites we have identified in *Pseudomonas aeruginosa* ParD (^{42}RQQWQV^{47}). The masses of the degradation products seen in RK2 ParD however, do not correspond to cleavage at this site. Instead, analysis of the fragments of RK2 suggests two distinct cleavage events resulting in a 6006 Da fragment corresponding to cleavage at leucine 54, and a 6873 Da fragment corresponding to cleavage at leucine 61. Since both RK2 ParD and Pseudomonas aeruginosa ParD have intrinsically disordered C-termini in the absence of ParE binding, the intrinsic degradation observed may be expected for all unstructured ParD proteins.[10,15] The degradation of ParD can be effectively blocked by inclusion of EDTA or a protease inhibitor cocktail that contains inhibitors of serine, cysteine, aspartic, and metalloproteases. The partial inhibition of degradation by both the irreversible serine protease PMSF and EDTA suggests the degradation may be caused by a combination of a serine and metal-dependent protease.

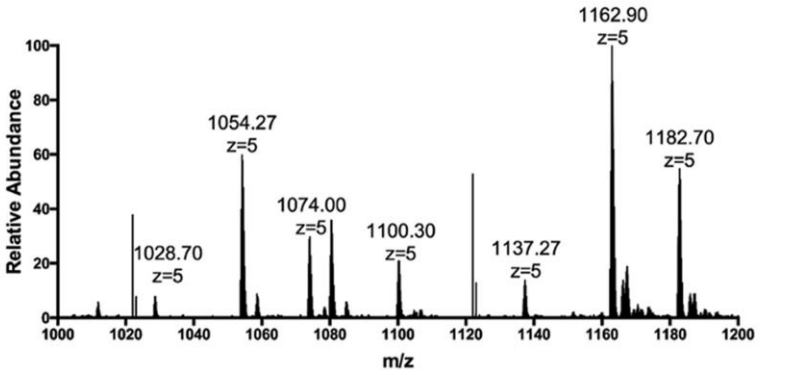

PaParD sequences	Predicted MW	ΔMW	Charge	m/z	MW	ΔMW	Rel. Abundance (%)
.....AQYLERQQWQVAA	6051.82						
.....AQYLERQQWQV **(47)**	5905.98	145.84	5	1182.7	5908.5		60.0
.....AQYLERQQWQ **(46)**	5806.91	99.07	5	1162.9	5809.5	99.0	100.0
.....AQYLERQQW **(45)**	5678.85	128.06	5	1137.3	5681.5	128.0	15.0
.....AQYLERQQ **(44)**	5492.77	186.08	5	1100.3	5496.5	185.0	20.0
.....AQYLERQ **(43)**	5364.71	128.06	5	1074.0	5365.0	131.5	30.0
.....AQYLERQ **(43)**	5264.57	100.14	5	1054.3	5266.4	98.6	60.0
.....AQYLERQ **(42)**	5139.78	124.79	5	1028.7	5138.5	127.9	10.0

*red denontes loss of side chain

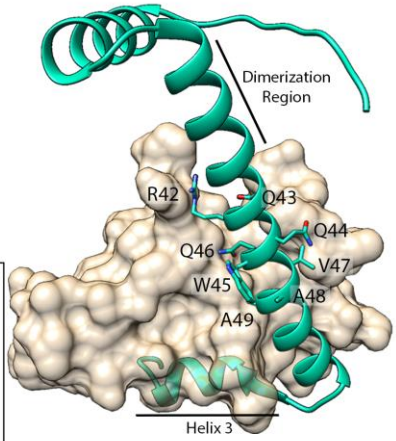

Figure 3.4. Intrinsic degradation of WT ParD results in complete loss of the toxin-binding region. Direct Infusion Mass Spectrometry of degraded ParD, +5 charged species shown (see **Fig. 3.3** for intact WT ParD mass spectrum). (Right) ParD (green) with amino acids corresponding to fragments detected by mass spectrometry displayed on the ParDE complex; ParE toxin is shown as a tan surface (PDB ID: 6XRW).

While evidence points to a either a serine or metal-dependent protease, the species mediating the observed degradation remains unclear. Prior to observing ParD for degradation, extensive purification was performed. ParD was initially purified by IMAC chromatography using a Ni-NTA column; the protein was then desalted to remove imidazole and was treated with thrombin for removal of the N-terminal 6x-His tag. After thrombin cleavage, ParD was passed again over a Ni-NTA column and collected in the flow-through, with any residual contaminants from the first Ni-NTA purification expected to also be retained in this subsequent Ni-NTA purification step. A final size-exclusion step was included to separate ParD from thrombin. Despite these extensive purification steps, purification alone was not sufficient in blocking ParD degradation,

and analysis by direct-infusion mass spectrometry identified peaks attributed to only ParD. The mass spectrometry results reveal that the toxin-binding region is completely absent from degraded antitoxin, and the DNA binding region remains intact. The mass spectrometry results combined with our *in vitro* degradation assays suggest *Pseudomonas aeruginosa* ParD may have latent protease activity that is capable of autocatalytic self-cleavage. If this is also the case *in vivo*, it indicates that it may be possible for the cell to uncouple the transcriptional repression functionality of ParD from its toxin neutralizing function. While this analysis did not provide answers to what was mediating the degradation, as no peaks of significant height were detected other than antitoxin, it does bring an interesting idea of uncoupling toxin binding with DNA binding in an antitoxin molecule, and suggests a potential protease activity for at least some ParD antitoxins.

Acknowledgements
We appreciate the assistance of the OU Protein Production and Characterization core facility for assistance with protein purification. The OU Protein Production and Characterization Core facility is supported by an Institutional Development Award (IDeA) from the National Institute of General Medical Sciences of the National Institutes of Health under grant number P20GM103640. We appreciate the expert assistance of Dr. Steve Hartson for mass spectrometry data collection and analysis, which was carried out at the OSU DNA/Protein Core Facility at Oklahoma State University, Stillwater OK.

Author Contributions
KJS collected all data; both authors participated in the project design, data analysis, manuscript drafting and editing and have approved the submitted version.

Funding
Research reported in this publication was supported by an Institutional Development Award (IDeA) from the National Institute of General Medical Sciences of the National Institutes of Health under grant number P20GM103640 (PI: A West, Project Leader: CRB), and an award for project number HR17-099 from the Oklahoma Center for the Advancement of Science and Technology (to CRB). The content is solely the responsibility of the authors and does not necessarily represent the official views of the National Institutes of Health.

References
1. Harms, A., Brodersen, D. E., Mitarai, N., and Gerdes, K. (2018) Toxins, Targets, and Triggers: An overview of Toxin-Antitoxin biology. Molecular Cell 70, 768-784
2. Page, R., and Peti, W. (2016) Toxin-antitoxin systems in bacterial growth arrest and persistence. Nature Chemical Biology 12, 208-214
3. Roberts, R. C., Ström, A. R., and Helinski, D. R. (1994) The parDE operon of the broadhost-range plasmid RK2 specifies growth inhibition associated with plasmid loss. Journal of Molecular Biology 237, 35-51
4. Gerdes, K., Rasmussen, P. B., and Molin, S. (1986) Unique type of plasmid maintenance function: postsegregational killing of plasmid-free cells. Proceedings of the National Academy of Sciences of the United States of America 83, 3116-3120
5. Ogura, T., and Hiraga, S. (1983) Mini-F plasmid genes that couple host cell division to plasmid proliferation. Proceedings of the National Academy of Sciences of the United

States of America 80, 4784-4788
6. Brzozowska, I., and Zielenkiewicz, U. (2013) Regulation of toxin–antitoxin systems by proteolysis. Plasmid 70, 33-41
7. Dubiel, A., Wegrzyn, K., Kupinski, A. P., and Konieczny, I. (2018) ClpAP protease is a universal factor that activates the parDE toxin-antitoxin system from a broad host range RK2 plasmid. Scientific Reports 8, 15287
8. Muthuramalingam, M., White, J. C., and Bourne, C. R. (2016) Toxin-Antitoxin modules are pliable switches activated by multiple protease pathways. Toxins (Basel) 8, 214
9. Dalton, K. M., and Crosson, S. (2010) A conserved mode of protein recognition and binding in a ParD−ParE toxin−antitoxin complex. Biochemistry 49, 2205-2215
10. Oberer, M., Zangger, K., Gruber, K., and Keller, W. (2007) The solution structure of ParD, the antidote of the ParDE toxin–antitoxin module, provides the structural basis for DNA and toxin binding. Protein Science 16, 1676-1688
11. El-Gebali, S., Mistry, J., Bateman, A., Eddy, S. R., Luciani, A., Potter, S. C., Qureshi, M., Richardson, L. J., Salazar, G. A., Smart, A., Sonnhammer, E. L. L., Hirsh, L., Paladin, L., Piovesan, D., Tosatto, S. C. E., and Finn, R. D. (2019) The Pfam protein families database in 2019. Nucleic Acids Research 47, D427-d432
12. Lite, T.-L. V., Grant, R. A., Nocedal, I., Littlehale, M. L., Guo, M. S., and Laub, M. T. (2020) Uncovering the basis of protein-protein interaction specificity with a combinatorially complete library. eLife 9, e60924
13. Sterckx, Y. G. J., Jové, T., Shkumatov, A. V., Garcia-Pino, A., Geerts, L., De Kerpel, M., Lah, J., De Greve, H., Van Melderen, L., and Loris, R. (2016) A unique heterohexadecameric architecture displayed by the Escherichia coli O157 PaaA2–ParE2 antitoxin–toxin complex. Journal of Molecular Biology 428, 1589-1603
14. Aakre, Christopher D., Herrou, J., Phung, Tuyen N., Perchuk, Barrett S., Crosson, S., and Laub, Michael T. (2015) Evolving new protein-protein interaction specificity through promiscuous intermediates. Cell 163, 594-606
15. Oberer, M., Lindner, H., Glatter, O., Kratky, C., and Keller, W. (1999) Thermodynamic properties and DNA binding of the ParD protein from the broad host-range plasmid RK2/RP4 killing system. Biological Chemistry 380, 1413-1420
16. Loris, R., and Garcia-Pino, A. (2014) Disorder- and dynamics-based regulatory mechanisms in toxin-antitoxin modules. Chemical Reviews 114, 6933-6947
17. De Jonge, N., Garcia-Pino, A., Buts, L., Haesaerts, S., Charlier, D., Zangger, K., Wyns, L., De Greve, H., and Loris, R. (2009) Rejuvenation of CcdB-poisoned gyrase by an intrinsically disordered protein domain. Molecular Cell 35, 154-163
18. Gur, E., and Sauer, R. T. (2008) Recognition of misfolded proteins by Lon, a AAA(+) protease. Genes & Development 22, 2267-2277
19. Muthuramalingam, M., White, J. C., Murphy, T., Ames, J. R., and Bourne, C. R. (2019) The toxin from a ParDE toxin-antitoxin system found in Pseudomonas aeruginosa offers protection to cells challenged with anti-gyrase antibiotics. Molecular Microbiology 111, 441-454
20. Schägger, H. (2006) Tricine–SDS-PAGE. Nature Protocols 1, 16-22
21. Schindelin, J., Rueden, C. T., Hiner, M. C., and Eliceiri, K. W. (2015) The ImageJ ecosystem: An open platform for biomedical image analysis. Molecular Reproduction and Development 82, 518-529

Chapter IV

Kevin J. Snead, Christina R. Bourne

Department of Chemistry and Biochemistry, University of Oklahoma, Norman OK USA

Introduction

Protein-protein interactions are essential for the cellular functions required for life to work. These interactions are required for key cellular functions such as metabolite transport, cell signaling, antibody-mediated immunity, and many more vital functions. Due to the essential nature of protein-protein interactions, they are prime targets for the development of new drugs to treat various diseases.[1,2] One such potential target are type-II toxin-antitoxin (TA) systems, a class of proteins unique to bacteria and archaea. Type-II TA systems are composed of two proteins, a non-secreted metabolic regulator protein (toxin) and a cognate protein which directly binds to and neutralizes toxin activity.[3-6]

During normal cell growth, toxin proteins are neutralized by their cognate antitoxin, which in the case of type-II TA systems the antitoxin is another protein. In type-II TA systems, the toxin protein is neutralized by direct binding and sequestering by its cognate antitoxin.[3-5,7] Studies of the protein-protein interactions of type-II TA systems have shown that the toxin-antitoxin interaction affinity is often in the nM to pM range, indicating very strong protein-protein interactions.[8-11] Multiple studies have been performed to identify protein-protein interaction inhibitors to target these type-II TA systems.[1,2,12-18] Many of these studies have identified either toxin- or antitoxin-derived peptides that bind to the cognate protein and prevent complex formation resulting in accumulation of "free" toxin protein.[12-16,18-20]

The current study examined the ParD1-ParE1 protein-protein interaction interface from the Pseudomonas aeruginosa ParDE1 type-II TA system to determine the minimal antitoxin unit required for toxin binding, in order to identify regions to screen small molecule protein-protein interaction inhibitors against. Using site-directed mutagenesis, N-terminal deletions of PaParD1 were generated to determine the minimal length of ParD1 required to bind to ParE1. A combination of *in vivo* BACTH assays and *in vitro* biophysical measurements utilizing biolayer interferometry were utilized to measure the interaction between ParD1 peptides and ParE1. In combination with previously published results, a ParD1 peptide corresponding to residues 62-75 were identified as the minimal antitoxin unit required for toxin binding. The $ParD1_{62-75}$-ParE1 interface was then used as the search box for *in silico* docking studies to identify potential inhibitors of the ParD1-ParE1 protein-protein interaction.

Experimental Procedures

Expression and Purification of Pseudomonas aeruginosa ParE1 and ParD1 peptides

Wild-type PaParE1 was expressed and purified using previously reported methods.[8,9] To purify PaParD1 peptides, wild-type PaParD1 was cloned into a pET-15b plasmid containing the fluorescent protein mCherry. PaParD1 was cloned as a C-terminal fusion of mCherry, with the

protein sequences linked by a C-terminal 6x-His tag on the C-terminus of mCherry followed by a thrombin cleavage site. ParD1 peptides were generated using Q5 site-directed mutagenesis (NEB) using primers flanking the regions to be deleted. The pET-15b plasmids containing mCherry-6x-His-PaParD1 was transformed into BL21(DE3) *E. coli* cells using a standard heat-shock protocol.

Cells were grown at 37°C in LB media supplemented with carbenicillin, until an OD_{600} of 0.6-0.8. Protein expression was then induced by addition of 1 mM IPTG to the media. The mCherry-ParD1 fusion proteins were induced for 4-6 hours at room temperature with moderate shaking. Cells were harvested by centrifugation and resuspend in a buffer containing 50 mM Tris-HCl pH 8.5, 300 mM NaCl, 40 mM imidazole. The resuspended cells were lysed using a high-pressure homogenizer (Emulsiflex) and pelleted prior to purification. The His-tagged mCherry-ParD1 peptide fusions were purified using a HisTrap FF Ni-NTA column (GE Healthcare), and further purified using a Superdex S75 10/300 (GE Healthcare) pre-equilibrated in 50 mM Tris-HCl pH 8.5, 300 mM NaCl buffer.

Bacterial Two-hybrid Assay

Bacterial two-hybrid assays were performed as previously described.[8] In short, wild-type PaParE1 was cloned into the pKT25 plasmid while wild-type PaParD1 was cloned into the pUT18C plasmid. N-terminal PaParD1 peptides were generated using Q5 site-directed mutagenesis (NEB) using primers flanking the regions to be deleted. The two plasmids were then co-transformed into BTH101 (cya-) E. coli using a standard heat-shock protocol. Cells harboring both plasmids were selected for by growing the cells on LB-agar plates supplemented with kanamycin (50 ug/mL) and carbenicillin (100 ug/mL). Protein-protein interactions were determined by growing the co-transformed cells for 24-hours at 30°C on LB-agar plates supplemented with kanamycin and carbenicillin with X-gal (40 ug/mL) and IPTG (0.5 mM). A positive protein-protein interaction is detected by the formation of blue colonies by reconstitution of an adenylate cyclase enzyme in the presence of X-gal, while white colonies indicate no reconstitution of adenylate cyclase.

The protein-protein interactions were quantified using a kinetic miller assay.[21] In short, the co-transformed cells were grown in LB media, and protein expression was induced with 0.5 mM IPTG, and protein expression was allowed to go overnight. After overnight expression, OD_{600} was measured prior to pelleting. The pelleted cells were resuspended in 100 uL of lysis buffer containing BugBuster (Sigma). The resuspended cells were then serially diluted with lysis buffer. B-galactosidase activity was monitored by the addition of ONPG (1 mg/mL) and measuring absorbance at 420 nm. Initial rates were determined from the linear portion of the A_{420} measurement overtime and were normalized by their OD_{600}. and compared to the empty vector controls. Three biological replicates, each with three technical replicates were performed for kinetic miller assay.

Biolayer Interferometry (BLI)

Biolayer Interferometry assays were performed using previously established protocols.[8] In short, prior to BLI, samples were desalted into a 50 mM Tris-HCl pH 8.5, 300 mM NaCl, 0.5% BSA, 0.05% Tween-20 buffer, and all solutions were matched to these buffer conditions. BLI was performed at 25 °C using an Octet RED96 interferometer (Pall ForteBio) by coupling 100 nM

mCherry-His-ParD1 peptides to Ni-NTA BLI sensor pins. WT-untagged PaParE1 was serially diluted (100 to 3.125 nM) and incubated with mCherry-ParD1-coupled pins until the association reached saturation. Dissociation rates were measured by incubating the pins in a 50 mM Tris-HCl, 300 mM NaCl, 0.5% BSA, 0.05% Tween-20 buffer. Rates were initially calculated by fitting the curves to a 1:1 Langmuir binding model but were ultimately fitted using a 2:1 binding model due to poor fitting of both association and dissociation using the 1:1 model. All fitting was performed with manufacturer-provided BioAnalysis software (v 8.2). Individual curves were analyzed to ensure high quality fits with R^2 values greater than 0.95; individual assays were repeated at least three times to obtain average K_d values.

In silico Docking

In silico docking of a peptidomemetic library (ChemDiv) against PaParE1 was performed using Autodock Vina.[23] The PaParE1 structure was extracted from the PaParDE1 complex structure (PDB: 6xrw) and was prepared using AutodockTools-1.5.6 prior to docking. The search box was limited to the PaParD1 alpha-helix 3-PaParE1 interface. Docking was performed against a rigid receptor (PaParE1) using flexible ligands using default settings for Autodock Vina.[23] The top scoring compounds were initially binned by their structural identifier, and the top scoring representative was selected for each class.

PaParD1 peptides were generated by extracting the PaParD1 structure from the PaParDE1 complex (PDB: 6xrw) followed by deletion of residues 1-61 or 1-64, resulting in peptides corresponding to the C-terminal alpha-helix of PaParD1. These peptides were prepared using AutodockTools-1.5.6 prior to docking against PaParE1. As opposed to the peptidomemetic library, the ParD1 peptides were rigidly docked against ParE1. Binding scores were normalized by their intersurface area and compared to the predicted binding scores of the ParD1 peptides normalized by their intersurface area. ParE1-ligand binding was visualized using UCSF Chimera.[24]

Results

ParD1-derived peptides represent minimal ParD1 unit required for toxin binding

To determine the minimal antitoxin unit required to bind to its cognate toxin protein, we utilized an *in vivo* bacterial two-hybrid (BACTH) assay to assess protein binding. We assayed different lengths of ParD1-derived peptides to determine their ability to bind to wild-type ParE1. Using site-directed mutagenesis (Table S4.1), we generated various N-terminal deletions of ParD1 to create ParD1-derived peptides corresponding to different portions of the toxin-antitoxin interface. N-terminal truncations were utilized since C-terminal deletions of various lengths have previously been shown to abolish toxin-binding.[8] ParD1-derived peptides were fused to the T18 fragment of adenylate cyclase and co-transformed with ParE1 fused to the T25 fragment of adenylate cyclase. Co-transformed cells were spotted on LB-agar plates to visually assess protein binding using the colorimetric indicator X-gal (Fig. 4.1A). ParD1 peptide binding to ParE1 was compared to a leucine zipper and empty vector controls (Fig. 4.1A). To validate the bindings observed, a kinetic miller assay was utilized to measure β-galactosidase activity.[21]

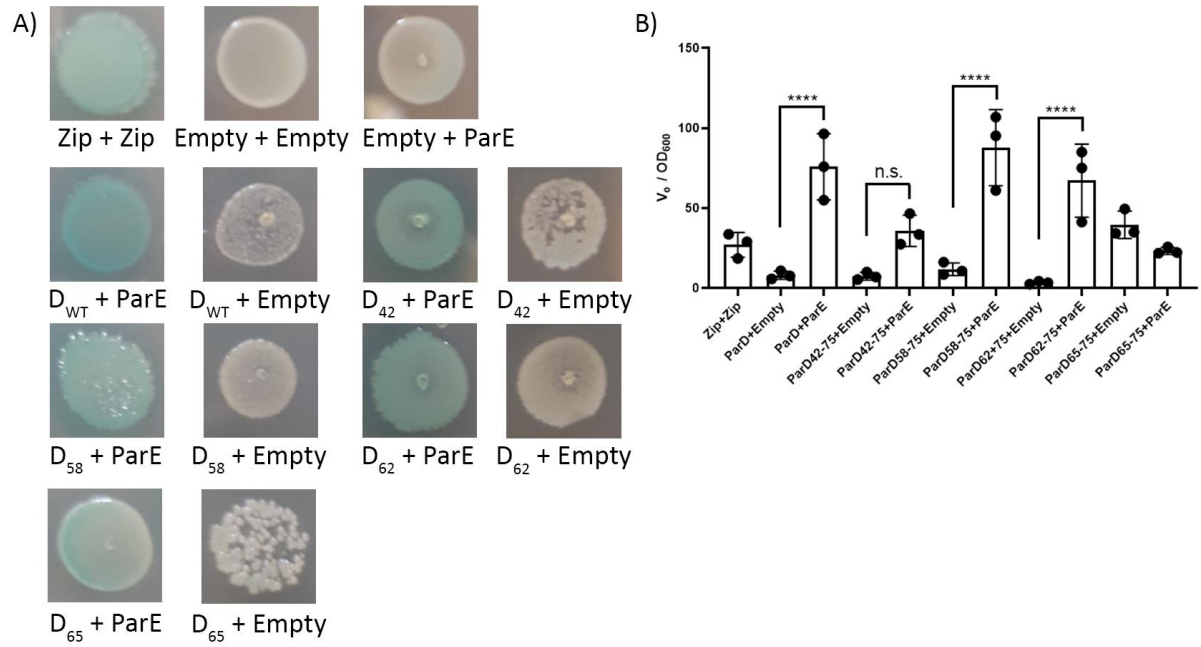

Figure 4.1. Bacterial two-hybrid and kinetic Miller assay of ParD1-derived peptides indicates minimal ParD1 binding unit. A) Co-transformed *E.coli* cells spotted on LB-agar supplemented with IPTG and X-gal. Blue colonies indicate positive interaction by reconstitution of adenylate cyclase; white colonies indicate negative interaction. **B)** Kinetic miller assays of the ParD1-ParE1 interactions (n = 3). Additional biological replicate in **Fig. S4.3** ****denotes p-value < 0.0001; $ParD_{42\text{-}75}$ p-value = 0.0593

Kinetic miller assays normalized to OD_{600} showed that ParD1-derived peptides corresponding to ParD1 residues 58-75 and 62-75 (different lengths of ParD1 alpha-helix 3) strong interact with wild-type ParE1 as indicated by significantly increased β-galactosidase activity (p-value < 0.0001) relative to the empty vector control. In the case of the ParD1-derived peptide corresponding to ParD1 residues 42-75 (full toxin-binding domain), no significant difference was observed (Fig. 4.1B). An mCherry-$ParD1_{42\text{-}75}$ fusion protein has previously shown that the $ParD1_{42\text{-}75}$ peptide does binds to "free" wild-type ParE1 *in vitro* by biolayer interferometry with affinities equivalent to wild-type ParD1.[8] Despite appearing blue when spotted on plates containing X-gal, the $ParD1_{65\text{-}75}$ peptide did not show any significant increase in β-galactosidase activity in the presence of wild-type ParE1 compared to the empty vector, indicating that interactions observed in the spotted *E. coli* colonies are likely transient and the signal is being amplified by β-galactosidase activity during the overnight incubation.

ParD1-derived peptides bind to ParE1 with similar affinities to wild-type ParD1

In order to further study the minimal antitoxin unit required to toxin binding, we utilized biolayer interferometry to study the binding affinities *in vitro*. Using site-directed mutagenesis, N-terminal truncations of ParD1 were generated from a full-length mCherry-ParD1 fusion protein. The same ParD1 peptides tested by BACTH ($ParD1_{58-75}$, $ParD1_{62-75}$) were generated and re-tested *in vitro*. Due to limited solubility, each peptide was purified as mCherry-fusions as previously described.[8] Kinetics of binding (association and dissociation) were measured for each ParD1 peptide and used to derive the equilibrium dissociation constant (K_d) for each mutant.

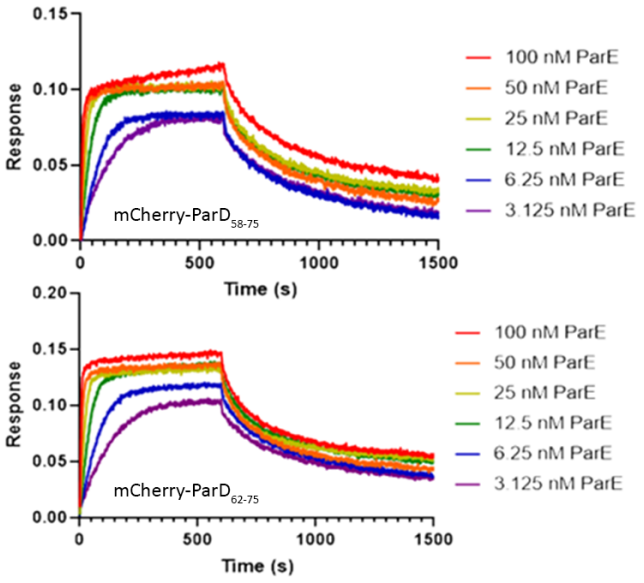

	K_{D1} (nM)	K_{D2} (nM)
mCh-PaParD1$_{WT}$	0.225 ± 0.006	n/a
mCh-PaParD1$_{42-75}$	0.828 ± 0.550	n/a
mCh-PaParD1$_{58-75}$	0.330 ± 0.113	14.19 ± 1.94
mCh-PaParD1$_{62-75}$	0.342 ± 0.059	7.95 ± 0.42

Figure 4.2. ParD1-derived peptides have binding affinities comparable to the full-length antitoxin. BLI traces of $ParD1_{58-75}$ and $ParD1_{62-75}$ with average K_D values (n=3). Additional traces with residual fitting shown in **fig. S4.1**. Fitting comparison is shown in **fig. S4.2**.

Equilibrium dissociation constants were determined for both mCherry-$ParD1_{58-75}$ and mCherry-$ParD1_{62-75}$, but no binding was detected for mCherry-$ParD1_{65-75}$, confirming the BACTH and kinetic miller assay results. As previously seen with some ParD1 mutants, both ParD1 peptides required fitting with a 2:1 heterogeneous ligand model to better fit the dissociation step, indicating two competing binding modes.[22] The mCherry-$ParD1_{58-75}$ peptide had a K_{d1} value of 330 ± 113 pM and K_{d2} value of 14.19 ± 1.94 nM, neither of which are significantly different from the previously determined K_d values for either mCherry-$ParD1_{wt}$ (225 ± 6 pM) or mCherry-$ParD1_{42-75}$ (828 ± 550 pM) (Fig. 4.2).[8] K_d values for mCherry-$ParD1_{62-75}$ (K_{d1} = 342 ± 59 pM and K_{d2} = 7.95 ± 0.42 nM) also showed no significant difference. No measurable binding was observed between mCherry and ParE1. Replicate BLI traces with residual fitting as well as the mCherry-ParE control are available in the supplemental data (fig. S4.1). A comparison of fitting results for ParD58-75 and ParD62-75 are also available (fig. S4.2).

Screening small-molecule protein-protein interaction inhibitors of the ParD1-ParE1 protein-protein interaction

In order to identify potential small-molecule protein-protein interaction inhibitors of the PaParDE1 protein-protein interaction, we utilized *in silico* docking to screen a peptidomemetic library to find potential high affinity inhibitors. With the ParD1 peptides characterized in this

work, and previously published binding data for the ParD1-ParE1 protein-protein interaction, we limited our search to compounds binding to ParE1 surface corresponding to the $ParD1_{58-75}$ binding site. In order to better rationalize our *in silico* binding data, we performed additional docking experiments using ParD1 peptides ($ParD1_{62-75}$ and $ParD1_{65-75}$) to generate a baseline score for known binders (Fig. 4.3).

After all compounds were docked, they were sorted into unique bins based on their structural identifier code, which corresponds to specific structural moieties. After sorting based on similar structure, the top scoring compound from each bin was then compared against each other to identify common structural features amongst the top scoring compounds. The binding scores of the top scoring compounds were normalized based on their intersurface area to determine their average binding energy over the whole protein-ligand interface and compared to the ParD1 peptide scores (Fig. 4.3). Commonalities between the top scoring compounds and the normal ParD1-ParE1 interaction include a tryptophan-like moiety which docked in a position closely aligned to the Trp72 binding pocket, as well as various structural moieties that closely docked into the Ile68 binding pocket.

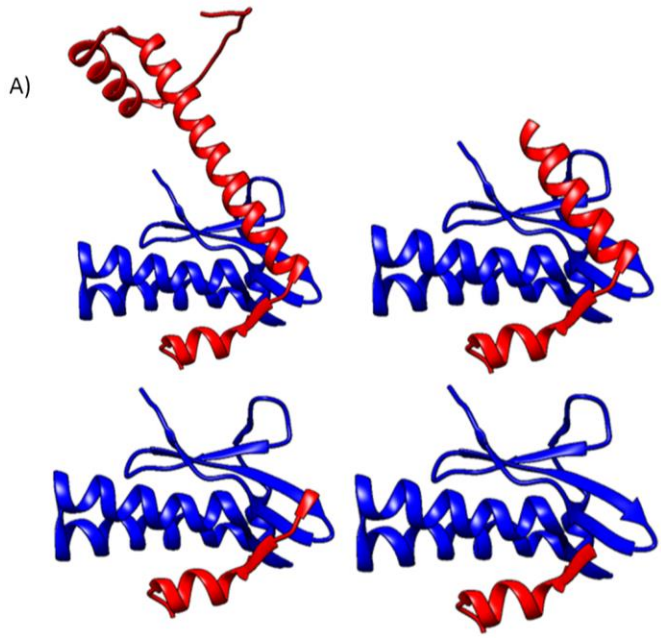

Compound	Affinity (kcal/mol)	Intersurf Area (Å^2)	Affinity / Intersurf Area
PaParD1_62-75	-17.5	957.8	-0.0183
PaParD1_65-75	-13.7	827.1	-0.0166
G907-0227	-9.4	563.9	-0.0167
G907-1207	-9.3	499.1	-0.0186
G868-1167	-9	598.9	-0.0150

Figure 4.3. Peptidomemetics compounds binding map to the ParD1 alpha-helix 3 - ParE1 interface, and target ParD1 side-chain binding sites. A) *Top Left*. Full-length ParD1-ParE1. *Top Right.* $ParD1_{42-75}$-ParE1. *Bottom Left*. $ParD_{58-75}$-ParE1. *Bottom Right.* $ParD_{62-75}$-ParE1. **B)** *In silico* docking of peptidomemetic compounds against ParE1.

Discussion

The concept of a minimal antitoxin binding unit required to sufficiently bind to and neutralize toxin could provide new insights into how to target toxin-antitoxin systems as a means to control bacterial cell growth. In combination with previously published mutational studies of the ParD1-ParE1 toxin-antitoxin protein-protein interaction, the ParD1 peptides characterized in this work have identified that the minimal ParD1 unit required for ParE1 binding corresponds to ParD1

residues 62-75, the fourteen C-terminal amino acids of ParD1. When additional truncations of either the C-terminus (Glu69stop) or the N-terminus ($ParD1_{65-75}$), binding is significantly reduced or completely abolished.[8] Biolayer interferometry of the $ParD1_{62-75}$ peptide binding to ParE1 indicates that this peptide, which corresponds to roughly 55% of the total ParD1-ParE1 interface area, has a binding affinity of low nM to high pM and is comparable to the affinity of the full-length toxin-binding domain.[8] These results support our hypothesis that the full-length binding is controlled by the disorder-to-order transition of the C-terminal alpha-helix of ParD1.[8]

The minimal antitoxin unit required for ParD1 binding provides us insight into how to prevent ParDE1 complex formation. Protein-protein interaction inhibitors that can compete for binding at the same interface as the $ParD1_{62-75}$ peptide binding interface, we can prevent complex formation. Disruption of complex formation would allow us to take advantage of the natural instability of antitoxin proteins to promote degradation of unbound antitoxin by cellular proteases, resulting in accumulation of "free" toxin protein.[8,22] Previous studies of the Pseudomonas aeruginosa ParDE1 protein-protein interactions also identified a "hot-spot" (Ile68) interaction that significantly impacts the binding affinity, which is located in the minimal unit identified in this work. The best scoring peptidomemetic compounds screened by *in silico* docking in this study were shown to be well aligned with multiple binding pockets within the $ParD1_{62-75}$ peptide binding interface. Structure-based rational design can be used to help further develop a protein-protein interaction inhibitor to better bind to these sites in order to competitively bind to ParE1 and prevent ParD1 binding.

Author Contributions

K.J.S. collected all data reported in this chapter; K.J.S. and C.R.B. participated in the project design, data analysis, manuscript drafting, and editing.

Funding

Funding Research reported in this chapter was supported by an award for project number HR17-099 from the Oklahoma Center for the Advancement of Science and Technology (to CRB). The content is solely the responsibility of the authors and does not necessarily represent the official views of the National Institutes of Health. Financial support was also provided from the Office of the Vice President for Research and the Office of the Provost, University of Oklahoma. Notes The authors declare no competing financial interest.

Acknowledgements

We appreciate the assistance of the OU Protein Production and Characterization core facility for assistance with protein purification and for access to the Octet RED96. The OU Protein Production and Characterization Core facility is supported by an Institutional Development Award (IDeA) from the National Institute of General Medical Sciences of the National Institutes of Health under grant number P20GM103640.

References

1. Kahan, R., Worm, D. J., de Castro, G. V., Ng, S., and Barnard, A. (2021) Modulators of protein-protein interactions as antimicrobial agents. RSC Chem Biol 2, 387-409

2. Lu, H., Zhou, Q., He, J., Jiang, Z., Peng, C., Tong, R., and Shi, J. (2020) Recent advances in the development of protein–protein interactions modulators: mechanisms and clinical trials. Signal Transduction and Targeted Therapy 5, 213
3. Jurėnas, D., Fraikin, N., Goormaghtigh, F., and Van Melderen, L. (2022) Biology and evolution of bacterial toxin–antitoxin systems. Nature Reviews Microbiology 20, 335-350
4. Fraikin, N., Goormaghtigh, F., and Van Melderen, L. (2020) Type II Toxin-Antitoxin Systems: Evolution and Revolutions. Journal of Bacteriology 202, e00763-00719
5. Page, R., and Peti, W. (2016) Toxin-antitoxin systems in bacterial growth arrest and persistence. Nature Chemical Biology 12, 208-214
6. Kang, S.-M., Kim, D.-H., Jin, C., and Lee, B.-J. (2018) A Systematic Overview of Type II and III Toxin-Antitoxin Systems with a Focus on Druggability. Toxins 10, 515
7. Harms, A., Brodersen, D. E., Mitarai, N., and Gerdes, K. (2018) Toxins, Targets, and Triggers: An Overview of Toxin-Antitoxin Biology. Molecular Cell 70, 768-784
8. Snead, K. J., Moore, L. L., and Bourne, C. R. (2022) ParD Antitoxin Hotspot Alters a Disorder-to-Order Transition upon Binding to Its Cognate ParE Toxin, Lessening Its Interaction Affinity and Increasing Its Protease Degradation Kinetics. Biochemistry 61, 34-45
9. Muthuramalingam, M., White, J. C., Murphy, T., Ames, J. R., and Bourne, C. R. (2019) The toxin from a ParDE toxin-antitoxin system found in Pseudomonas aeruginosa offers protection to cells challenged with anti-gyrase antibiotics. Molecular Microbiology 111, 441-454
10. Sterckx, Y. G. J., Jové, T., Shkumatov, A. V., Garcia-Pino, A., Geerts, L., De Kerpel, M., Lah, J., De Greve, H., Van Melderen, L., and Loris, R. (2016) A unique hetero-hexadecameric architecture displayed by the Escherichia coli O157 PaaA2–ParE2 antitoxin–toxin complex. Journal of Molecular Biology 428, 1589-1603
11. Yuan, J., Sterckx, Y., Mitchenall, L. A., Maxwell, A., Loris, R., and Waldor, M. K. (2010) Vibrio cholerae ParE2 poisons DNA gyrase via a mechanism distinct from other gyrase inhibitors. J Biol Chem 285, 40397-40408
12. Kang, S.-M., Moon, H., Han, S.-W., Kim, B. W., Kim, D.-H., Kim, B. M., and Lee, B.-J. (2021) Toxin-Activating Stapled Peptides Discovered by Structural Analysis Were Identified as New Therapeutic Candidates That Trigger Antibacterial Activity against Mycobacterium tuberculosis in the Mycobacterium smegmatis Model. Microorganisms 9, 568
13. Kang, S.-M., Jin, C., Kim, D.-H., Park, S. J., Han, S.-W., and Lee, B.-J. (2021) Structure-based design of peptides that trigger Streptococcus pneumoniae cell death. FEBS J 288, 1546-1564
14. Chen, R., Zhou, J., and Xie, W. (2021) Mechanistic Insight into the Peptide Binding Modes to Two M. tb MazF Toxins. Toxins 13
15. Farhadi, T., Hashemian, S. M., and Farhadi, Z. (2020) *In silico* Designing of Peptidomimetics Enhancing Endoribonucleolytic Activities of Acinetobacter MazF Toxin as the Novel Anti-bacterial Candidates. International Journal of Peptide Research and Therapeutics 26, 1061-1071
16. Sundar, S., Rajan, M. P., and Piramanayagam, S. (2019) *In silico* Derived Peptides for Inhibiting the Toxin–Antitoxin Systems of Mycobacterium tuberculosis: Basis for Developing Peptide-Based Therapeutics. International Journal of Peptide Research and Therapeutics 25, 1467-1475
17. Nigam, A., Kumar, S., and Engelberg-Kulka, H. (2018) Quorum Sensing Extracellular Death Peptides Enhance the Endoribonucleolytic Activities of Mycobacterium tuberculosis MazF Toxins. mBio 9, e00685-00618

18. Ahn, D.-H., Lee, K.-Y., Lee, S. J., Park, S. J., Yoon, H.-J., Kim, S.-J., and Lee, B.-J. (2017) Structural analyses of the MazEF4 toxin-antitoxin pair in Mycobacterium tuberculosis provide evidence for a unique extracellular death factor. Journal of Biological Chemistry 292, 18832-18847
19. Kim, D.-H., Kang, S.-M., Park, S. J., Jin, C., Yoon, H.-J., and Lee, B.-J. (2018) Functional insights into the Streptococcus pneumoniae HicBA toxin-antitoxin system based on a structural study. Nucleic Acids Res 46, 6371-6386
20. Gao, X., Mu, Z., Qin, B., Sun, Y., and Cui, S. (2017) Structure-Based Prototype Peptides Targeting the Pseudomonas aeruginosa Type VI Secretion System Effector as a Novel Antibacterial Strategy. Front Cell Infect Microbiol 7, 411-411
21. Schaefer, J., Jovanovic, G., Kotta-Loizou, I., and Buck, M. (2016) Single-step method for β-galactosidase assays in Escherichia coli using a 96-well microplate reader. Anal Biochem 503, 56-57
22. Snead, K. J., and Bourne, C. R. (2021) Intrinsic Degradation of the Type-II Antitoxin ParD from Pseudomonas aeruginosa. bioRxiv, 2021.2003.2029.437564
23. Trott, O., and Olson, A. J. (2010) AutoDock Vina: improving the speed and accuracy of docking with a new scoring function, efficient optimization, and multithreading. J Comput Chem 31, 455-461
24. Pettersen, E. F., Goddard, T. D., Huang, C. C., Couch, G. S., Greenblatt, D. M., Meng, E. C., and Ferrin, T. E. (2004) UCSF Chimera--a visualization system for exploratory research and analysis. J Comput Chem 25, 1605-1612

Chapter V

Research Impact and Future Directions

The research presented in chapters II-IV contributing to this dissertation work has provided unique insights into the field of toxin-antitoxin (TA) system research. Chapter II provided new details into the basis of how the strong (typically nano to picomolar affinity) protein-protein interactions are formed as well as provided evidence that key residues can act as "hot-spots" that contribute significantly to the interactions.[1] We also identified how weakening the protein-protein interaction of toxin-antitoxin systems can directly impact antitoxin availability for proteolysis by cellular proteases such as the AAA+ protease Lon, as well as Chapter III that identified a previously uncharacterized example of intrinsic degradation of type-II antitoxins.[1,2] We also determined that complex formation of the PaParDE1 system is predicated on the initial seeding of the seven most C-terminal amino acids of ParD1, as shown by binding studies utilizing both N- and C-terminal truncations of ParD1.[1]

The utilization of the Pseudomonas aeruginosa ParDE1 (PaParDE1) toxin-antitoxin system, which contains an attenuated toxin ParE1,[3] in chapter II allowed us to utilize techniques to study the protein-protein interactions that are typically infeasible with more potent toxin-antitoxin systems. The attenuated nature of ParE1 allowed us to easily overexpress and purify large quantities (several milligrams per liter) of toxin protein without the normal difficulties associated with purifying highly potent toxins. Typically, toxin proteins must be co-expressed and co-purified in the presence of their cognate antitoxin protein, followed by difficult and tedious unfolding and re-folding of the toxin protein.[4] While this process has be shown to work with some toxin-antitoxin systems, we have experienced that these methods require high amounts of optimization of each step to produce soluble and active protein, and usually with very low yields, making *in vitro* experiments such as the "hot-spot" analysis used in chapter II unfeasible.

The *in vitro* "hot-spot" analysis of the protein-protein interactions of the PaParDE1 system from chapter II is the first study to look at the individual contributions of each residue of the antitoxin involved in forming and maintaining the high affinity protein-protein interactions of type-II TA systems. While it isn't feasible to perform the same *in vitro* "hot-spot" analysis on every toxin-antitoxin system, it provides us key insights that we can be applied to type-II TA systems. In combination with advancements in protein structure and protein-protein complex structure prediction by artificial intelligence assisted programs like AlphaFold, which can provide highly accurate models in a high-throughput manner, we can build databases to better predict which residues may act as "hot-spots" in other TA systems.[5] Once we have identified these "hot-spot" residues, we can utilize more high-throughput assays such as *in vivo* toxicity assays or bacterial two-hybrid assays to characterize these interactions. The prediction of "hot-spots" will allow us to rationally design antitoxin mutants to better validate these predictions in a high-throughput manner.

In addition to the "hot-spot" analysis utilized in chapter II to study the protein-protein interactions of type-II TA systems, we also utilized both N- and C-terminal antitoxin truncations in chapters II and IV to map the minimal antitoxin unit required to form a stable protein-protein interaction in TA systems. In the case of the PaParDE1 system, we determined the minimal unit

required for binding is the C-terminal residues corresponding to amino acids 62-75 of the antitoxin ParD1 (manuscript in preparation). In the full-length antitoxin, this region is unstructured in the absence of ParE1 as determined by analysis of secondary structure utilizing FTIR in chapter II. This region undergoes a disorder-to-order transition to form an alpha-helix upon binding to ParE1, which was confirmed by our x-ray crystal structure of the ParDE1 complex.[1] In the case of the PaParDE1 system, when the C-terminal alpha-helix of ParD1 is truncated, or when specific positions are mutated (Ile68Ala), the disorder-to-order transition is altered, or the protein-protein binding is completely abolished (Glu69Stop). With this knowledge in hand, we can utilize computational methods such as *in silico* docking, as in chapter IV, to predict protein-protein interaction inhibitors (PPIi) that can disrupt the formation of toxin-antitoxin complexes while maintaining protein activity.

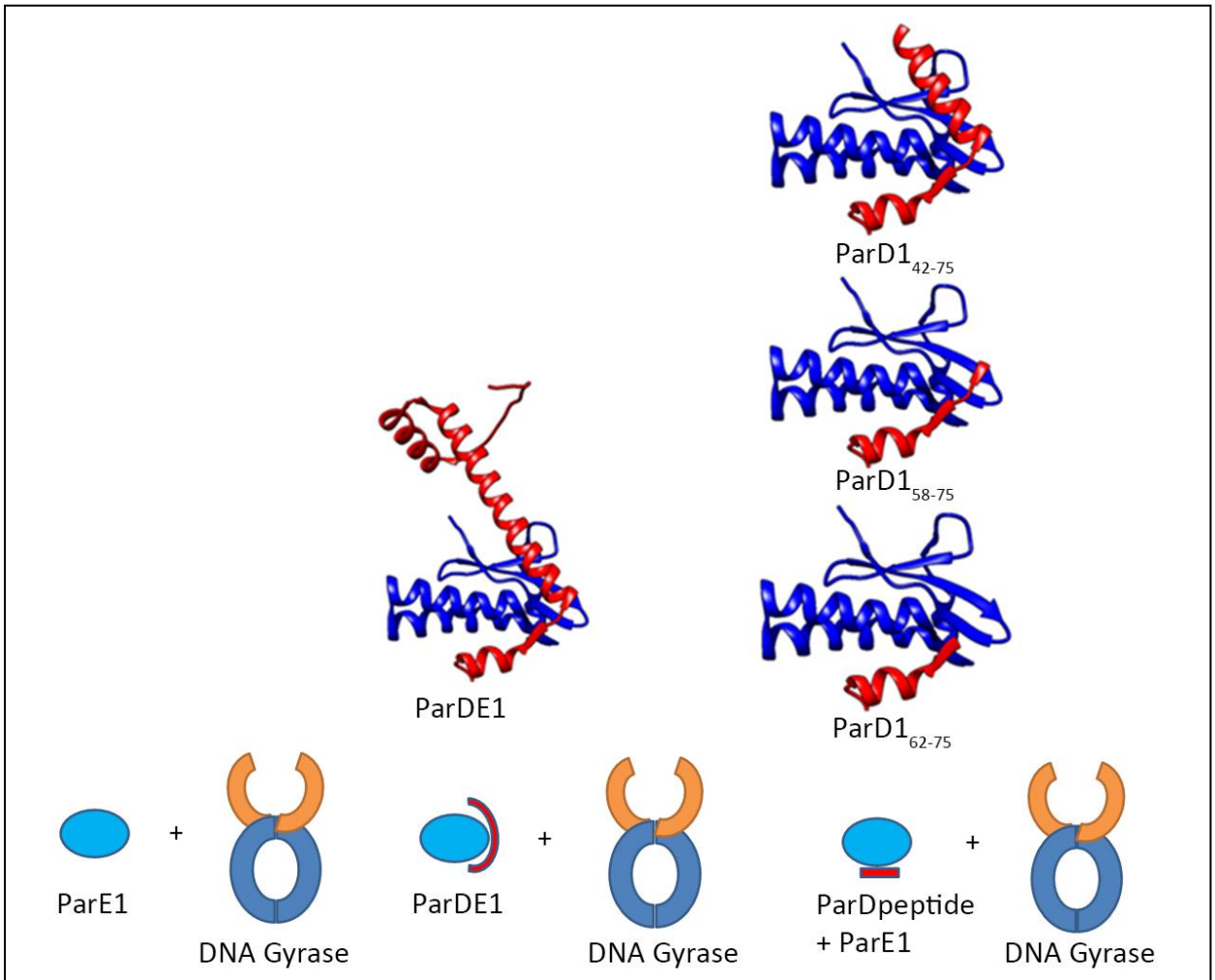

Figure 5.1. Schematic for probing ParE-mediated DNA Gyrase inhibition. DNA gyrase inhibition assays carried out in the presence of PaParE1 (left), PaParDE1 complex (center) or PaParE-ParD1$_{peptide}$ complexes (right); can be utilized to determine the ParE1 surface required to bind to and inhibit DNA gyrase.

One of the most important pieces of knowledge needed going forward in the field of toxin-antitoxin research, specifically for ParDE systems, is understanding the mechanism of action of ParE-mediated DNA gyrase inhibition. With the knowledge of the minimal ParD1 unit required for binding as determined in chapters II and IV, we can assay ParE toxicity in the presence of various lengths of antitoxin to determine their role in toxin-neutralization. In the case of the PaParDE1 system, we can test different lengths of the ParD1 antitoxin in their ability to neutralize ParE1 toxicity (Fig. 5.1). In testing a combination of ParE1 bound to different ParD1 peptides corresponding to the full-length antitoxin, the full toxin-binding domain, or the C-terminal alpha-helix of the toxin-binding domain, we can determine which toxin surface is required to inhibit DNA gyrase. These studies are on-going, and their completion is expected to be combined with my data in Chapter IV for publication. In addition, determination of a ParE-DNA gyrase protein complex would be a major boon to the field, allowing for additional insight into the mechanism of inhibition. In addition, a ParE-DNA gyrase structure would allow us to better design protein-protein interaction inhibitors that could prevent antitoxin binding, without impacting the ParE-DNA gyrase interactions.

Another major development of this research is the first reported instance that shows a direct link between toxin-antitoxin binding affinity and antitoxin stability. Previous research on the RK2 ParDE1 system has shown that the presence of a cognate ParE protected a ParD antitoxin from degradation by cellular proteases.[6] In chapter II, we showed that when the protein-protein interaction affinity of a type-II TA system is reduced, such as the case of the Ile68Ala mutation of PaParD1, the resulting increase in unbound antitoxin is directly correlated to antitoxin degradation by cellular proteases.[1] In the case of the wild-type PaParDE1 complex, the picomolar binding affinity resulted in little degradation of antitoxin. The Ile68Ala mutation of PaParD1, which impacts the disorder-to-order transition of alpha helix 3 upon PaParE1 binding results in different binding affinities. The difference in affinities is primarily due to a significantly increased dissociation constant of the Ile68Ala mutation. This increase in dissociation rate of the Ile68Ala mutant resulted in complete degradation in the same timeframe compared to wild-type PaParDE1.[1] These results provide insight that weakening or completely blocking the normal protein-protein interactions of type-II TA systems could be a viable method to accumulate excess “free” toxin by increasing the rate of antitoxin degradation.

While we have shown direct evidence that weakening the protein-protein interactions can increase antitoxin degradation, it currently remains to be seen if degradation of antitoxin is sufficient in generating active toxin protein. Experiments are currently underway utilizing an inducible degradation system based on an SspB-mediated degron to artificially degrade antitoxin from a toxin-antitoxin complex.[7] Using this system, we can introduce a co-expression plasmid containing PaParD1 C-terminally tagged with the DAS+4 degron and PaParE1 and transform it into an SspB knockout strain of E. coli co-transformed with an inducible plasmid-encoded SspB. Using this system, we can probe the feasibility of AAA+ proteases ability to directly degrade antitoxin from the toxin-antitoxin complex. After the toxin-antitoxin complex has been sufficiently induced, we would induce SspB production to begin degrading antitoxin. Results of these experiments will provide insight into how the systems might be activated in response to stress. It is currently unknown if activation of toxin-antitoxin systems result from de-repression of the TA operon combined with up-regulation of toxin translation and up-regulation of degradation of unbound antitoxin by cellular proteases, or if activation of TA systems is a result

of degradation of antitoxin from pre-formed complex resulting in the accumulation of "free" toxin protein.

The intrinsic degradation of antitoxin reported in chapter III is, to our knowledge, the second reported instance of self-proteolysis of antitoxin protein in the absence of cognate toxin protein, although the inherent instability of purified antitoxins is common knowledge within the field. Utilizing a top-down mass spectrometry approach, we were able to map an instance of self-cleavage of antitoxin protein. This is the second identified case of a ParD-type antitoxin that undergoes self-cleavage in the absence of proteases.[2,8] While the original observation of the RK2 ParD degradation was investigated using MALDI-TOF mass spectrometry, the authors did not determine whether the degradation was caused by trace amounts of contaminating proteases, or whether the degradation was caused by autoproteolysis by the antitoxin.[8] In our research, we utilized direct-infusion mass spectrometry to analyze intact proteins present in the sample. In freshly purified samples, we detected two species corresponding to monomeric and dimeric ParD antitoxin. ParD samples were incubated at room temperature for two weeks prior to analysis by mass spectrometry to capture the "degraded" state. After analysis by direct-infusion mass spectrometry, we identified a series of peptides with masses corresponding to the N-terminus of ParD1 with a series of cleavages in the range of residues 42-47. The most abundant PaParD1 peptide corresponded to cleavage at the C-terminal end of Gln46.[2]

Despite a homologous sequence in the RK2 ParD in the same location, the reported degradation of RK2 ParD did not appear to occur in the same region[8], but mass predictions indicate that the peptides may correspond to different glutamine rich regions of the RK2 ParD sequence.[7] In both cases, the peptides correspond to cleavages that would map to alpha-helix two of the ParD antitoxin, which could provide insight into ParD stability. Additional research would be required to determine if this degradation is unique to these two ParD antitoxins, or whether it is a common feature of ParD antitoxins.

Utilizing multi-sequence alignment and blast searches, we can generate a database of ParD antitoxin sequences, and determine if these glutamine-rich regions are common amongst these sequences. ParD antitoxins containing similar sequences can be tested to determine if they undergo similar intrinsic degradation. Recent research into autoproteolysis of proteins have identified intrinsic degradation occurring at the C-terminal end of glutamic acid and glutamine residues under similar conditions.[9] Additional research is still required to determine what if any role this intrinsic degradation of antitoxin may play *in vivo*, including whether the observed degradation contributes to the relatively short half-life of antitoxin proteins. It also remains to be seen whether this degradation occurs when the antitoxin is bound to its cognate protein.

Overall, the research presented in this dissertation has greatly increased our overall understanding of how the protein-protein interactions of type-II toxin antitoxins are formed, as well as provided new insights into how we can target these interactions to develop new methods to control bacterial cell growth using toxin-antitoxin systems. Moving forward, the ultimate goal is to utilize the newly synthesized knowledge provided by this research to develop a mechanism of ParE-mediated DNA gyrase inhibition. Once we have determined how ParE inhibits DNA gyrase, we can create a database of ParE structures through a combination of x-ray crystallography, cryo-EM, and structural prediction using AlphaFold to help predict protein-

protein interaction inhibitors using *in silico* docking to prevent the formation of toxin-antitoxin protein-protein interactions. These inhibitors would facilitate the accumulation of "free" toxin protein due to increased degradation of unbound antitoxin protein, allowing us to develop new antibacterial agents which can be tuned to target individual ParDE systems, allowing us to potentially develop new narrow-spectrum antibiotics.

References

1. Snead, K. J., Moore, L. L., and Bourne, C. R. (2022) ParD Antitoxin Hotspot Alters a Disorder-to-Order Transition upon Binding to Its Cognate ParE Toxin, Lessening Its Interaction Affinity and Increasing Its Protease Degradation Kinetics. Biochemistry 61, 34-45
2. Snead, K. J., and Bourne, C. R. (2021) Intrinsic Degradation of the Type-II Antitoxin ParD from Pseudomonas aeruginosa. bioRxiv, 2021.2003.2029.437564
3. Muthuramalingam, M., White, J. C., Murphy, T., Ames, J. R., and Bourne, C. R. (2019) The toxin from a ParDE toxin-antitoxin system found in Pseudomonas aeruginosa offers protection to cells challenged with anti-gyrase antibiotics. Molecular Microbiology 111, 441-454
4. Sterckx, Y. G. J., De Gieter, S., Zorzini, V., Hadži, S., Haesaerts, S., Loris, R., and Garcia-Pino, A. (2015) An efficient method for the purification of proteins from four distinct toxin–antitoxin modules. *Protein Expression and Purification* **108**, 30-40
5. Jumper, J., Evans, R., Pritzel, A., Green, T., Figurnov, M., Ronneberger, O., Tunyasuvunakool, K., Bates, R., Žídek, A., Potapenko, A., Bridgland, A., Meyer, C., Kohl, S. A. A., Ballard, A. J., Cowie, A., Romera-Paredes, B., Nikolov, S., Jain, R., Adler, J., Back, T., Petersen, S., Reiman, D., Clancy, E., Zielinski, M., Steinegger, M., Pacholska, M., Berghammer, T., Bodenstein, S., Silver, D., Vinyals, O., Senior, A. W., Kavukcuoglu, K., Kohli, P., and Hassabis, D. (2021) Highly accurate protein structure prediction with AlphaFold. Nature 596, 583-589
6. Dubiel, A., Wegrzyn, K., Kupinski, A. P., and Konieczny, I. (2018) ClpAP protease is a universal factor that activates the parDE toxin-antitoxin system from a broad host range RK2 plasmid. Scientific reports 8, 15287
7. McGinness, K. E., Baker, T. A., and Sauer, R. T. (2006) Engineering Controllable Protein Degradation. Molecular Cell 22, 701-707
8. Oberer, M., Lindner, H., Glatter, O., Kratky, C., and Keller, W. (1999) Thermodynamic Properties and DNA Binding of the ParD Protein from the Broad Host-Range Plasmid RK2/RP4 Killing System. 380, 1413-1420
9. Friedrich, M. G., Wang, Z., Schey, K. L., and Truscott, R. J. W. (2021) Spontaneous Cleavage at Glu and Gln Residues in Long-Lived Proteins. ACS Chemical Biology 16, 2244-2254

Appendix A:

Chapter II Supporting Information

ParD Antitoxin Hotspot Alters a Disorder-to-Order Transition upon Binding to its Cognate ParE Toxin, Lessening Its Interaction Affinity and Increasing Its Protease Degradation Kinetics

Kevin J. Snead , Landon L. Moore, Christina R. Bourne

Contents

Table S2.1. Primer sequences used for mutagenesis of PaParD.

W45 to Ala*	F: 5'-g gaa agg cag cag GCG cag gtc gct gcc-3'
	R: 5'-ggc agc gac ctg CGC ctg ctg cct ttc c-3'
V47 to Ala*	F: 5'-cag cag tgg cag GCC gct gcc atc gat-3'
	R: 5'-atc gat ggc agc GGC ctg cca ctg ctg-3'
I50 to Ala*	F: 5'-gg cag gtc gct gcc GCC gat gaa ggc ttg g-3'
	R: 5'-c caa gcc ttc atc GGC ggc agc gac ctg cc-3'
L54 to Ala*	F: 5'-gcc atc gat gaa ggc GCG gcc gat gcc aat gc-3'
	R: 5'-gc att ggc atc ggc CGC gcc ttc atc gat ggc-3'
D56 to Ala†	F: 5'-aa ggc ttg gcA GCG gcc aat gcc g-3'
	R: 5'-c atc gat ggc agc gac ct-3'
L62 to Ala*	F: 5'-cc aat gcc ggt cgc GCG ctg gaa cac atc g-3'
	R: 5'-c gat gtg ttc cag CGC gcg acc ggc att gg-3'
L63 to Ala*	F: 5'-c aat gcc ggt cgc ctg GCG gaa cac atc gag atc-3'
	R: 5'-gat ctc gat gtg ttc CGC cag gcg acc ggc att g-3'
E64 to Ala†	F: 5'-t cgc ctg ctg GCG cac atc gag atc gag-3'
	R: 5'-cc ggc att ggc atc ggc c-3'
H65 to Ala†	F: 5'-c ctg ctg gaa GCG atc gag atc gag-3'
	R: 5'-cg acc ggc att ggc atc g-3'
I66 to Ala*	F: 5'-cgc ctg ctg gaa cac GCC gag atc gag aag cg-3'
	R: 5'-cg ctt ctc gat ctc GGC gtg ttc cag cag gcg-3'
I68 to Ala*	F: 5'-ctg gaa cac atc gag gcc GAG aag cgc tgg gg-3'
	R: 5'-cc cca gcg ctt CTC ggc ctc gat gtg ttc cag-3'
E69 to Ala†	F: 5'-c atc gag atc GCG aag cgc tgg g-3'
	R: 5'-tg ttc cag cag gcg acc g-3'
R71 to Ala†	F: 5'-g atc gag aag GCG tgg ggg ctg caa tg-3'
	R: 5'-tc gat gtg ttc cag cag g-3'
W72 to Ala*	F: 5'-gag atc gag aag cgc GCG ggg ctg caa tga gg-3'
	R: 5'-cc tca ttg cag ccc CGC gcg ctt ctc gat ctc-3'
L74 to Ala†	F: 5'-ag cgc tgg ggA GCT caa tga gga tc-3'
	R: 5'-t ctc gat ctc gat gtg ttc-3'
N58 to Stop*	F: 5'-gaa ggc ttg gcc gat gcc aat TAG ggt cgc ctg ct-3'
	R: 5'-ag cag gcg acc CTA att ggc atc ggc caa gcc ttc-3'
L63 to Stop†	F: 5'-c gct cgc ctg TAA gaa cac atc gag atc-3'
	R: 5'-gc att ggc atc ggc caa g-3'
E69 to Stop†	F: 5'-c atc gag atc TAA aag cgc tgg ggg-3'
	R: 5'-gc att ggc atc ggc caa g-3'

*denotes primers for QuikChange (Stratagene); †denotes primers for Q5 (NEB) mutagenesis

Table S2.2. Data collection and refinement statistics

	PaParDE1 (6XRW)
Resolution range (Å)	27.86 - 1.77 (1.84 - 1.77)
Space group	C 2 2 21
Unit cell (Å)	98.4, 121.3, 58.6 90°, 90°, 90°
Total reflections	168452 (7423)
Unique reflections	32866 (3106)
Multiplicity	5.1 (2.4)
Completeness (%)	99.4 (95.5)
Mean I/sigma (I)	21.7 (3.6)
Wilson B-factor (Å2)	19.1
R-merge	0.049 (0.274)
R-meas	0.054 (0.347)
R-pim	0.022 (0.210)
CC1/2	0.999 (0.905)
Reflections used in refinement	33497 (3178)
Reflections used for R-free	1999 (190)
R-work	0.1776 (0.2626)
R-free	0.2195 (0.3350)
Number of non-hydrogen atoms	3224
macromolecules	2744
ligands	61
solvent	419
Protein residues	342
RMSD (bonds, Å)	0.008
RMSD (angles, °)	0.97
Ramachandran favored (%)	99.40
Ramachandran allowed (%)	0.60
Ramachandran outliers (%)	0.00
Rotamer outliers (%)	0.35
Clashscore	9.17
Average B-factor (Å2)	24.14
macromolecules	22.26
ligands	27.38
solvent	35.97

Statistics for the highest-resolution shell are shown in parentheses.

Table S2.3. Global fitting results for Biolayer Interferometry assays

	K_D (M)	*p* value	k_{on} (1/Ms)	*p* value	koff (1/s)	*p* value
Wild-type	1.52 ± 0.12 E-10	n/a	7.50 ± 0.30 E+05	n/a	1.20 ± 1.00 E-05	n/a
W45A	< 1.0 E-12	> 0.99	3.56 ± 2.35E+04	0.99	< 1.0 E-07	> 0.99
V47A	< 1.0 E-12	> 0.99	1.88 ± 0.87 E+05	0.99	< 1.0 E-07	> 0.99
I50A	4.90 ± 1.39 E-09	> 0.99	1.82 ± 1.28E+04	0.99	5.24 ± 1.0 E-05	> 0.99
D56A	2.41 ± 0.50 E-09	> 0.99	1.33 ± 0.40 E+05	0.99	3.16 ± 1.16 E-04	> 0.99
L62A	3.64 ± 2.18 E-09	> 0.99	1.80 ± 0.37 E+05	0.99	1.19 ± 0.40 E-03	0.99
L63A	5.33 ± 4.00 E-08	0.99	1.41 ± 1.47E+04	0.99	3.56 ± 1.34 E-04	> 0.99
E64A	7.05 ± 1.28 E-10	> 0.99	9.50 ± 0.66 E+04	0.99	6.73 ± 1.52E-05	> 0.99
H65A	1.90 ± 0.63 E-9	> 0.99	2.63 ± 0.63 E+05	0.79	4.73 ± 0.22 E-04	> 0.99
I66A	< 1.0 E-12	> 0.99	1.17 ± 0.89 E+05	0.99	< 1.0 E-07	> 0.99
I68A (1)	6.27 ± 4.69 E-07	< 0.0001	8.47 ± 3.40 E+04	0.99	4.25 ± 1.61E-02	< 0.0001
I68A (2)	2.55 ± 2.19 E-08	0.99	4.67 ± 2.73 E+05	0.06	7.99 ± 6.55E-03	0.98
E69A	7.89 ± 0.95 E-11	> 0.99	1.20 ± 0.07 E+05	0.99	9.55 ± 1.59E-05	> 0.99
R71A	4.31 ± 0.42 E-10	> 0.99	3.86 ± 0.16 E+05	0.22	1.53 ± 0.354 E-04	> 0.99
W72A	<1.0 E-12	> 0.99	2.95 ± 0.26 E+05	0.62	< 1.0 E-07	n.s.
L74A	1.89 ± 0.38 E-09	> 0.99	1.78 ± 0.38 E+05	0.99	3.27 ± 0.06 E-04	> 0.99
mCh-WT	3.10 ± 2.32 E-10	> 0.99	2.20 ± 1.51 E+05	0.99	3.25 ± 1.86E-04	> 0.99
mCh-WT_{42-75}	8.28 ± 5.49 E-10	> 0.99	6.14 ± 5.97 E+05	0.99	1.37 ± 2.34E-02	0.55
mCh-$I68A_{42-75}$ (1)	3.00 ± 1.12 E-8	0.99	1.74E ± 0.30 E+06	< 0.0001	5.43 ± 3.03E-02	< 0.0001
mCh-$I68A_{42-75}$ (2)	2.86 ± 0.18 E-09	> 0.99	1.09 ± 0.63 E+05	0.99	2.36 ± 0.93 E-04	> 0.99

p-values were calculated using one-way ANOVA compared to previously published wild-type PaParDE1 interaction kinetics (Muthuramalingam, et al (2018) Molecular microbiology 111, 441-454).

Table S2.4. Secondary Structure Analysis of PaParDE1 Complex by FTIR (n=3)

	# Amino Acids in Secondary Structure	
	α helix	**β sheet**
WT PaParD1 (dimer)	67	55
I68A PaParD1 (dimer)	70	55
PaParE1 (monomer)	31	44

	# Amino Acids in Secondary Structure		Remove contribution of PaParE1 from complex = contribution of antitoxin		Difference in complexed antitoxin dimer as compared to free antitoxin dimer	
	α helix	**β sheet**	**α helix**	**β sheet**	**α helix**	**β sheet**
WT PaParDE1 complex (D_2:E_2)	141	141	79	53	12	-2
I68A PaParDE1 complex (D_2:E_1)	130	99	99	55	29	0

Table S2.5. ParD-ParE Interface Analysis

PDB ID	Interface	Interface Area (Å^2)	Surface Area (Å^2) (ParD, copy 1)	% Buried (ParD, copy 1)	% Hydrophobic (ParD, copy 1)	Surface Area (Å^2) (ParD, copy 2)	% Buried (ParD, copy 2)	% Hydrophobic (ParD, copy 2)
6XRW	ParD-ParD	1700.4	7543.0	22.5	48.6	7543.0	22.5	48.6
3KXE	ParD-ParD	1343.5	7026.0	19.5	51.7	6893.0	19.1	51.7
5CEG	ParD-ParD	1685.9	8458.0	19.9	47.4	8458.0	19.9	47.4
6X0A	ParD-ParD	1391.6	8596.0	16.3	50.0	8523.0	16.2	44.1

PDB ID	Interface	Interface Area (Å^2)	Surface Area (Å^2) (ParD)	% Buried (ParD)	% Hydrophobic (ParD)	Surface Area (Å^2) (ParE)	% Buried (ParE)	% Hydrophobic (ParE)
6XRW	ParD-ParE	1247.0	7543.0	16.5	46.2	5892.0	21.2	37.8
3KXE	ParD-ParE	1479.6	6893.0	21.5	51.9	6645.0	22.3	40.0
5CEG	ParD-ParE	1607.2	8458.0	19.0	46.7	6585.0	24.4	48.8
6X0A	ParD-ParE	1552.0	8523.0	18.2	57.6	5959.0	26.0	58.7
5CZE	Paa-ParE	1660.0	6101.0	27.2	40.6	5663.0	29.3	50.0

*Surface area values were calculated using the PDBePISA webserver from EMBL.
Note, the structure 5CZE lacks the ParD-ParD interaction interface.

WT ParD1 (Ni-NTA Pin) + WT ParE1

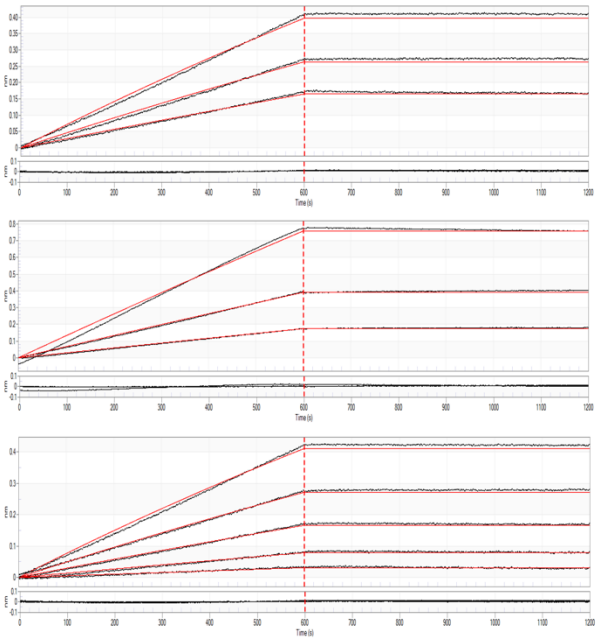

	Conc. (nM)	KD (M)	kon(1/Ms)	kdis(1/s)	Full R^2
Local Fit	10	<1.0E-12	8.64E+04	<1.0E-07	0.9831
	5	<1.0E-12	1.22E+05	<1.0E-07	0.991
	2.5	<1.0E-12	1.23E+05	<1.0E-07	0.993
Global Fit		<1.0E-12	1.49E+04	<1.0E-07	0.9977

	Conc. (nM)	KD (M)	kon(1/Ms)	kdis(1/s)	Full R^2
Local Fit	5	<1.0E-12	7.92E+04	<1.0E-07	0.9938
	2.5	<1.0E-12	3.29E+05	<1.0E-07	0.9742
	1.25	<1.0E-12	3.49E+05	<1.0E-07	0.984
Global Fit		<1.0E-12	8.24E+04	<1.0E-07	0.9956

	Conc. (nM)	KD (M)	kon(1/Ms)	kdis(1/s)	Full R^2
Local Fit	5	<1.0E-12	8.06E+04	<1.0E-07	0.9949
	3.5	<1.0E-12	1.69E+05	<1.0E-07	0.9944
	2.5	<1.0E-12	3.52E+05	<1.0E-07	0.984
	1.25	<1.0E-12	7.71E+05	<1.0E-07	0.9609
	0.625	2.14E-09	6.49E+04	1.39E-04	0.96
Global Fit		<1.0E-12	8.67E+04	<1.0E-07	0.998

Figure S2.1. Replicates of Biolayer Interferometry assays with corresponding residual error of fits and calculated values. (Additional images for each mutant on the following pages).

W45A ParD1 (Ni-NTA Pin) + WT ParE1

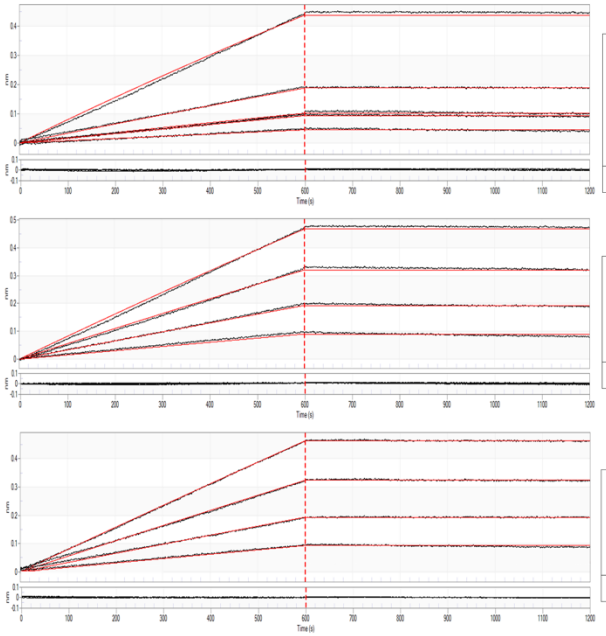

	Conc. (nM)	KD (M)	kon(1/Ms)	kdis(1/s)	Full R^2
Local Fit	5	<1.0E-12	1.12E+05	<1.0E-07	0.9928
	3.5	<1.0E-12	2.35E+05	<1.0E-07	0.973
	2.5	<1.0E-12	5.05E+05	<1.0E-07	0.9862
	1.25	3.27E-10	2.44E+05	7.98E-05	0.996
	0.625	1.82E-09	1.14E+05	2.08E-04	0.9796
Global Fit		<1.0E-12	6.10E+04	<1.0E-07	0.9984

	Conc. (nM)	KD (M)	kon(1/Ms)	kdis(1/s)	Full R^2
Local Fit	5	<1.0E-12	2.32E+05	<1.0E-07	0.9773
	3.5	<1.0E-12	2.50E+05	<1.0E-07	0.9835
	2.5	2.53E-09	2.39E+04	6.03E-05	0.9991
	1.25	2.25E-09	1.35E+05	3.03E-04	0.9972
Global Fit		<1.0E-12	3.13E+04	<1.0E-07	0.9983

	Conc. (nM)	KD (M)	kon(1/Ms)	kdis(1/s)	Full R^2
Local Fit	5	7.59E-10	3.93E+03	2.98E-06	0.9998
	3.5	<1.0E-12	1.68E+05	<1.0E-07	0.9944
	2.5	<1.0E-12	4.99E+05	<1.0E-07	0.9833
	1.25	1.28E-09	1.17E+05	1.49E-04	0.9959
Global Fit		1.03E-10	1.46E+04	1.51E-06	0.9995

V47A ParD1 (Ni-NTA Pin) + WT ParE1

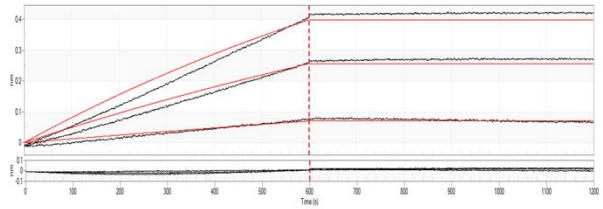

	Conc. (nM)	KD (M)	kon(1/Ms)	kdis(1/s)	Full R^2
Local Fit	5	<1.0E-12	1.63E+05	<1.0E-07	0.9734
	3.5	<1.0E-12	1.76E+05	<1.0E-07	0.9722
	1.25	<1.0E-12	1.88E+05	<1.0E-07	0.9433
Global Fit		<1.0E-12	1.68E+05	<1.0E-07	0.9864

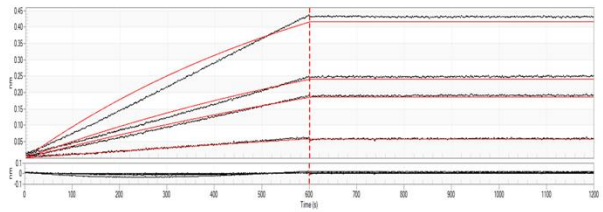

	Conc. (nM)	KD (M)	kon(1/Ms)	kdis(1/s)	Full R^2
Local Fit	5	<1.0E-12	1.95E+05	<1.0E-07	0.9901
	3.5	<1.0E-12	2.81E+05	<1.0E-07	0.9877
	2.5	<1.0E-12	2.35E+05	<1.0E-07	0.9943
	1.25	<1.0E-12	1.05E+06	<1.0E-07	0.9785
Global Fit		<1.0E-12	2.85E+05	<1.0E-07	0.9924

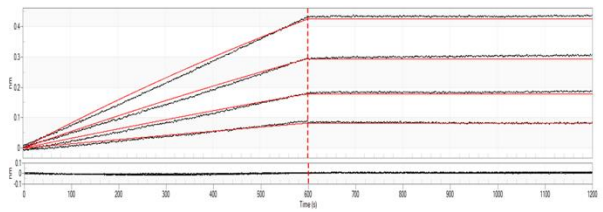

	Conc. (nM)	KD (M)	kon(1/Ms)	kdis(1/s)	Full R^2
Local Fit	5	<1.0E-12	3.08E+04	<1.0E-07	0.999
	3.5	<1.0E-12	1.74E+05	<1.0E-07	0.9888
	2.5	<1.0E-12	3.21E+05	<1.0E-07	0.9719
	1.25	<1.0E-12	7.85E+05	<1.0E-07	0.9619
Global Fit		<1.0E-12	1.15E+05	<1.0E-07	0.9965

I50A ParD1 (Ni-NTA Pin) + WT ParE1

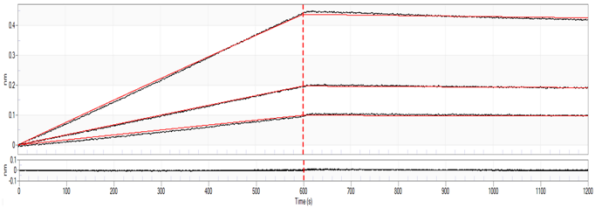

	Conc. (nM)	KD (M)	kon(1/Ms)	kdis(1/s)	Full R^2
Local Fit	5	2.65E-09	2.00E+04	5.30E-05	0.9985
	2.5	<1.0E-12	3.63E+05	<1.0E-07	0.9868
	1.25	<1.0E-12	7.27E+05	<1.0E-07	0.9505
Global Fit		3.92E-09	1.16E+04	4.53E-05	0.999

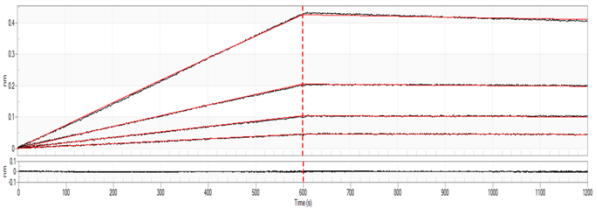

	Conc. (nM)	KD (M)	kon(1/Ms)	kdis(1/s)	Full R^2
Local Fit	5	6.42E-09	1.12E+04	7.16E-05	0.9994
	2.5	<1.0E-12	3.96E+05	<1.0E-07	0.9906
	1.25	<1.0E-12	7.80E+05	<1.0E-07	0.9872
	0.625	<1.0E-12	4.14E+05	<1.0E-07	0.9906
Global Fit		5.88E-09	1.01E+04	5.94E-05	0.9997

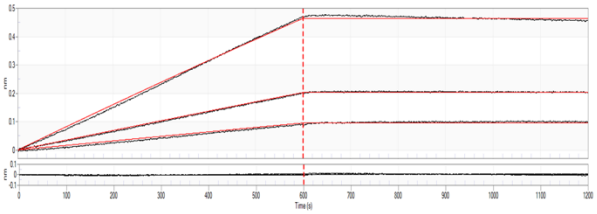

	Conc. (nM)	KD (M)	kon(1/Ms)	kdis(1/s)	Full R^2
Local Fit	10	4.61E-09	8.78E+04	4.04E-04	0.9939
	5	<1.0E-12	1.81E+05	<1.0E-07	0.9875
	2.5	<1.0E-12	1.24E+05	<1.0E-07	0.9958
	1.25	<1.0E-12	4.18E+05	<1.0E-07	0.9622
Global Fit		<1.0E-12	3.29E+04	<1.0E-07	0.9989

D56A ParD1 (Ni-NTA Pin) + WT ParE1

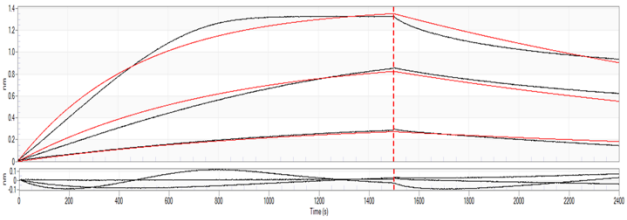

	Conc. (nM)	KD (M)	kon(1/Ms)	kdis(1/s)	Full R^2
Local Fit	10	3.08E-09	1.68E+05	5.17E-04	0.9655
	5	7.06E-09	5.44E+04	3.84E-04	0.9988
	2.5	2.00E-08	3.65E+04	7.28E-04	0.9987
Global Fit		2.73E-09	1.64E+05	4.48E-04	0.9868

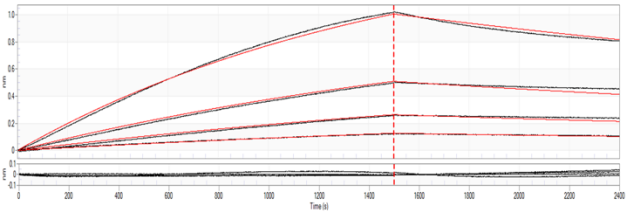

	Conc. (nM)	KD (M)	kon(1/Ms)	kdis(1/s)	Full R^2
Local Fit	5	4.57E-09	6.57E+04	3.00E-04	0.9979
	2.5	1.49E-09	8.00E+04	1.19E-04	0.9996
	1.25	4.65E-09	2.07E+04	9.62E-05	0.9982
	0.625	2.90E-10	5.30E+05	1.54E-04	0.9986
Global Fit		2.67E-09	8.71E+04	2.32E-04	0.9977

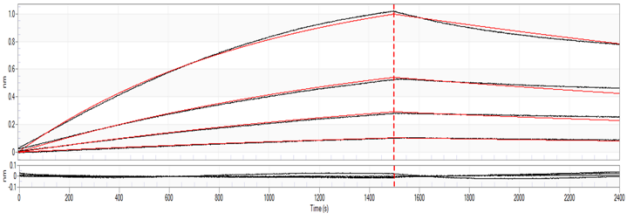

	Conc. (nM)	KD (M)	kon(1/Ms)	kdis(1/s)	Full R^2
Local Fit	5	2.76E-09	1.22E+05	3.36E-04	0.998
	2.5	6.73E-10	2.14E+05	1.44E-04	0.9991
	1.25	3.59E-10	2.95E+05	1.06E-04	0.9995
	0.625	3.76E-09	4.12E+04	1.55E-04	0.9965
Global Fit		1.83E-09	1.47E+05	2.69E-04	0.9982

L62A ParD1 (Ni-NTA Pin) + WT ParE1

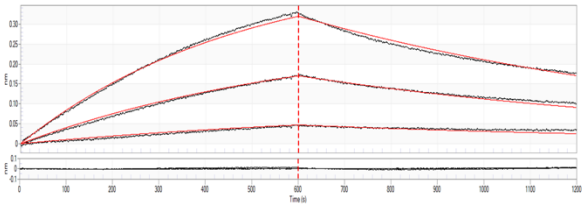

	Conc. (nM)	KD (M)	kon(1/Ms)	kdis(1/s)	Full R^2
Local Fit	5	5.78E-09	1.93E+05	1.12E-03	0.995
	2.5	7.17E-09	1.29E+05	9.27E-04	0.9974
	0.625	5.84E-09	8.74E+04	5.10E-04	0.9875
Global Fit		4.80E-09	2.18E+05	1.05E-03	0.9971

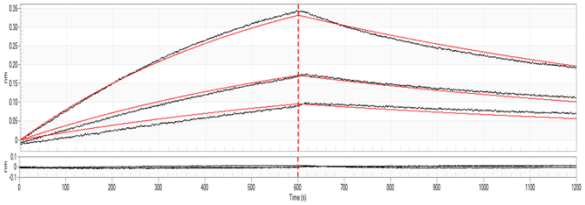

	Conc. (nM)	KD (M)	kon(1/Ms)	kdis(1/s)	Full R^2
Local Fit	10	7.82E-09	1.81E+05	1.41E-03	0.9893
	5	8.01E-09	1.30E+05	1.04E-03	0.9973
	2.5	3.67E-08	1.85E+04	6.77E-04	0.9953
	1.25	6.39E-09	4.33E+04	2.76E-04	0.967
Global Fit		4.99E-09	1.76E+05	8.76E-04	0.9897

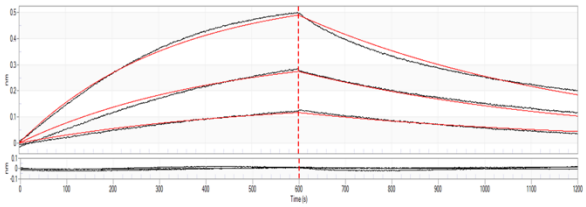

	Conc. (nM)	KD (M)	kon(1/Ms)	kdis(1/s)	Full R^2
Local Fit	10	1.11E-08	1.52E+05	1.69E-03	0.99
	5	1.50E-07	1.00E+04	1.51E-03	0.9915
	2.5	6.29E-08	2.74E+04	1.72E-03	0.9799
Global Fit		1.12E-08	1.45E+05	1.63E-03	0.9934

L63A ParD1 (Ni-NTA Pin) + WT ParE1

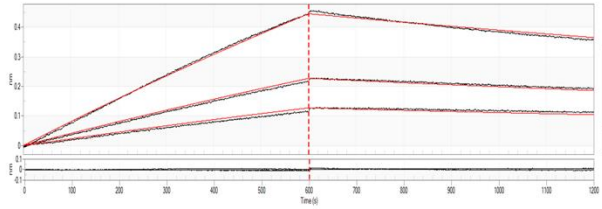

	Conc. (nM)	KD (M)	kon(1/Ms)	kdis(1/s)	Full R^2
Local Fit	5	3.15E-08	1.21E+04	3.81E-04	0.9991
	2.5	9.70E-09	2.11E+04	2.05E-04	0.9978
	1.25	<1.0E-12	7.18E+05	<1.0E-07	0.9812
Global Fit		8.10E-08	4.10E+03	3.32E-04	0.9979

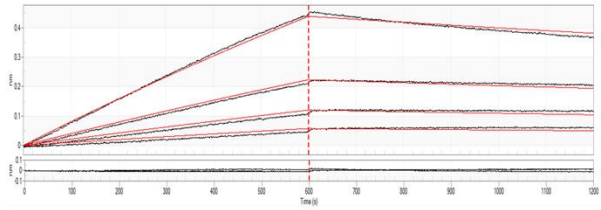

	Conc. (nM)	KD (M)	kon(1/Ms)	kdis(1/s)	Full R^2
Local Fit	10	6.78E-09	1.10E+05	7.43E-04	0.9933
	5	2.46E-08	1.37E+04	3.36E-04	0.9993
	2.5	1.41E-09	3.91E+04	5.51E-05	0.9978
	1.25	<1.0E-12	4.89E+05	<1.0E-07	0.9683
Global Fit		7.60E-09	3.10E+04	2.35E-04	0.996

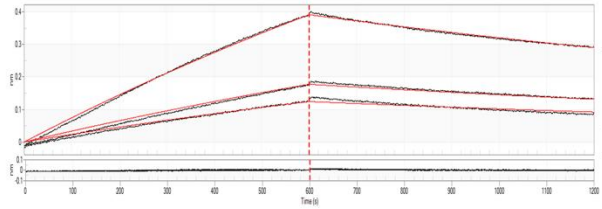

	Conc. (nM)	KD (M)	kon(1/Ms)	kdis(1/s)	Full R^2
	5	4.37E-08	1.17E+04	5.12E-04	0.998
	2.5	1.46E-08	2.68E+04	3.89E-04	0.9867
	1.25	1.03E-08	5.41E+04	5.58E-04	0.9757
Global Fit		7.05E-08	7.10E+03	5.00E-04	0.9971

E64A ParD1 (Ni-NTA Pin) + WT ParE1

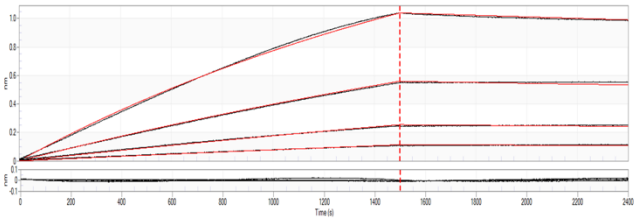

	Conc. (nM)	KD (M)	kon(1/Ms)	kdis(1/s)	Full R^2
Local Fit	5	1.03E-09	7.74E+04	7.93E-05	0.9992
	2.5	<1.0E-12	2.17E+05	<1.0E-07	0.9931
	1.25	<1.0E-12	4.57E+05	<1.0E-07	0.9939
	0.625	<1.0E-12	6.44E+05	<1.0E-07	0.99
Global Fit		6.14E-10	8.74E+04	5.36E-05	0.9995

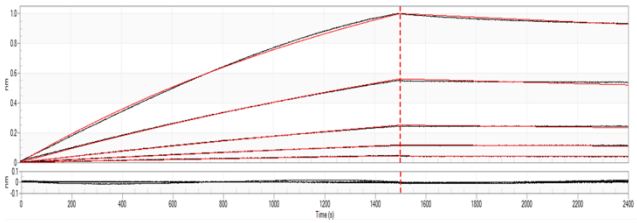

	Conc. (nM)	KD (M)	kon(1/Ms)	kdis(1/s)	Full R^2
Local Fit	5	1.18E-09	8.81E+04	1.04E-04	0.9989
	2.5	<1.0E-12	2.50E+05	<1.0E-07	0.9971
	1.25	<1.0E-12	4.56E+05	<1.0E-07	0.9951
	0.625	<1.0E-12	9.15E+05	<1.0E-07	0.9943
	0.3125	1.22E-10	1.13E+06	1.38E-04	0.984
Global Fit		8.51E-10	9.82E+04	8.36E-05	0.9996

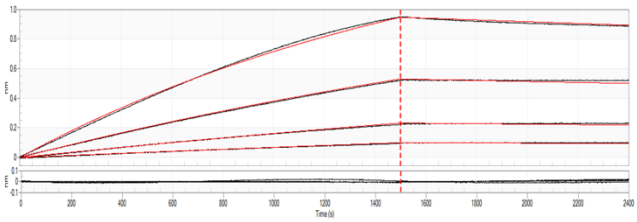

	Conc. (nM)	KD (M)	kon(1/Ms)	kdis(1/s)	Full R^2
Local Fit	5	1.14E-09	8.67E+04	9.91E-05	9.99E-01
	2.5	<1.0E-12	2.22E+05	<1.0E-07	9.94E-01
	1.25	<1.0E-12	4.13E+05	<1.0E-07	9.91E-01
	0.625	<1.0E-12	6.64E+05	<1.0E-07	9.85E-01
Global Fit		6.51E-10	9.93E+04	6.46E-05	9.99E-01

H65A ParD1 (Ni-NTA Pin) + WT ParE1

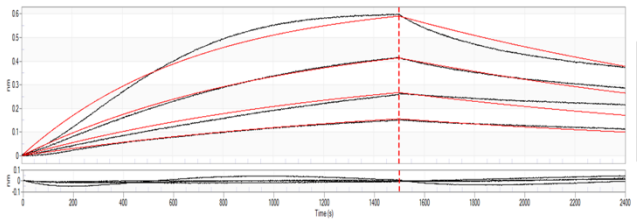

	Conc. (nM)	KD (M)	kon(1/Ms)	kdis(1/s)	Full R^2
Local Fit	5	4.79E-09	1.38E+05	6.61E-04	0.9739
	2.5	3.05E-09	1.52E+05	4.63E-04	0.9962
	1.25	1.66E-09	1.34E+05	2.22E-04	0.9995
	0.625	7.95E-10	4.29E+05	3.41E-04	0.9954
Global Fit		2.62E-09	1.90E+05	4.96E-04	0.986

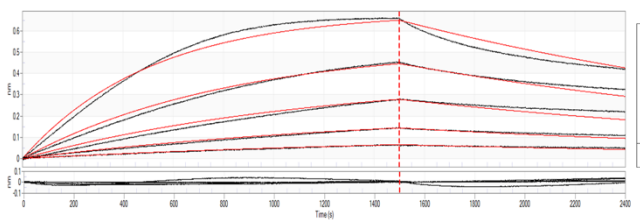

	Conc. (nM)	KD (M)	kon(1/Ms)	kdis(1/s)	Full R^2
Local Fit	5	2.37E-09	2.62E+05	6.22E-04	0.9814
	2.5	2.08E-09	2.01E+05	4.19E-04	0.9971
	1.25	2.10E-09	1.36E+05	2.86E-04	0.9988
	0.625	1.43E-09	2.25E+05	3.23E-04	0.9984
	0.3125	3.71E-10	7.60E+05	2.82E-04	0.9951
Global Fit		1.58E-09	2.98E+05	4.70E-04	0.9922

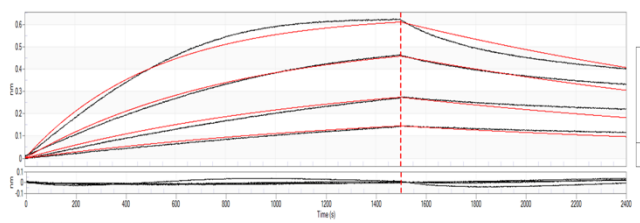

	Conc. (nM)	KD (M)	kon(1/Ms)	kdis(1/s)	Full R^2
Local Fit	5	2.36E-09	2.57E+05	6.08E-04	0.9821
	2.5	1.66E-09	2.50E+05	4.15E-04	0.9972
	1.25	1.79E-09	1.42E+05	2.54E-04	0.9993
	0.625	2.95E-09	8.34E+04	2.46E-04	0.9993
Global Fit		1.50E-09	3.01E+05	4.52E-04	0.99

I66A ParD1 (Ni-NTA Pin) + WT ParE1

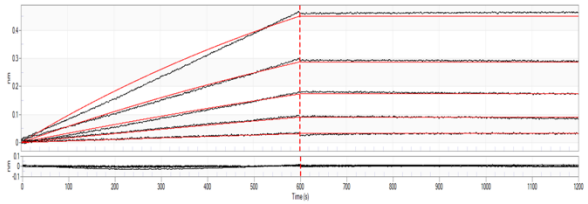

	Conc. (nM)	KD (M)	kon(1/Ms)	kdis(1/s)	Full R^2
Local Fit	5	<1.0E-12	1.96E+05	<1.0E-07	0.9894
	3.5	<1.0E-12	1.74E+05	<1.0E-07	0.997
	2.5	<1.0E-12	3.45E+05	<1.0E-07	0.9831
	1.25	4.43E-10	3.12E+05	1.38E-04	0.9961
	0.625	<1.0E-12	2.77E+06	<1.0E-07	0.9526
Global Fit		<1.0E-12	2.07E+05	<1.0E-07	0.9967

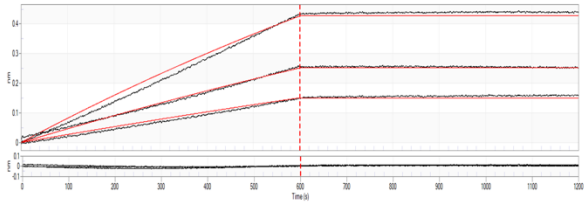

	Conc. (nM)	KD (M)	kon(1/Ms)	kdis(1/s)	Full R^2
Local Fit	5	<1.0E-12	5.97E+04	<1.0E-07	0.995
	3.5	<1.0E-12	1.68E+05	<1.0E-07	0.9929
	2.5	<1.0E-12	4.57E+05	<1.0E-07	0.956
Global Fit		<1.0E-12	1.14E+05	<1.0E-07	0.9947

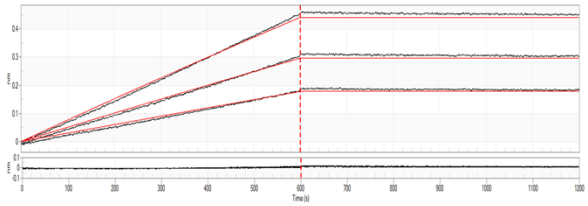

	Conc. (nM)	KD (M)	kon(1/Ms)	kdis(1/s)	Full R^2
Local Fit	5	<1.0E-12	1.77E+05	<1.0E-07	0.9844
	3.5	<1.0E-12	2.41E+05	<1.0E-07	0.9797
	2.5	<1.0E-12	2.44E+05	<1.0E-07	0.9773
Global Fit		<1.0E-12	2.97E+04	<1.0E-07	0.9958

I68A ParD1 (Ni-NTA Pin) + WT ParE1

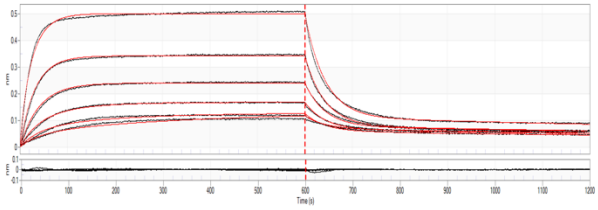

	Conc. (nM)	KD (M)	kon(1/Ms)	kdis(1/s)	Full R^2
Local Fit	100	9.51E-08	2.88E+05	2.74E-02	0.9992
	50	1.30E-07	1.91E+05	2.50E-02	0.9994
	25	1.42E-07	1.54E+05	2.19E-02	0.9995
	12.5	4.19E-07	5.13E+04	2.15E-02	0.9988
	6.25	1.86E-07	8.87E+04	1.65E-02	0.9967
	3.125	1.39E-07	1.11E+05	1.55E-02	0.9957
Global Fit		2.22E-07	1.09E+05	2.40E-02	0.9989

	Conc. (nM)	KD2 (M)	kon2 (1/Ms)	kdis2 (1/s)	Full R^2
Local Fit	100	3.51E-09	1.82E+05	6.40E-04	0.9992
	50	1.93E-09	3.44E+05	6.64E-04	0.9994
	25	8.88E-10	5.79E+05	5.14E-04	0.9995
	12.5	3.98E-10	9.52E+05	3.79E-04	0.9988
	6.25	1.85E-10	1.71E+06	3.17E-04	0.9967
	3.125	4.89E-11	2.45E+06	1.20E-04	0.9957
Global Fit		5.92E-10	7.82E+05	4.63E-04	0.9989

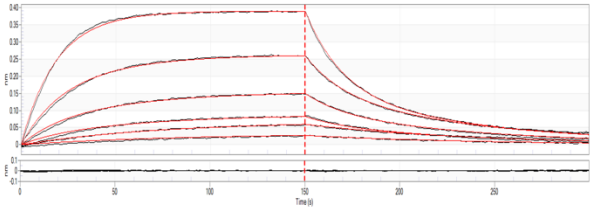

	Conc. (nM)	KD (M)	kon(1/Ms)	kdis(1/s)	Full R^2
Local Fit	100	1.67E-06	3.20E+04	5.34E-02	0.9996
	50	1.20E-06	3.15E+04	3.77E-02	0.9996
	25	3.52E-07	7.47E+04	2.63E-02	0.9992
	12.5	2.13E-07	8.88E+04	1.90E-02	0.995
	6.25	6.18E-08	2.36E+05	1.46E-02	0.9929
	3.125	1.63E-07	6.04E+04	9.83E-03	0.9332
Global Fit		5.18E-07	9.92E+04	5.14E-02	0.9992

	Conc. (nM)	KD2 (M)	kon2 (1/Ms)	kdis2 (1/s)	Full R^2
Local Fit	100	2.69E-08	4.01E+05	1.08E-02	0.9996
	50	1.61E-08	4.37E+05	7.03E-03	0.9996
	25	7.53E-09	6.95E+05	5.23E-03	0.9992
	12.5	4.68E-09	8.17E+05	3.82E-03	0.995
	6.25	<1.0E-12	7.47E+05	<1.0E-07	0.9929
	3.125	1.68E-07	6.04E+04	1.01E-02	0.9332
Global Fit		3.42E-08	3.24E+05	1.11E-02	0.9992

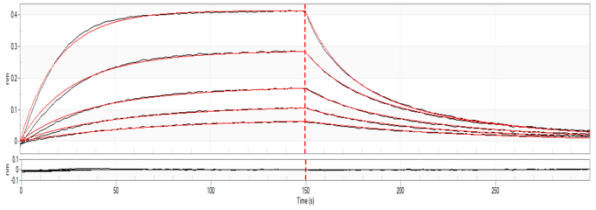

	Conc. (nM)	KD (M)	kon(1/Ms)	kdis(1/s)	Full R^2
Local Fit	100	2.38E-06	2.19E+04	5.20E-02	0.999
	50	1.19E-06	2.73E+04	3.26E-02	0.9986
	25	2.96E-07	7.51E+04	2.22E-02	0.998
	12.5	1.08E-07	1.77E+05	1.90E-02	0.9951
	6.25	5.48E-08	2.93E+05	1.60E-02	0.9906
Global Fit		1.14E-06	4.58E+04	5.22E-02	0.9987

	Conc. (nM)	KD2 (M)	kon2 (1/Ms)	kdis2 (1/s)	Full R^2
Local Fit	100	3.29E-08	3.55E+05	1.17E-02	0.999
	50	1.66E-08	4.37E+05	7.25E-03	0.9986
	25	1.97E-09	7.70E+05	1.52E-03	0.998
	12.5	<1.0E-12	1.07E+05	<1.0E-07	0.9951
	6.25	<1.0E-12	2.31E+05	<1.0E-07	0.9906
Global Fit		4.18E-08	2.96E+05	1.24E-02	0.9987

E69A ParD1 (Ni-NTA Pin) + WT ParE1

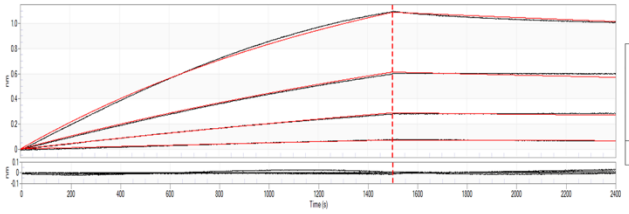

	Conc. (nM)	KD (M)	kon(1/Ms)	kdis(1/s)	Full R^2
Local Fit	5	1.21E-09	9.84E+04	1.19E-04	0.9985
	2.5	<1.0E-12	2.25E+05	<1.0E-07	0.9949
	1.25	<1.0E-12	4.38E+05	<1.0E-07	0.9934
	0.625	2.37E-09	3.30E+04	7.82E-05	0.9815
Global Fit		6.99E-10	1.12E+05	7.85E-05	0.9991

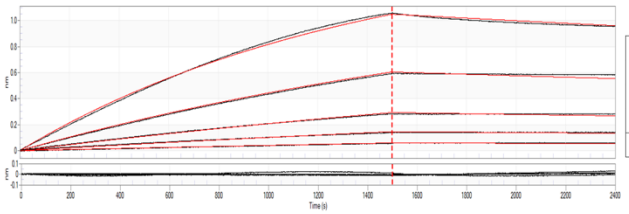

	Conc. (nM)	KD (M)	kon(1/Ms)	kdis(1/s)	Full R^2
Local Fit	5	1.27E-09	1.10E+05	1.40E-04	0.9988
	2.5	<1.0E-12	2.42E+05	<1.0E-07	0.9967
	1.25	<1.0E-12	4.89E+05	<1.0E-07	0.9967
	0.625	<1.0E-12	7.49E+05	<1.0E-07	0.9981
Global Fit		7.80E-10	1.26E+05	9.80E-05	0.9992

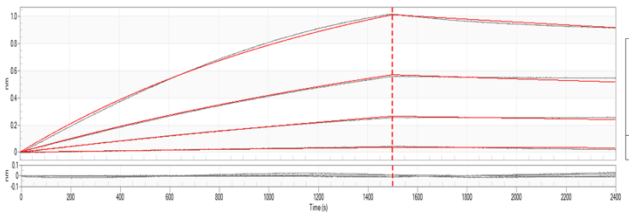

	Conc. (nM)	KD (M)	kon(1/Ms)	kdis(1/s)	Full R^2
Local Fit	5	1.36E-09	1.09E+05	1.48E-04	0.9984
	2.5	<1.0E-12	2.47E+05	<1.0E-07	0.997
	1.25	<1.0E-12	4.75E+05	<1.0E-07	0.9961
	0.625	2.00E-08	2.58E+04	5.14E-04	0.9426
Global Fit		8.89E-10	1.23E+05	1.10E-04	0.9991

R71A ParD1 (Ni-NTA Pin) + WT ParE1

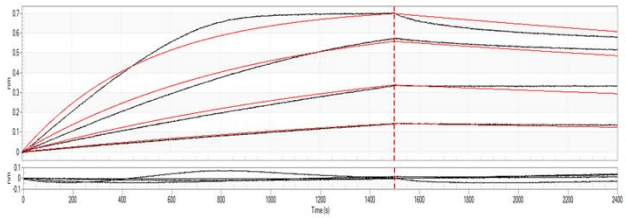

	Conc. (nM)	KD (M)	kon(1/Ms)	kdis(1/s)	Full R^2
Local Fit	5	8.65E-10	3.52E+05	3.04E-04	0.9724
	2.5	7.33E-10	1.93E+05	1.42E-04	0.9989
	1.25	<1.0E-12	4.50E+05	<1.0E-07	0.9946
	0.625	3.05E-10	1.77E+05	5.40E-05	0.9994
Global Fit		4.21E-10	3.69E+05	1.55E-04	0.9875

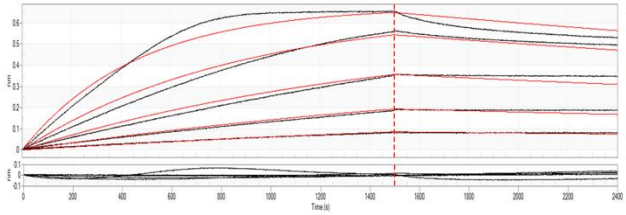

	Conc. (nM)	KD (M)	kon(1/Ms)	kdis(1/s)	Full R^2
Local Fit	5	8.71E-10	3.81E+05	3.32E-04	0.9719
	2.5	7.36E-10	2.20E+05	1.62E-04	0.9989
	1.25	<1.0E-12	4.56E+05	<1.0E-07	0.9951
	0.625	<1.0E-12	8.91E+05	<1.0E-07	0.9928
	0.3125	1.69E-12	1.75E+06	2.96E-06	0.9974
Global Fit		3.95E-10	4.01E+05	1.59E-04	0.9889

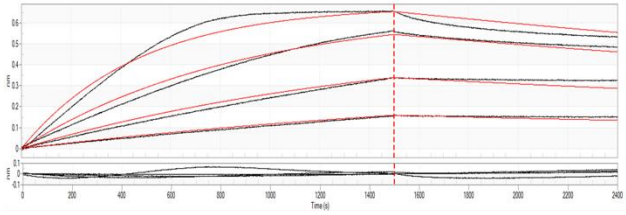

	Conc. (nM)	KD (M)	kon(1/Ms)	kdis(1/s)	Full R^2
Local Fit	5	8.80E-10	3.72E+05	3.28E-04	0.9711
	2.5	8.31E-10	2.30E+05	1.91E-04	0.9982
	1.25	<1.0E-12	4.69E+05	<1.0E-07	0.9956
	0.625	<1.0E-12	8.78E+05	<1.0E-07	0.9933
Global Fit		4.77E-10	3.88E+05	1.85E-04	0.9878

W72A ParD1 (Ni-NTA Pin) + WT ParE1

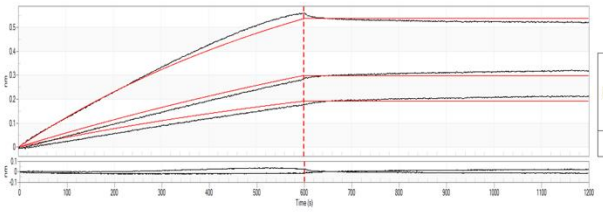

	Conc. (nM)	KD (M)	kon(1/Ms)	kdis(1/s)	Full R^2
Local Fit	5	5.10E-10	2.59E+05	1.32E-04	0.9966
	3.5	<1.0E-12	8.46E+04	<1.0E-07	0.9638
	1.25	<1.0E-12	1.55E+04	<1.0E-07	0.9902
Global Fit		<1.0E-12	2.74E+05	<1.0E-07	0.9908

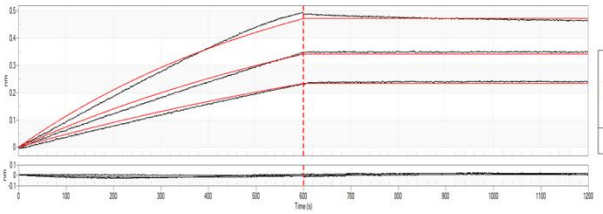

	Conc. (nM)	KD (M)	kon(1/Ms)	kdis(1/s)	Full R^2
Local Fit	5	8.68E-10	1.45E+05	1.26E-04	0.9983
	3.5	<1.0E-12	3.58E+05	<1.0E-07	0.9876
	2.5	<1.0E-12	1.24E+05	<1.0E-07	0.9967
Global Fit		<1.0E-12	3.24E+05	<1.0E-07	0.9938

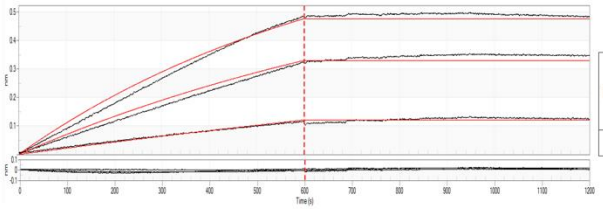

	Conc. (nM)	KD (M)	kon(1/Ms)	kdis(1/s)	Full R^2
Local Fit	5	<1.0E-12	2.68E+05	<1.0E-07	0.9914
	3.5	<1.0E-12	3.33E+05	<1.0E-07	0.9743
	1.25	<1.0E-12	1.11E+06	<1.0E-07	0.9678
Global Fit		<1.0E-12	2.87E+05	<1.0E-07	0.9932

L74A ParD1 (Ni-NTA Pin) + WT ParE1

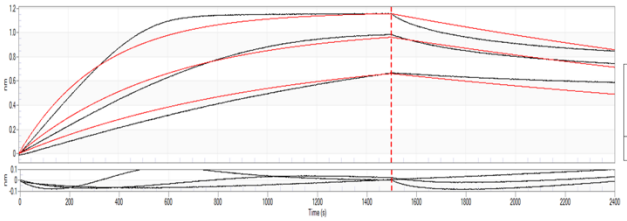

	Conc. (nM)	KD (M)	kon(1/Ms)	kdis(1/s)	Full R^2
Local Fit	12.5	2.06E-09	2.21E+05	4.56E-04	0.9624
	6.25	2.69E-09	1.46E+05	3.93E-04	0.9892
	3.13	2.09E-09	7.60E+04	1.59E-04	0.9988
Global Fit		1.55E-09	2.14E+05	3.31E-04	0.9727

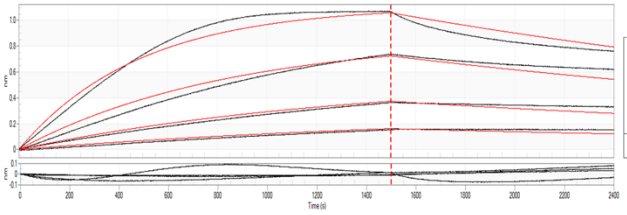

	Conc. (nM)	KD (M)	kon(1/Ms)	kdis(1/s)	Full R^2
Local Fit	12.5	3.88E-09	1.27E+05	4.93E-04	0.975
	6.25	3.09E-09	7.11E+04	2.19E-04	0.9988
	3.13	8.02E-10	1.34E+05	1.07E-04	0.9999
	1.56	<1.0E-12	3.76E+05	<1.0E-07	0.9812
Global Fit		2.30E-09	1.39E+05	3.20E-04	0.9864

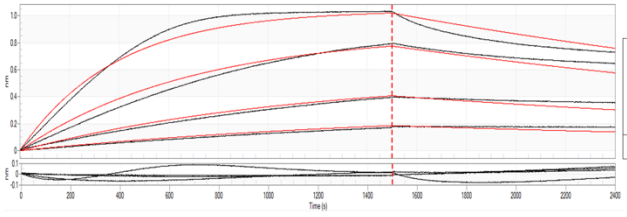

	Conc. (nM)	KD (M)	kon(1/Ms)	kdis(1/s)	Full R^2
Local Fit	12.5	2.85E-09	1.75E+05	5.00E-04	0.9732
	6.25	2.41E-09	1.09E+05	2.63E-04	0.9984
	3.13	7.26E-10	1.75E+05	1.27E-04	0.9996
	1.56	<1.0E-12	3.79E+05	<1.0E-07	0.9948
Global Fit		1.82E-09	1.80E+05	3.29E-04	0.9866

mCh-WT ParD1 (Ni-NTA Pin) + WT ParE1

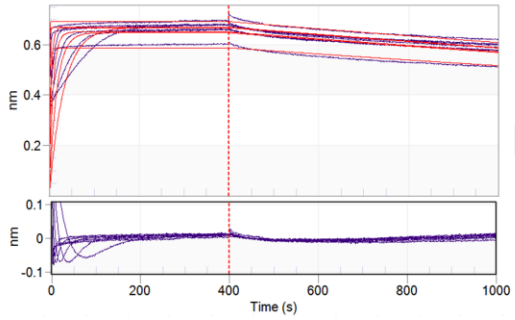

	Conc. (nM)	KD (M)	kon(1/Ms)	kdis(1/s)	Full R^2
Global Fit		5.47E-11	3.93E+06	2.15E-04	0.8257

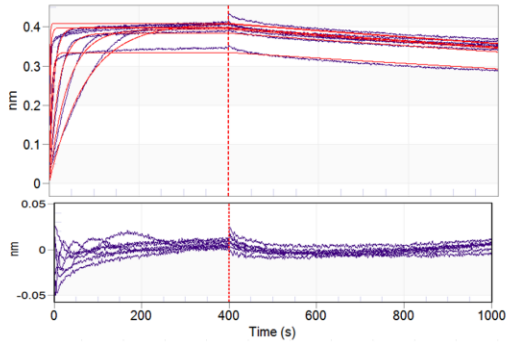

	Conc. (nM)	KD (M)	kon(1/Ms)	kdis(1/s)	Full R^2
Global Fit		1.46E-10	1.53E+06	2.22E-04	0.9766

mCh-WT ParD1$_{42-75}$ (Ni-NTA Pin) + WT ParE1

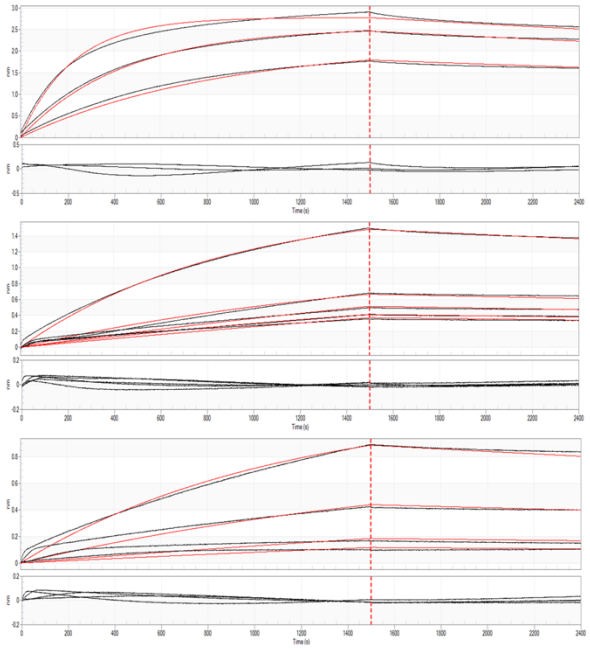

	Conc. (nM)	KD (M)	kon(1/Ms)	kdis(1/s)	Full R^2
Local Fit	10	2.64E-10	3.87E+05	1.02E-04	0.9856
	5	1.66E-10	4.78E+05	7.93E-05	0.9979
	2.5	1.75E-10	6.13E+05	1.07E-04	0.9994
Global Fit		2.56E-10	4.34E+05	1.11E-04	0.9924

	Conc. (nM)	KD (M)	kon(1/Ms)	kdis(1/s)	Full R^2
Local Fit	10	7.78E-10	1.11E+05	8.62E-05	0.9976
	5	<1.0E-12	1.14E+05	<1.0E-07	0.993
	2.5	<1.0E-12	2.96E+05	<1.0E-07	0.9894
	1.25	<1.0E-12	7.54E+05	<1.0E-07	0.9813
	0.625	3.11E-12	1.78E+06	5.55E-06	0.9831
Global Fit		8.77E-10	1.06E+05	9.29E-05	0.9959

	Conc. (nM)	KD (M)	kon(1/Ms)	kdis(1/s)	Full R^2
Local Fit	10	6.01E-10	8.47E+04	5.09E-05	0.9928
	5	1.92E-11	2.85E+05	5.48E-06	0.9645
	0.625	1.40E-11	4.86E+06	6.81E-05	0.9812
	0.3125	<1.0E-12	8.72E+06	<1.0E-07	0.9855
Global Fit		1.35E-09	8.02E+04	1.09E-04	0.9882

mCh-I68A ParD142-75 (Ni-NTA Pin) + WT ParE1

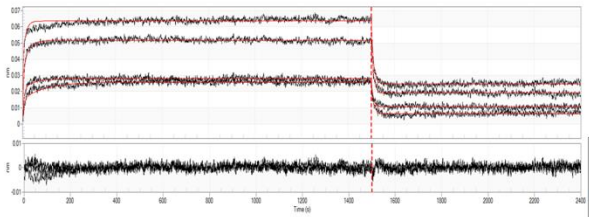

	Conc. (nM)	KD (M)	kon(1/Ms)	kdis(1/s)	Full R^2
Local Fit	50	3.64E-08	2.40E+06	8.71E-02	0.9901
	25	2.94E-08	2.84E+06	8.33E-02	0.9933
	12.5	4.17E-08	2.29E+06	9.54E-02	0.9964
	6.25	5.39E-07	2.99E+05	1.61E-01	0.971
	3.125	1.77E-07	5.65E+05	1.00E-01	0.9907
Global Fit		4.29E-08	2.08E+06	8.92E-02	0.9929

	Conc. (nM)	KD2 (M)	kon2 (1/Ms)	kdis2 (1/s)	Full R^2
Local Fit	50	3.55E-09	3.76E+04	1.34E-04	0.9901
	25	8.44E-10	1.31E+05	1.10E-04	0.9933
	12.5	<1.0E-12	2.89E+05	<1.0E-07	0.9964
	6.25	2.25E-08	1.39E+06	3.13E-02	0.971
	3.125	4.44E-10	2.32E+06	1.03E-03	0.9907
Global Fit		7.72E-10	1.80E+05	1.39E-04	0.9929

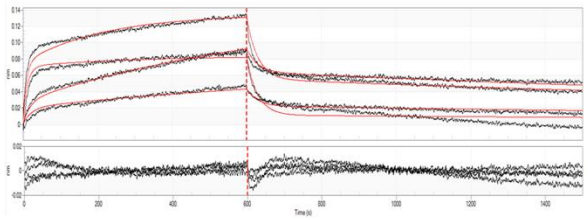

	Conc. (nM)	KD (M)	kon(1/Ms)	kdis(1/s)	Full R^2
Local Fit	50	2.10E-08	2.60E+06	5.45E-02	0.9914
	35	1.22E-07	5.65E+05	6.89E-02	0.9943
	12.5	1.91E-09	1.01E+05	1.92E-04	0.9857
	6.25	1.78E-07	1.92E+05	3.40E-02	0.9775
Global Fit		2.24E-08	1.54E+06	3.45E-02	0.9847

	Conc. (nM)	KD2 (M)	kon2 (1/Ms)	kdis2 (1/s)	Full R^2
Local Fit	50	4.75E-09	9.23E+04	4.38E-04	0.9914
	35	5.94E-08	5.19E+04	3.08E-03	0.9943
	12.5	3.11E-08	1.62E+06	5.04E-02	0.9857
	6.25	1.55E-08	5.36E+04	8.29E-04	0.9775
Global Fit		3.77E-09	8.58E+04	3.23E-04	0.9847

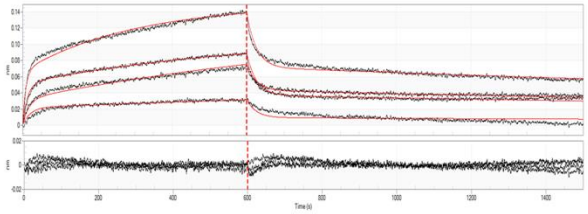

	Conc. (nM)	KD (M)	kon(1/Ms)	kdis(1/s)	Full R^2
Local Fit	50	2.53E-08	1.80E+06	4.55E-02	0.9894
	25	6.94E-08	6.55E+05	4.55E-02	0.9952
	12.5	4.94E-10	2.34E+05	1.16E-04	0.9771
	6.25	1.26E-08	2.57E+06	3.25E-02	0.9835
Global Fit		2.47E-08	1.59E+06	3.91E-02	0.9929

	Conc. (nM)	KD2 (M)	kon2 (1/Ms)	kdis2 (1/s)	Full R^2
Local Fit	50	5.52E-09	5.80E+04	3.20E-04	0.9894
	25	1.93E-09	6.38E+04	1.23E-04	0.9952
	12.5	6.22E-09	4.35E+06	2.71E-02	0.9771
	6.25	3.52E-09	5.66E+05	1.99E-03	0.9835
Global Fit		4.04E-09	6.12E+04	2.47E-04	0.9929

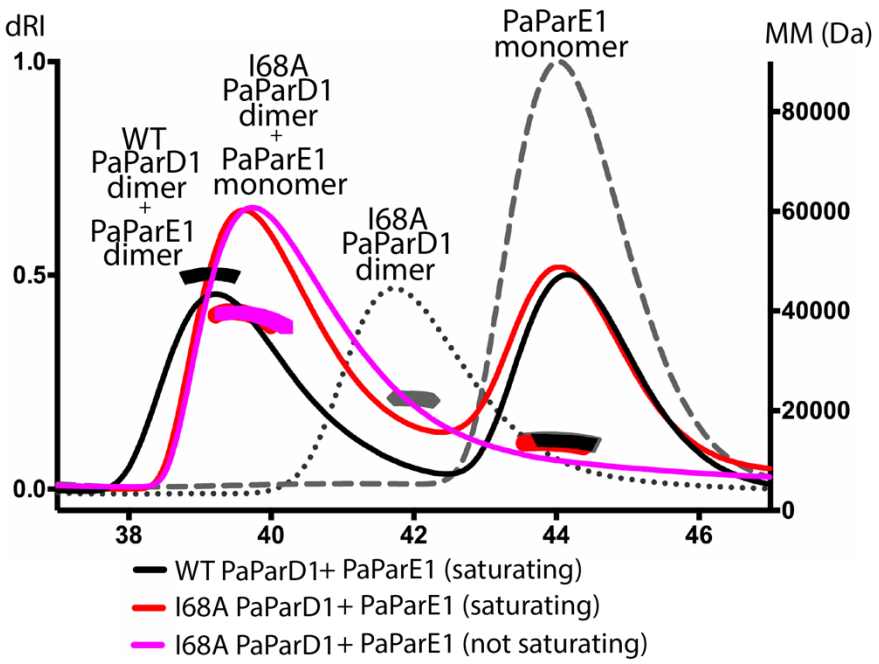

Data for all replicates (also see Fig. 3)

PaParE1	I68A PaParD1	I68A PaParD1 + PaParE1	WT PaParD1 + PaParE1
13,830 ± 6.0%			
	22,370 ± 5.3%		
**PaParE not saturating*		38,850 ± 4.4%	
13,660 ± 10.4%		38,320 ± 4.7%	
13,350 ± 6.2%		38,120 ± 4.5%	
13,690 ± 6.0%			47,040 ± 4.4%
13,740 ± 7.5%			47,260 ± 4.6%

Average values, ± SD

PaParE1	I68A PaParD1	I68A PaParD1 + PaParE1	WT PaParD1 + PaParE1
13,654 Da ± 182 Da	22,370 Da ± 377 Da	38,430 Da ± 377 Da	47,150 Da ± 156 Da
n=5	*n=1*	*n=3*	*n=2*

Figure S2.2. Replicates of Size Exclusion Chromatography – Multiangle Light Scattering experiments. Samples were separated in 50 mM MES pH 6.0, 300 mM NaCl, 5% glycerol; data processing followed manufacturer's recommendations (description given in Experimental procedures). The trial depicted by the magenta trace did not have saturating toxin, yet the same complex was generated as when excess toxin was added. Molecular weight determinations are listed here for each trial. Note, some traces are included in the text Fig. 2.6; they are reproduced again here for reference.

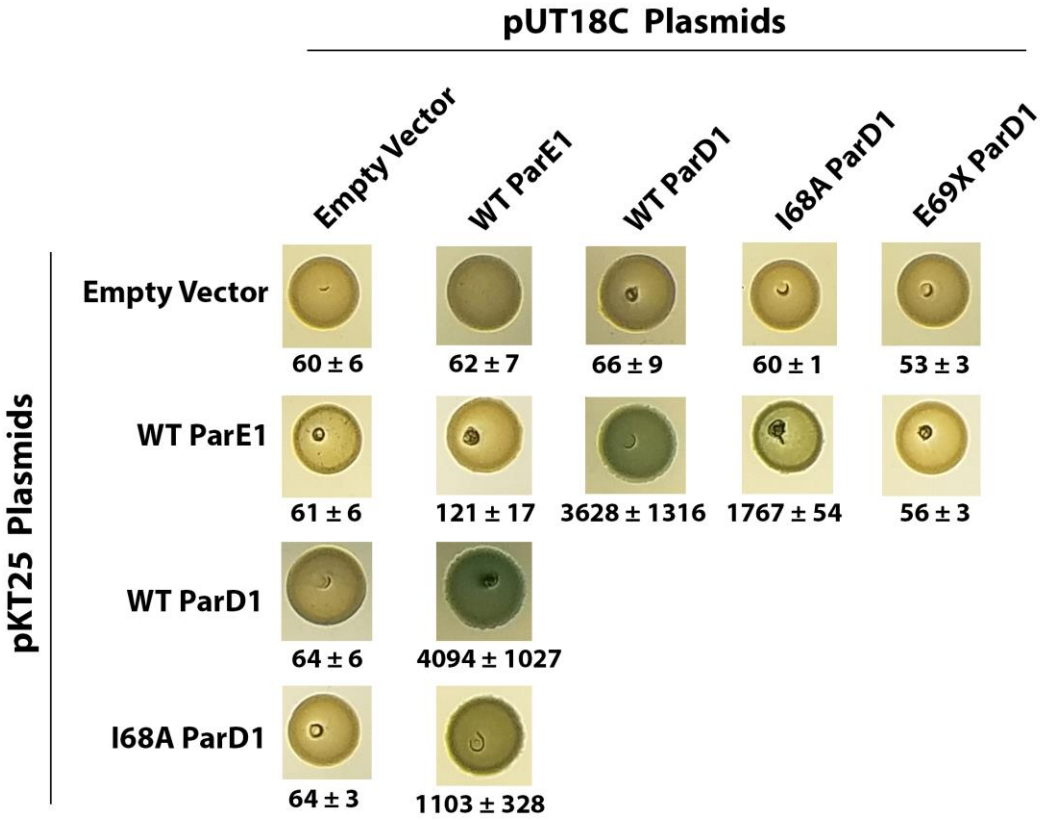

Figure S2.3. A Bacterial Two-Hybrid Screen was used to characterize the strength of interactions between PaParD1, PaParE1, and associated constructs in a cellular environment. Colony images and resulting color is representative of at least three independent replicates; Miller unit values are calculated from at least three independent replicates (e.g. different transformations). Images of each colony were obtained from the same plate and were cropped and rearranged for ease of presentation. Note: selected colonies and values are also shown in the text, Figure 2.5.

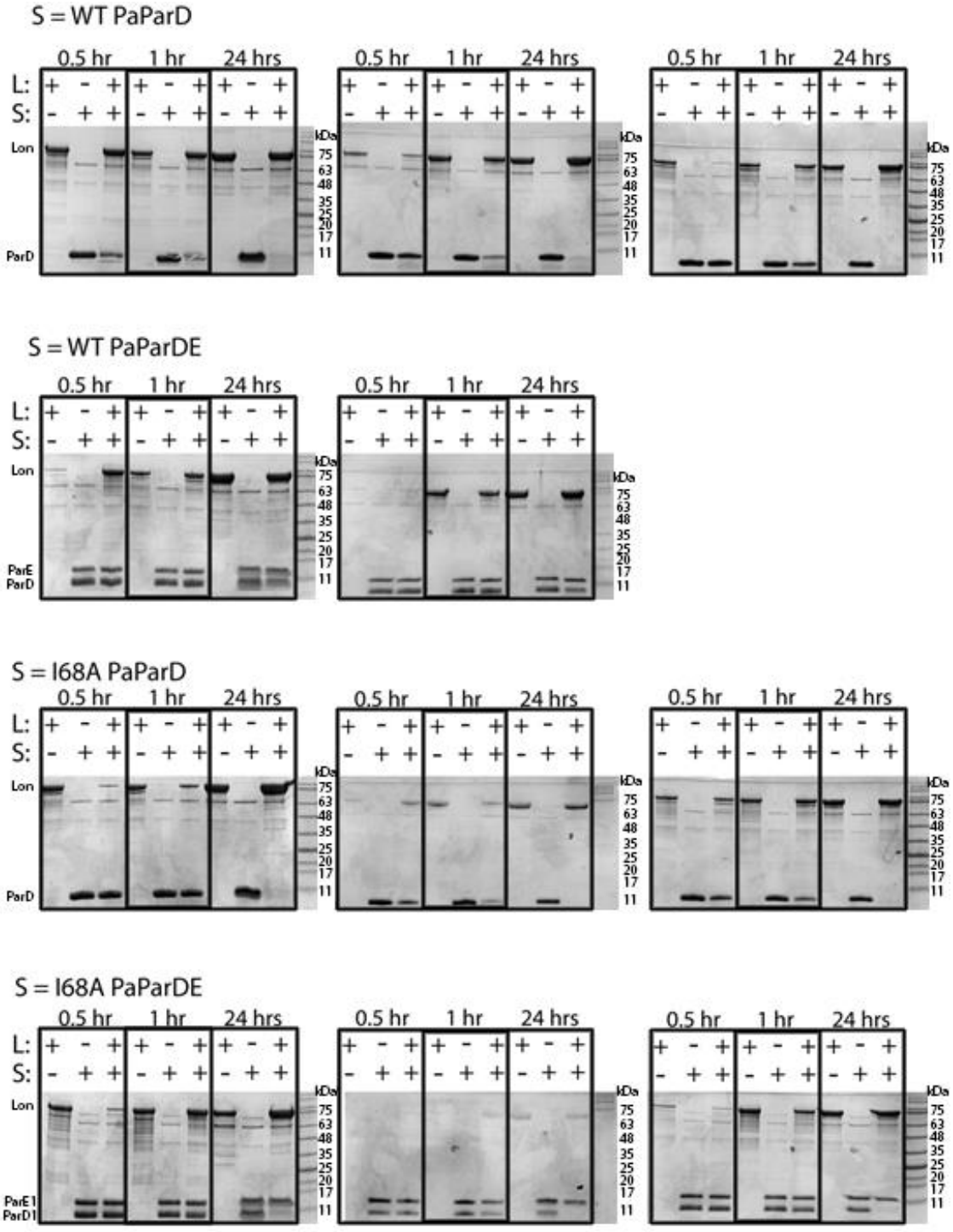

Figure S2.4. Replicate gels for the analysis of E. coli Lon digestion of PaParD1, I68A PaParD1, and the associated complexes. These data are summarized in the text, Fig. 2.7. Calculations were made as % intensity of the PaParD1 or PaParE1 band remaining in the + Lon samples ("L") as compared to the same time point without Lon. Note, boxes over images are for clarity only; each image is of a single gel and no cropping has been applied.

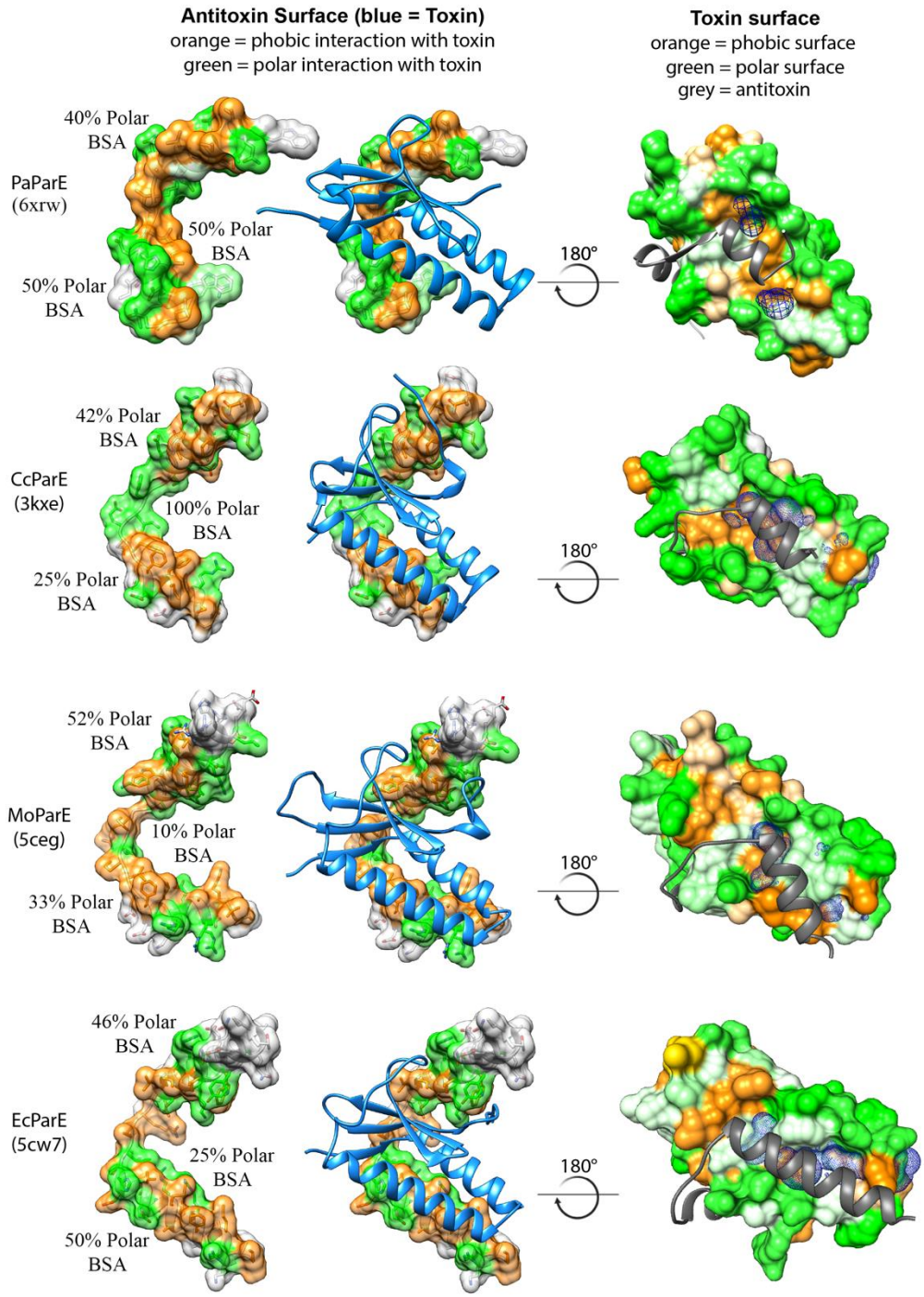

Figure S2.5. Analysis of PaParD1-PaParE1 interfaces reveals little conservation at specific positions, but commonalities in overall types of interactions and toxin surface features. The breakdown of polar (green) versus hydrophobic (orange) buried surface area (BSA) has been parsed into antitoxin α2, the five amino acid linker, and α3. Antitoxin α3 contains side chains that appear to fit into diverse cavities (blue mesh) on the toxin, the shape and depth of which are defined by toxin amino acids in the two helices. In PaParDE1, this PaParE1 toxin cavity accommodates the identified hotspot amino acid Ile68 (see text, Fig. 2.2).

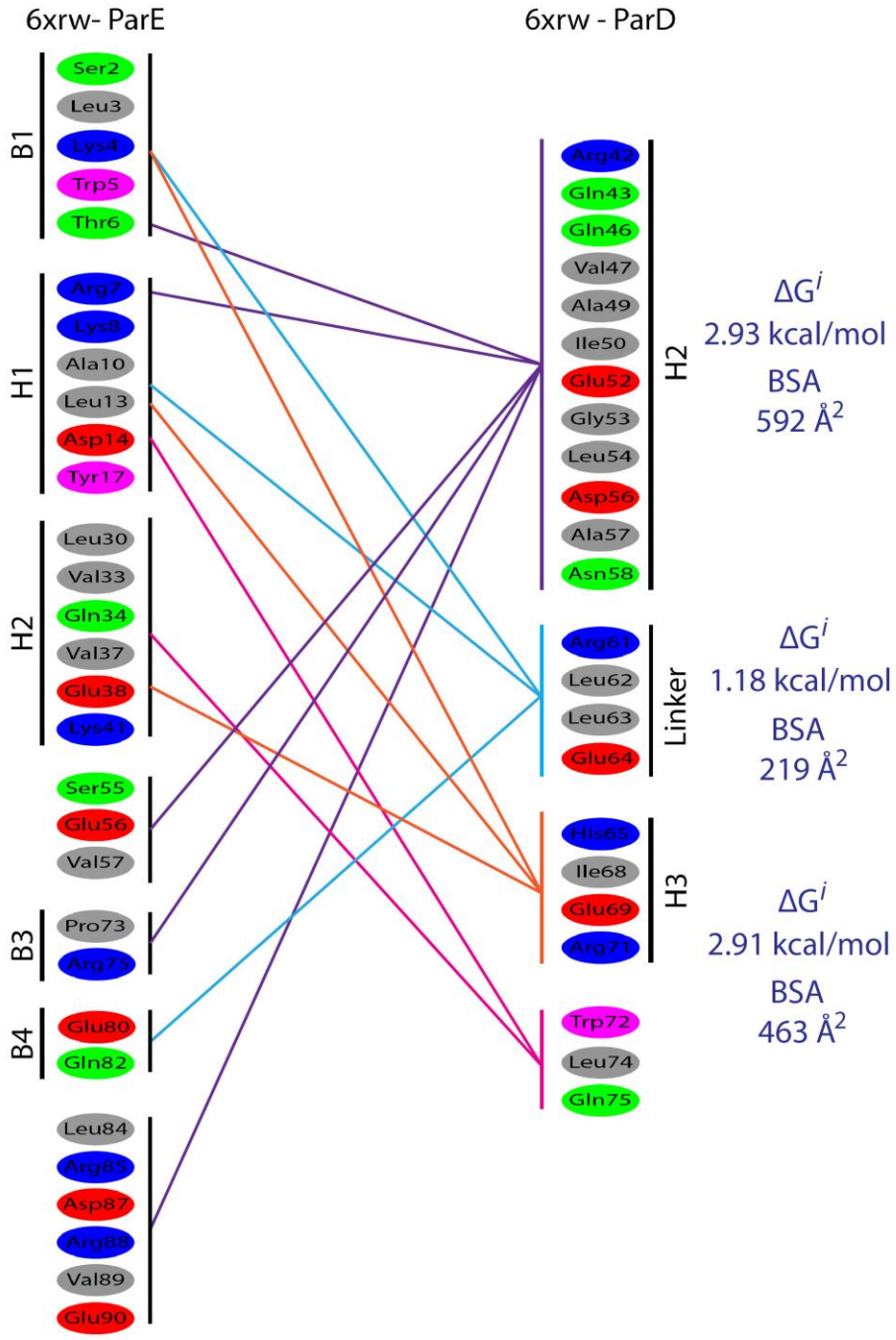

Figure S2.6 Interactions between ParD toxin-binding domains (α2, loop, α3) with cognate ParE. Interaction network of PaParD1 with PaParE1; amino acids are colored based on the scheme used in PDBsum; lines between regions are simply colored for clarity (e.g., purple for the H2 of the antitoxin, cyan for the linker, and orange for H3 of the antitoxin). Values for ΔGi and BSA were taken from the PISA web server. (Additional images for each ParDE structure on the following pages).

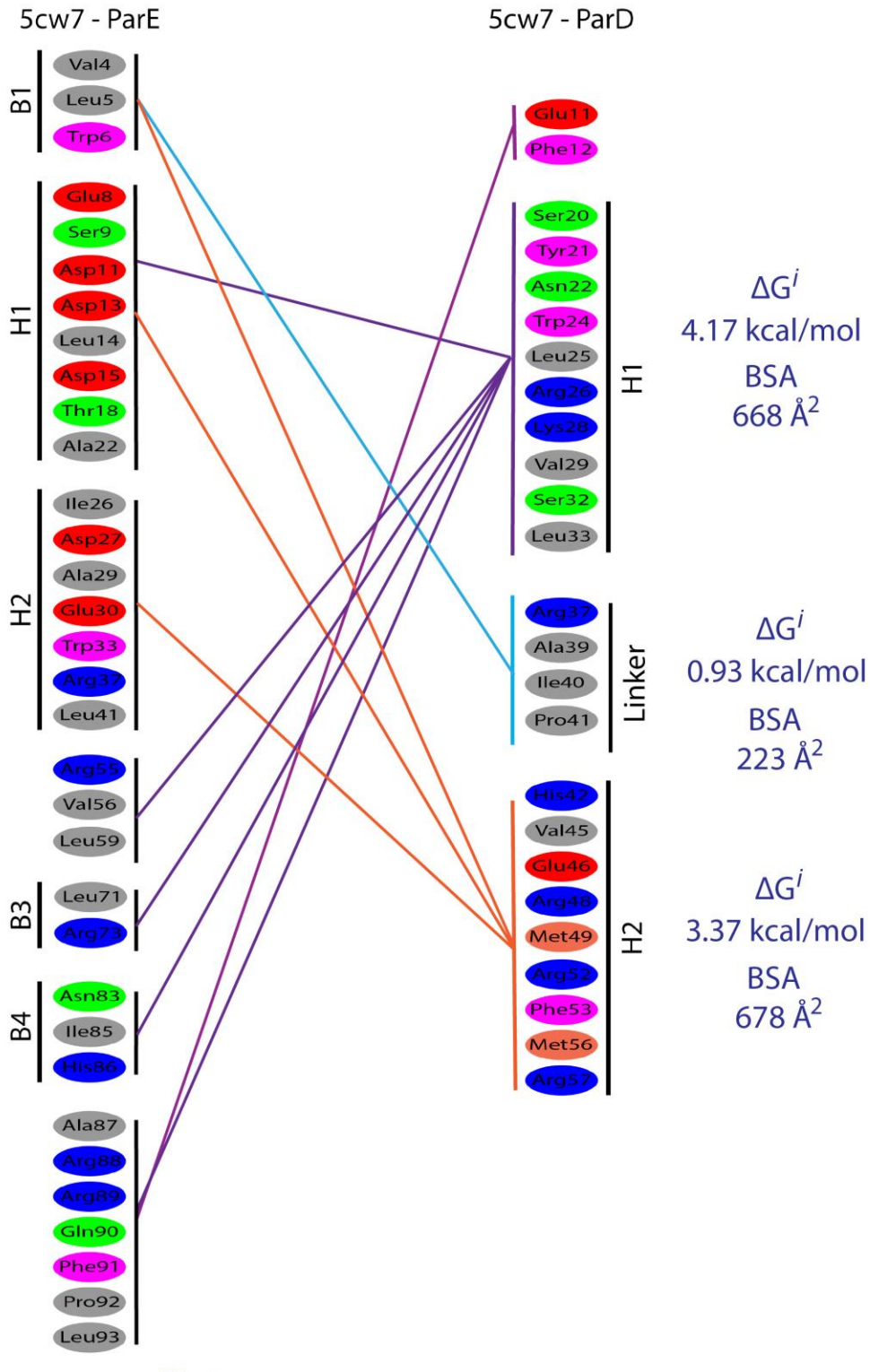
5cw7 - ParE
5cw7 - ParD
B1
Val4
Leu5
Trp6
H1
Glu8
Ser9
Asp11
Asp13
Leu14
Asp15
Thr18
Ala22
H2
Ile26
Asp27
Ala29
Glu30
Trp33
Arg37
Leu41
Arg55
Val56
Leu59
B3
Leu71
Arg73
B4
Asn83
Ile85
His86
Ala87
Arg88
Arg89
Gln90
Phe91
Pro92
Leu93
Glu11
Phe12
Ser20
Tyr21
Asn22
Trp24
Leu25
Arg26
Lys28
Val29
Ser32
Leu33
H1
Arg37
Ala39
Ile40
Pro41
Linker
His42
Val45
Glu46
Arg48
Met49
Arg52
Phe53
Met56
Arg57
H2
ΔG^i
4.17 kcal/mol
BSA
668 Å2
ΔG^i
0.93 kcal/mol
BSA
223 Å2
ΔG^i
3.37 kcal/mol
BSA
678 Å2

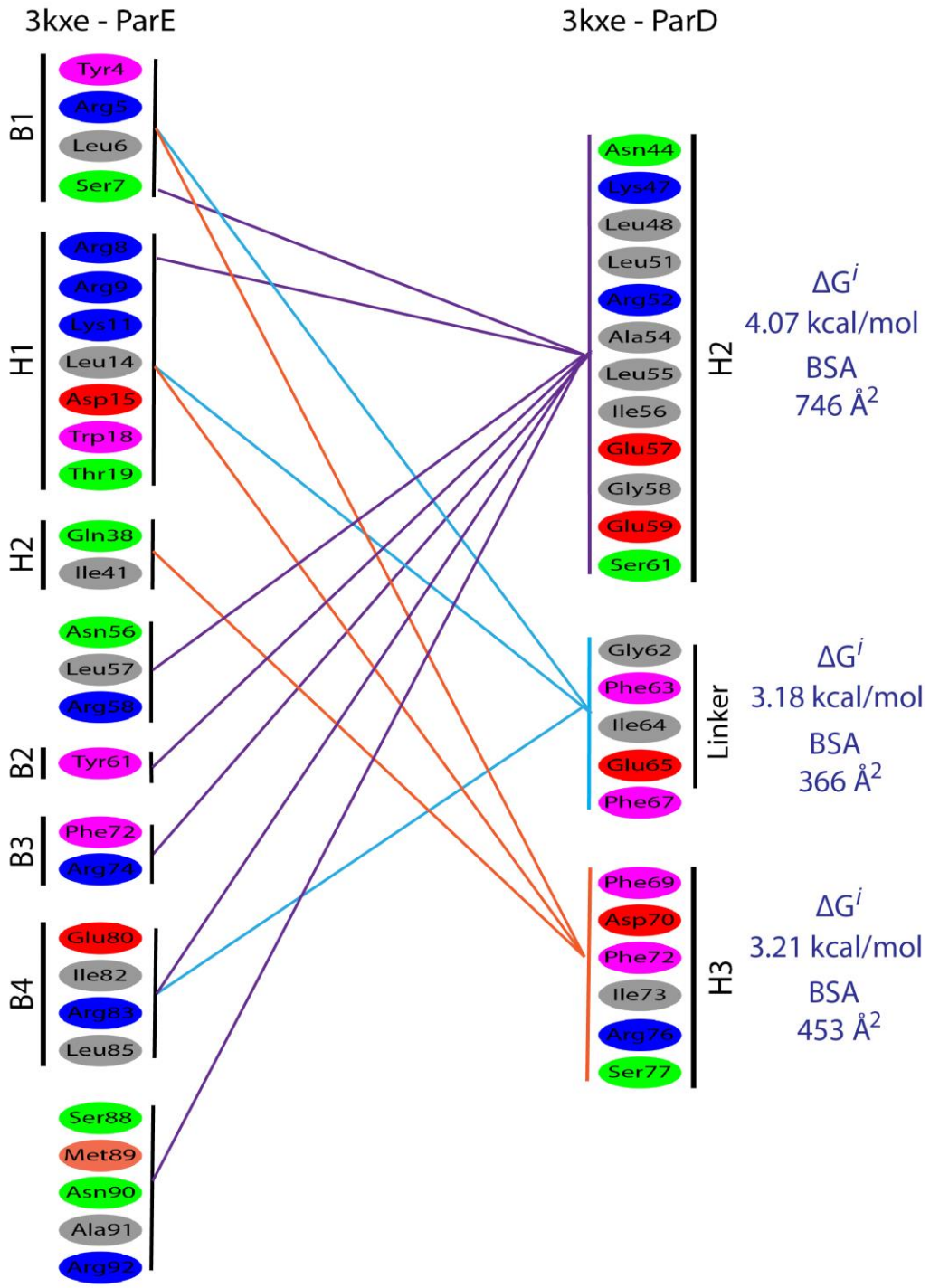
3kxe - ParE
3kxe - ParD
B1
Tyr4
Arg5
Leu6
Ser7
H1
Arg8
Arg9
Lys11
Leu14
Asp15
Trp18
Thr19
H2
Gln38
Ile41
B2
Asn56
Leu57
Arg58
B3
Tyr61
B4
Phe72
Arg74
Glu80
Ile82
Arg83
Leu85
Ser88
Met89
Asn90
Ala91
Arg92
H2
Asn44
Lys47
Leu48
Leu51
Arg52
Ala54
Leu55
Ile56
Glu57
Gly58
Glu59
Ser61
ΔG^i
4.07 kcal/mol
BSA
746 Å2
Linker
Gly62
Phe63
Ile64
Glu65
Phe67
ΔG^i
3.18 kcal/mol
BSA
366 Å2
H3
Phe69
Asp70
Phe72
Ile73
Arg76
Ser77
ΔG^i
3.21 kcal/mol
BSA
453 Å2

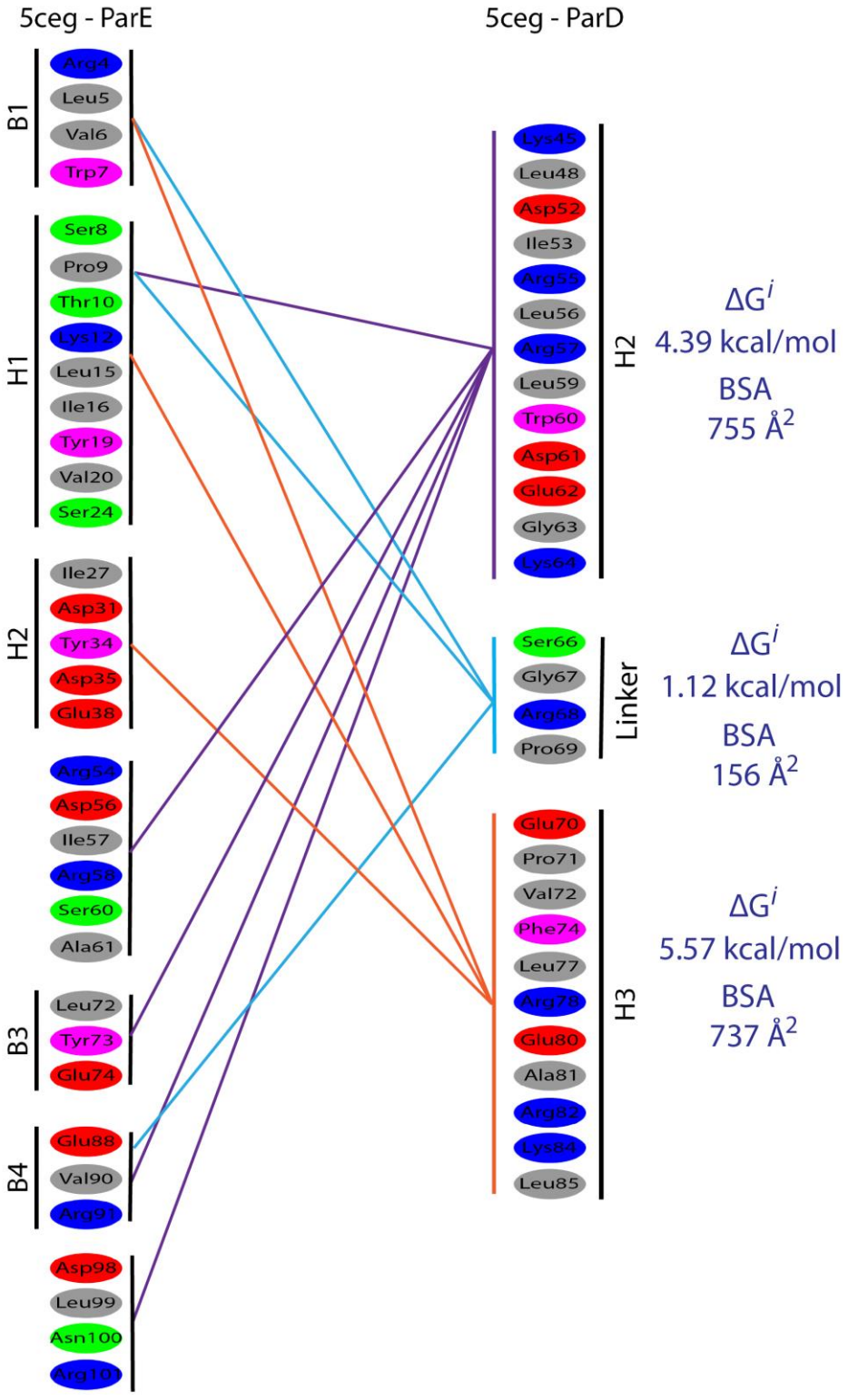
5ceg - ParE
5ceg - ParD
B1
Arg4
Leu5
Val6
Trp7
H1
Ser8
Pro9
Thr10
Lys12
Leu15
Ile16
Tyr19
Val20
Ser24
H2
Ile27
Asp31
Tyr34
Asp35
Glu38
Arg54
Asp56
Ile57
Arg58
Ser60
Ala61
B3
Leu72
Tyr73
Glu74
B4
Glu88
Val90
Arg91
Asp98
Leu99
Asn100
Arg101
Lys45
Leu48
Asp52
Ile53
Arg55
Leu56
Arg57
Leu59
Trp60
Asp61
Glu62
Gly63
Lys64
H2
ΔG^i
4.39 kcal/mol
BSA
755 Å2
Ser66
Gly67
Arg68
Pro69
Linker
ΔG^i
1.12 kcal/mol
BSA
156 Å2
Glu70
Pro71
Val72
Phe74
Leu77
Arg78
Glu80
Ala81
Arg82
Lys84
Leu85
H3
ΔG^i
5.57 kcal/mol
BSA
737 Å2

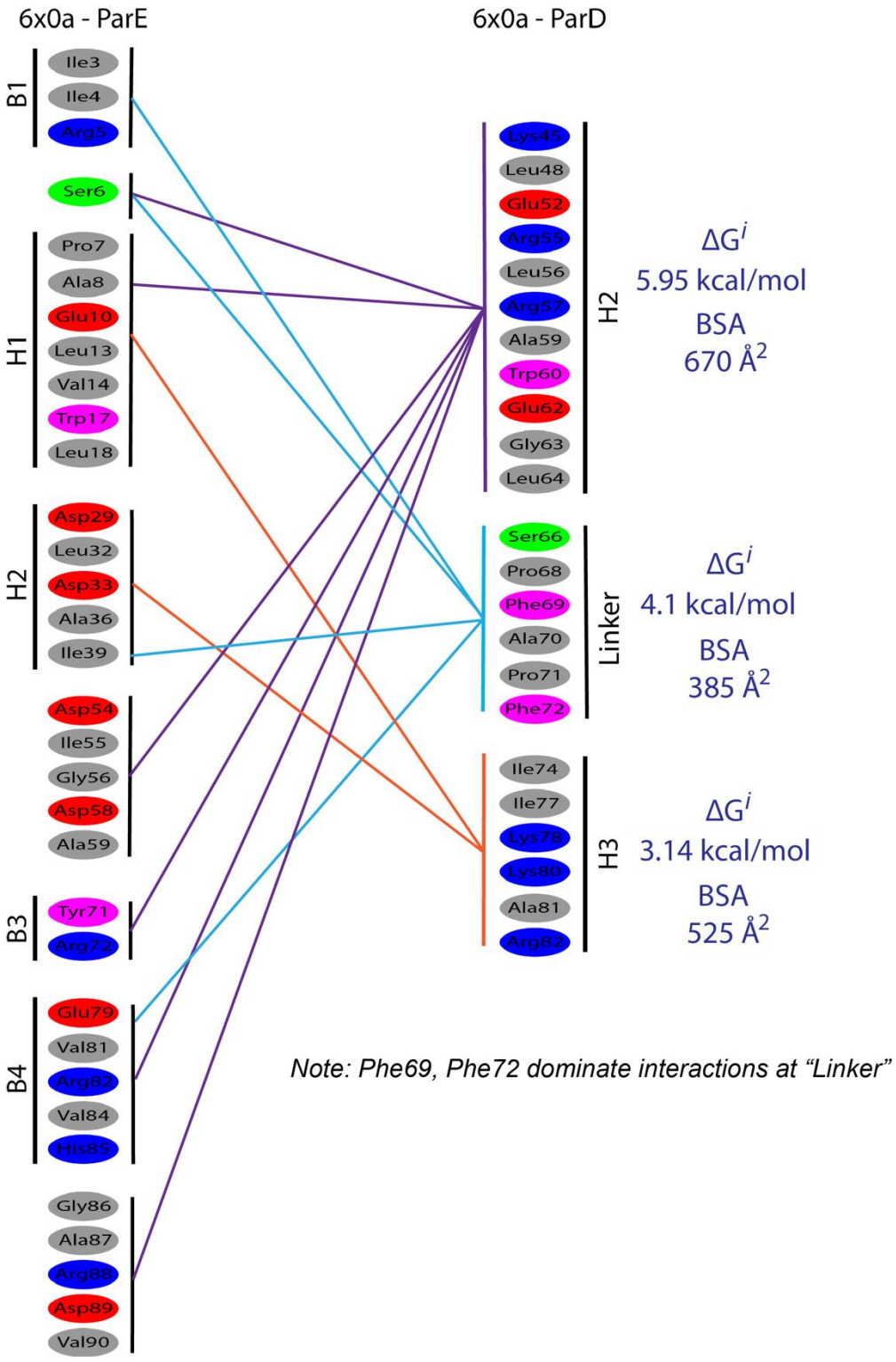
6x0a - ParE
6x0a - ParD
B1
Ile3
Ile4
Arg5
Ser6
H1
Pro7
Ala8
Glu10
Leu13
Val14
Trp17
Leu18
H2
Asp29
Leu32
Asp33
Ala36
Ile39
Asp54
Ile55
Gly56
Asp58
Ala59
B3
Tyr71
Arg72
B4
Glu79
Val81
Arg82
Val84
His85
Gly86
Ala87
Arg88
Asp89
Val90
Lys45
Leu48
Glu52
Arg55
Leu56
Arg57
Ala59
Trp60
Glu62
Gly63
Leu64
H2
ΔG^i
5.95 kcal/mol
BSA
670 Å2
Ser66
Pro68
Phe69
Ala70
Pro71
Phe72
Linker
ΔG^i
4.1 kcal/mol
BSA
385 Å2
Ile74
Ile77
Lys78
Lys80
Ala81
Arg82
H3
ΔG^i
3.14 kcal/mol
BSA
525 Å2
Note: Phe69, Phe72 dominate interactions at “Linker”

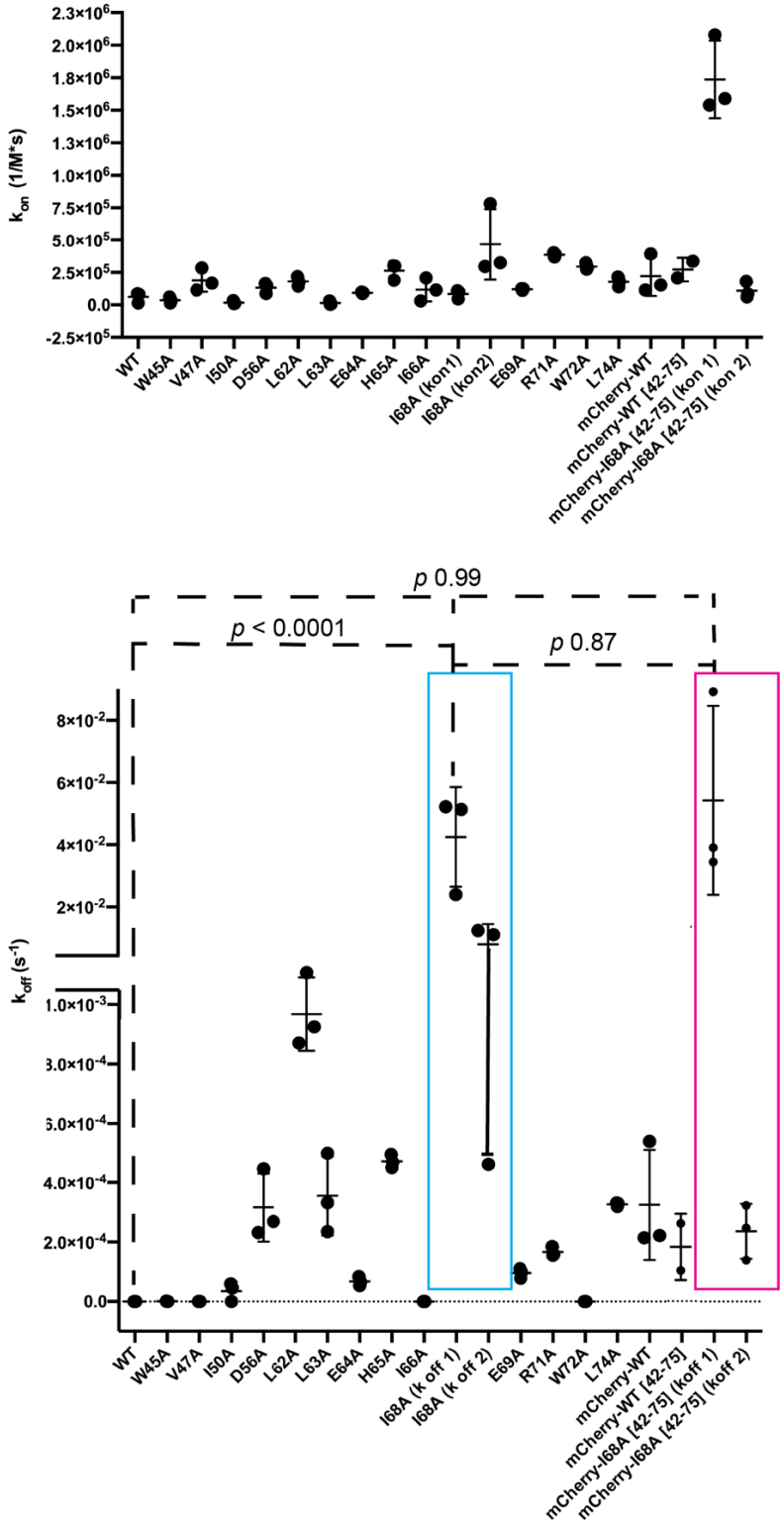

Figure S2.7. Kinetic rates of association and disassociation for wild type and mutant PaParD1 proteins. (Values given in Table S2.3, traces and individual measurements given in Fig. S2.1). Significance determined using a one-way ANOVA analysis.

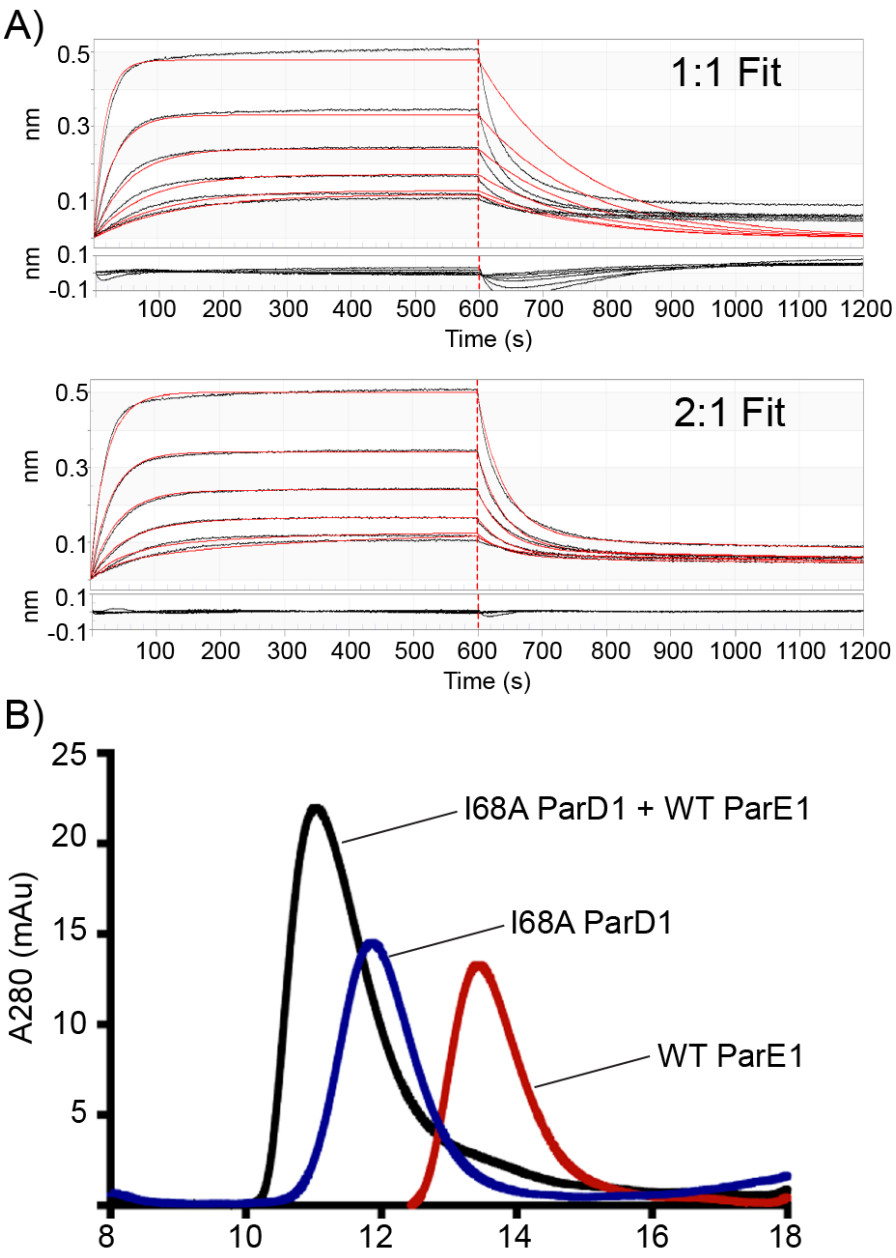

Figure S2.8. Analysis of I68A ParDE complex formation reveals a drastic change in complex interactions.
A. Comparison of fit for I68A BLI results. Comparison of residual fits indicates the I68A mutant does not impact the association rate of complex formation but causes two distinct dissociation events that cannot be fit by a 1:1 model. **B.** SEC analysis of I68A ParDE complex formation indicates a stable complex is formed between WT ParE1 and I68A ParD1.

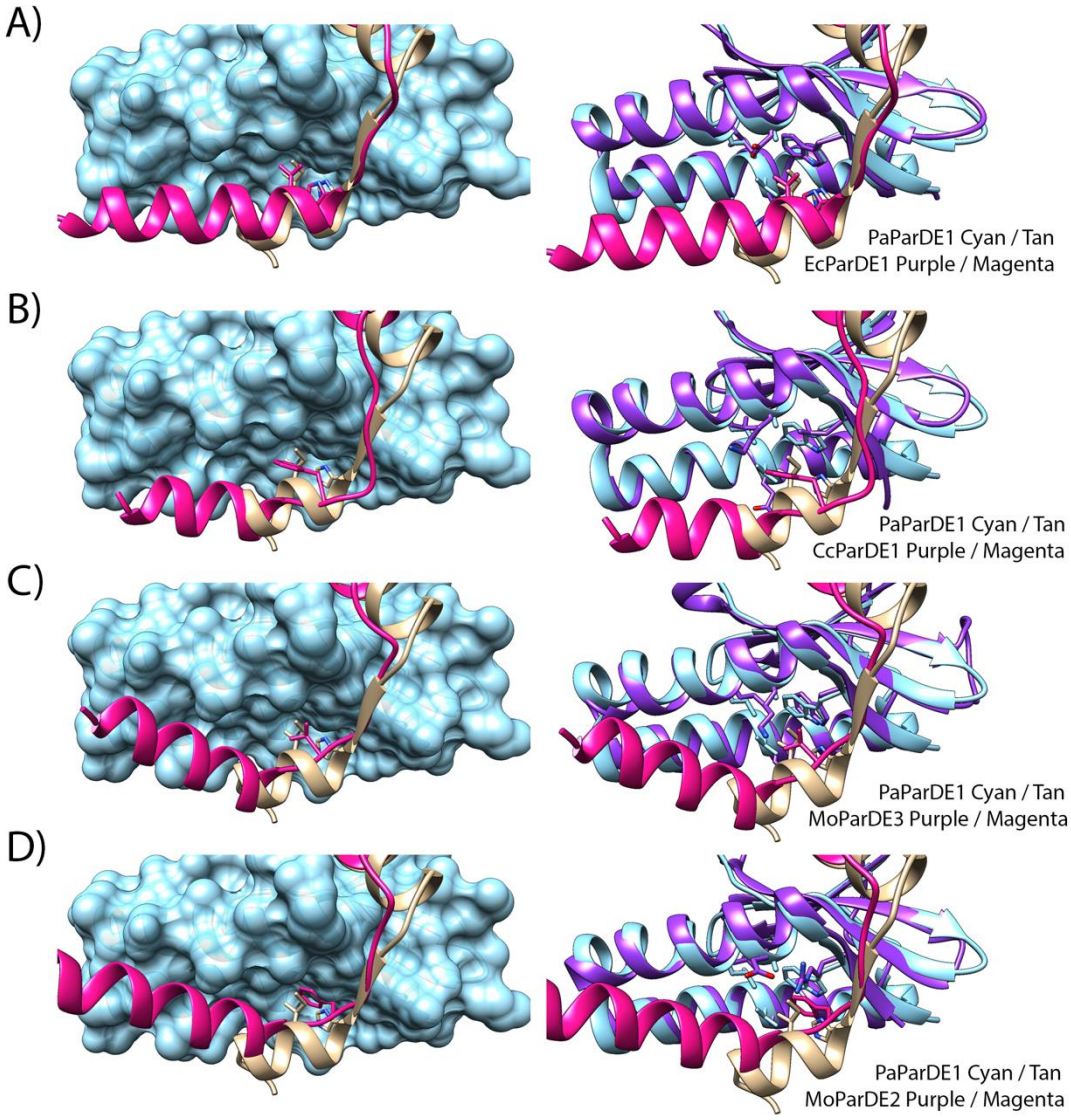

Figure S2.9. Structural comparison of ParDα3-ParE interfaces.
A. Left: Superposition of EcPaaA1 (5CZE, magenta) and PaParD1 (6XRW, tan) with PaParE1 surface (6XRW, cyan). Right: Superposition of EcParE2 (5CZE, purple) residues with PaParE1 (6XRW) residues in the PaParD1Ile68 binding pocket. **B.** Left: Superposition of CcParD1 (3KXE, magenta) and PaParD1 (6XRW, tan) with PaParE1 surface (6XRW, cyan). Right: Superposition of CcParE1 (3KXE, purple) residues with PaParE1 (6XRW) residues in the PaParD1Ile68 binding pocket. **C.** Left: Superposition of MoParD3 (5CEG, magenta) and PaParD1 (6XRW, tan) with PaParE1 surface (6XRW, cyan). Right: Superposition of MoParE3 (5CEG, purple) residues with PaParE1 (6XRW) residues in the PaParD1Ile68 binding pocket. **D.** Left: Superposition of MoParD2 (6X0A, magenta) and PaParD1 (6XRW, tan) with PaParE1 surface (6XRW, cyan). Right: Superposition of MoParE2 (6X0A, purple) residues with PaParE1 (6XRW) residues in the PaParD1Ile68 binding pocket.

Appendix B:

Chapter IV Supporting Information

Contents

Table S4.1 – Mutagenesis Primers for pET-15b::mCherry-PaParD1

mCh-ParD$_{42\text{-}75}$	**Fwd:** 5'-AGGCAGCAGTGGCAGGTC-3'
	Rev: 5'-TATCGATGAATTCGAGCTCGGTACC-3'
mCh-ParD$_{58\text{-}75}$	**Fwd:** 5'-AATGCCGGTCGCCTGCTG-3'
	Rev: 5'-TATCGATGAATTCGAGCTC-3'
mCh-ParD$_{62\text{-}75}$	**Fwd:** 5'-CTGCTGGAACACATCGAG-3'
	Rev: 5'-TATCGATGAATTCGAGCTCGGTACC-3'
mCh-ParD$_{65\text{-}75}$	**Fwd:** 5'-CACATCGAGATCGAGAAG-3'
	Rev: 5'-TATCGATGAATTCGAGCTC-3'

ParD1$_{58-75}$ (Ni-NTA Pin) + WT ParE1

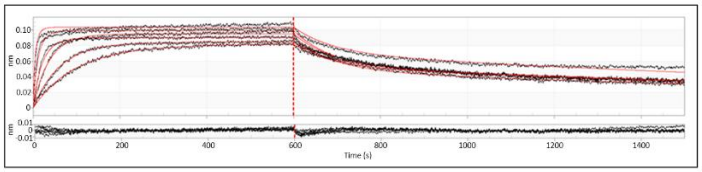

	Conc. (nM)	KD1 (M)	kon1 (1/Ms)	kdis1 (1/s)	Full R^2
Local Fit	100	2.73E-10	8.30E+05	2.27E-04	0.9910
	50	2.84E-08	5.57E+05	1.58E-02	0.9952
	25	1.33E-08	9.57E+05	1.27E-02	0.9965
	12.5	3.73E-10	1.63E+06	6.09E-04	0.9945
	6.25	6.23E-09	1.27E+06	7.90E-03	0.9962
	3.125	6.36E-09	1.38E+06	8.75E-03	0.9935
Global Fit		2.00E-10	2.45E+06	4.91E-04	0.9926

	Conc. (nM)	KD2 (M)	kon2 (1/Ms)	kdis2 (1/s)	Full R^2
Local Fit	100	2.34E-09	4.47E+06	1.04E-02	0.9910
	50	1.77E-10	3.49E+06	6.20E-04	0.9952
	25	2.32E-10	2.73E+06	6.34E-04	0.9965
	12.5	5.88E-09	2.38E+06	1.40E-02	0.9945
	6.25	2.10E-10	2.45E+06	5.13E-04	0.9962
	3.125	2.16E-10	2.62E+06	5.65E-04	0.9935
Global Fit		1.20E-08	9.39E+05	1.12E-02	0.9926

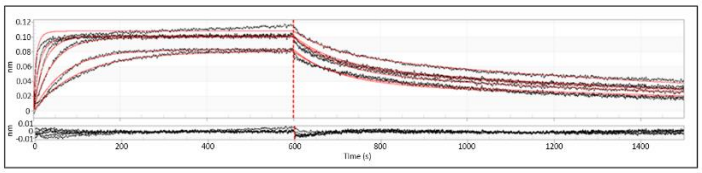

	Conc. (nM)	KD1 (M)	kon1 (1/Ms)	kdis1 (1/s)	Full R^2
Local Fit	100	1.37E-06	9.06E+03	1.24E-02	0.9931
	50	3.13E-08	5.46E+05	1.71E-02	0.9965
	25	4.19E-10	1.68E+06	7.05E-04	0.9975
	12.5	1.95E-08	7.44E+05	1.45E-02	0.9968
	6.25	1.96E-07	7.68E+04	1.50E-02	0.9954
	3.125	1.54E-07	9.35E+04	1.44E-02	0.9940
Global Fit		4.03E-10	1.98E+06	7.99E-04	0.9935

	Conc. (nM)	KD2 (M)	kon2 (1/Ms)	kdis2 (1/s)	Full R^2
Local Fit	100	3.48E-10	2.30E+06	7.98E-04	0.9931
	50	5.11E-10	2.06E+06	1.05E-03	0.9965
	25	8.81E-09	1.27E+06	1.12E-02	0.9975
	12.5	4.64E-10	1.84E+06	8.51E-04	0.9968
	6.25	7.61E-10	1.74E+06	1.33E-03	0.9954
	3.125	6.65E-10	1.90E+06	1.26E-03	0.9940
Global Fit		1.54E-08	6.93E+05	1.07E-02	0.9935

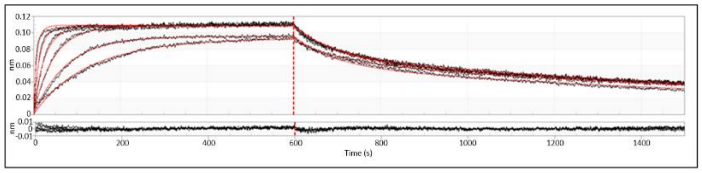

	Conc. (nM)	KD1 (M)	kon1 (1/Ms)	kdis1 (1/s)	Full R^2
Local Fit	100	6.87E-10	9.22E+05	6.33E-04	0.9964
	50	3.08E-10	2.09E+06	6.46E-04	0.9967
	25	4.96E-10	1.34E+06	6.62E-04	0.9976
	12.5	4.67E-10	1.63E+06	7.60E-04	0.9975
	6.25	1.23E-07	1.05E+05	1.29E-02	0.9976
	3.125	9.29E-09	1.06E+06	9.84E-03	0.9943
Global Fit		3.89E-10	1.82E+06	7.07E-04	0.9966

	Conc. (nM)	KD2 (M)	kon2 (1/Ms)	kdis2 (1/s)	Full R^2
Local Fit	100	3.51E-09	2.90E+06	1.02E-02	0.9964
	50	1.99E-08	5.94E+05	1.18E-02	0.9967
	25	5.30E-09	1.76E+06	9.35E-03	0.9976
	12.5	1.09E-08	1.17E+06	1.27E-02	0.9975
	6.25	4.86E-10	1.86E+06	9.05E-04	0.9976
	3.125	4.05E-10	1.65E+06	6.70E-04	0.9943
Global Fit		1.52E-08	7.12E+05	1.08E-02	0.9966

Figure S4.1. Replicates of Biolayer Interferometry assays with corresponding residual error of fits and calculated values. (Additional traces on the following page).

ParD1$_{62\text{-}75}$ (Ni-NTA Pin) + WT ParE1

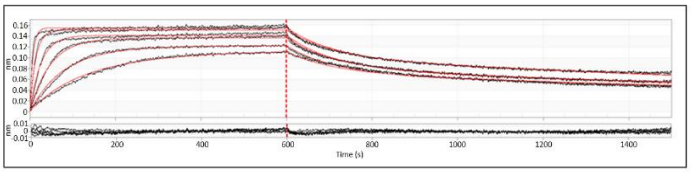

	Conc. (nM)	KD1 (M)	kon1 (1/Ms)	kdis1 (1/s)	Full R^2
Local Fit	100	3.42E-10	1.16E+06	3.97E-04	0.9966
	50	1.70E-10	2.20E+06	3.75E-04	0.9963
	25	4.34E-10	1.26E+06	5.49E-04	0.9959
	12.5	9.34E-09	1.06E+06	9.93E-03	0.9967
	6.25	3.76E-08	2.76E+05	1.04E-02	0.9972
	3.125	3.41E-08	1.89E+05	6.43E-03	0.9965
Global Fit		2.83E-10	1.58E+06	4.47E-04	0.9959

	Conc. (nM)	KD2 (M)	kon2 (1/Ms)	kdis2 (1/s)	Full R^2
Local Fit	100	3.40E-09	2.97E+06	1.01E-02	0.9966
	50	1.42E-08	6.75E+05	9.59E-03	0.9963
	25	7.27E-09	1.56E+06	1.13E-02	0.9959
	12.5	2.99E-10	1.62E+06	4.86E-04	0.9967
	6.25	3.59E-10	1.84E+06	6.58E-04	0.9972
	3.125	2.29E-10	1.99E+06	4.55E-04	0.9965
Global Fit		8.26E-09	1.10E+06	9.12E-03	0.9959

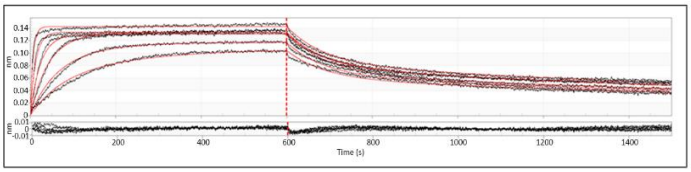

	Conc. (nM)	KD1 (M)	kon1 (1/Ms)	kdis1 (1/s)	Full R^2
Local Fit	100	4.16E-10	1.06E+06	4.41E-04	0.9963
	50	1.45E-08	9.54E+05	1.38E-02	0.9971
	25	1.01E-08	1.31E+06	1.33E-02	0.9974
	12.5	8.06E-09	1.47E+06	1.18E-02	0.9968
	6.25	8.84E-08	1.38E+05	1.22E-02	0.9976
	3.125	1.35E-07	7.98E+04	1.08E-02	0.9945
Global Fit		3.42E-10	1.53E+06	5.23E-04	0.9952

	Conc. (nM)	KD2 (M)	kon2 (1/Ms)	kdis2 (1/s)	Full R^2
Local Fit	100	3.80E-09	2.99E+06	1.14E-02	0.9963
	50	2.72E-10	2.39E+06	6.52E-04	0.9971
	25	2.10E-10	1.83E+06	3.84E-04	0.9974
	12.5	3.69E-10	1.42E+06	5.25E-04	0.9968
	6.25	4.17E-10	1.86E+06	7.75E-04	0.9976
	3.125	3.57E-10	1.95E+06	6.95E-04	0.9945
Global Fit		8.12E-09	1.40E+06	1.14E-02	0.9952

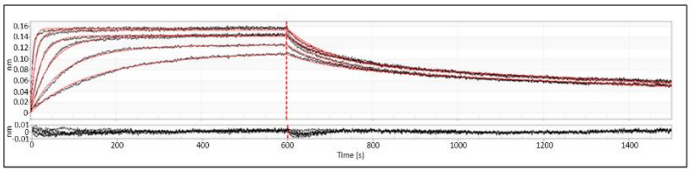

	Conc. (nM)	KD1 (M)	kon1 (1/Ms)	kdis1 (1/s)	Full R^2
Local Fit	100	4.96E-10	1.19E+06	1.14E-02	0.9977
	50	5.32E-10	1.21E+06	1.37E-02	0.9968
	25	4.81E-10	1.40E+06	1.23E-02	0.9975
	12.5	3.23E-10	1.57E+06	9.87E-03	0.9972
	6.25	2.75E-08	3.59E+05	5.46E-04	0.9974
	3.125	4.87E-09	1.15E+06	3.45E-04	0.9962
Global Fit		4.03E-10	1.45E+06	5.82E-04	0.9970

	Conc. (nM)	KD2 (M)	kon2 (1/Ms)	kdis2 (1/s)	Full R^2
Local Fit	100	3.80E-09	3.01E+06	1.14E-02	0.9977
	50	6.38E-09	2.15E+06	1.37E-02	0.9968
	25	8.36E-09	1.47E+06	1.23E-02	0.9975
	12.5	7.00E-09	1.41E+06	9.87E-03	0.9972
	6.25	2.95E-10	1.85E+06	5.46E-04	0.9974
	3.125	2.44E-10	1.41E+06	3.45E-04	0.9962
Global Fit		7.48E-09	1.47E+06	1.10E-02	0.9970

Fig. S4.1 (continued)

mCh-WT ParD1$_{42-75}$ (Ni-NTA Pin) + WT ParE1

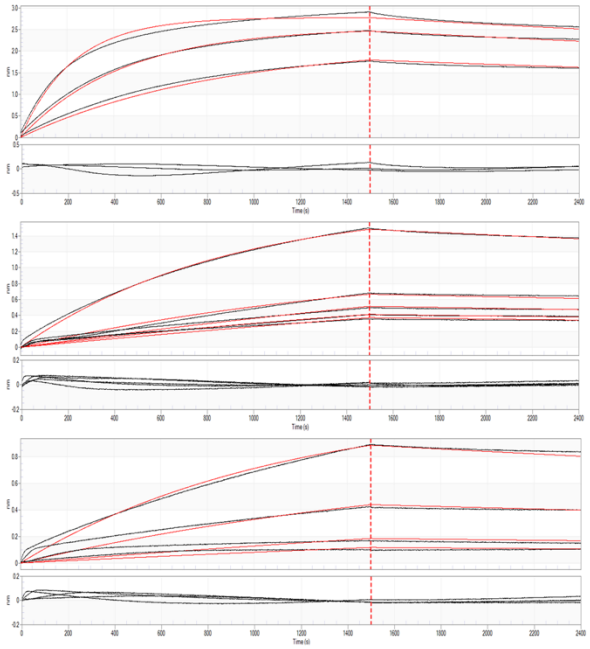

	Conc. (nM)	KD (M)	kon(1/Ms)	kdis(1/s)	Full R^2
Local Fit	10	2.64E-10	3.87E+05	1.02E-04	0.9856
	5	1.66E-10	4.78E+05	7.93E-05	0.9979
	2.5	1.75E-10	6.13E+05	1.07E-04	0.9994
Global Fit		2.56E-10	4.34E+05	1.11E-04	0.9924

	Conc. (nM)	KD (M)	kon(1/Ms)	kdis(1/s)	Full R^2
Local Fit	10	7.78E-10	1.11E+05	8.62E-05	0.9976
	5	<1.0E-12	1.14E+05	<1.0E-07	0.993
	2.5	<1.0E-12	2.96E+05	<1.0E-07	0.9894
	1.25	<1.0E-12	7.54E+05	<1.0E-07	0.9813
	0.625	3.11E-12	1.78E+06	5.55E-06	0.9831
Global Fit		8.77E-10	1.06E+05	9.29E-05	0.9959

	Conc. (nM)	KD (M)	kon(1/Ms)	kdis(1/s)	Full R^2
Local Fit	10	6.01E-10	8.47E+04	5.09E-05	0.9928
	5	1.92E-11	2.85E+05	5.48E-06	0.9645
	0.625	1.40E-11	4.86E+06	6.81E-05	0.9812
	0.3125	<1.0E-12	8.72E+06	<1.0E-07	0.9855
Global Fit		1.35E-09	8.02E+04	1.09E-04	0.9882

Fig. S4.1 (continued) *Note – previously published in Snead, K. J., Moore, L. L., and Bourne, C. R. (2022) ParD Antitoxin Hotspot Alters a Disorder-to-Order Transition upon Binding to Its Cognate ParE Toxin, Lessening Its Interaction Affinity and Increasing Its Protease Degradation Kinetics. Biochemistry 61, 34-45

mCh-WT ParD1 (Ni-NTA Pin) + WT ParE1

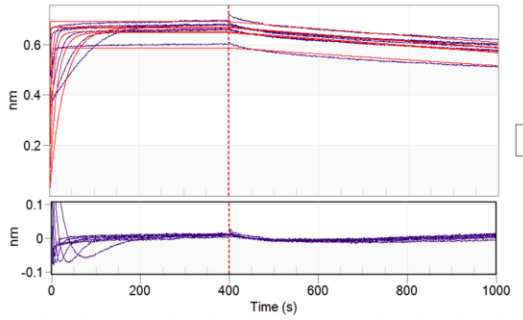

Conc. (nM)	KD (M)	kon(1/Ms)	kdis(1/s)	Full R^2
Global Fit	5.47E-11	3.93E+06	2.15E-04	0.8257

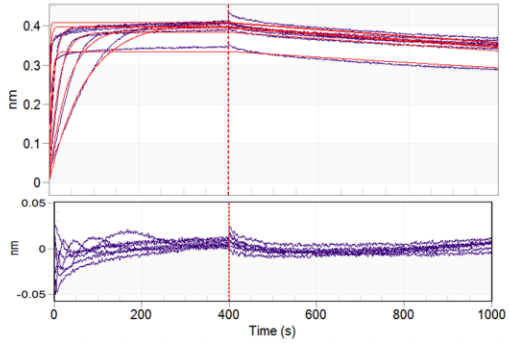

Conc. (nM)	KD (M)	kon(1/Ms)	kdis(1/s)	Full R^2
Global Fit	1.46E-10	1.53E+06	2.22E-04	0.9766

Fig. S4.1 (continued) *Note – previously published in Snead, K. J., Moore, L. L., and Bourne, C. R. (2022) ParD Antitoxin Hotspot Alters a Disorder-to-Order Transition upon Binding to Its Cognate ParE Toxin, Lessening Its Interaction Affinity and Increasing Its Protease Degradation Kinetics. Biochemistry 61, 34-45

mCherry (Ni-NTA) + WT ParE1

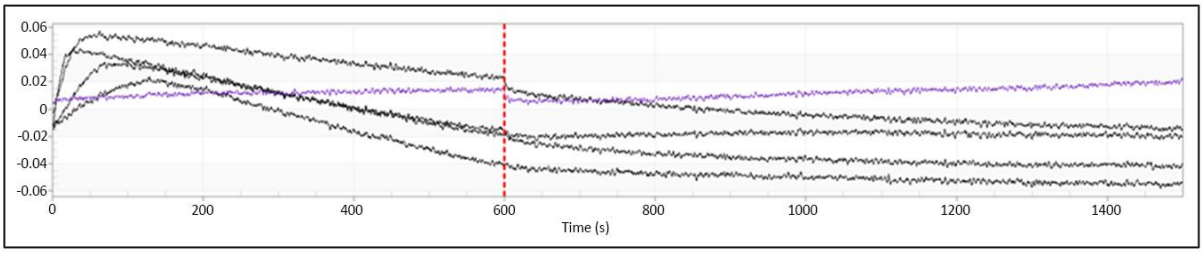

Fig. S4.1 (continued)

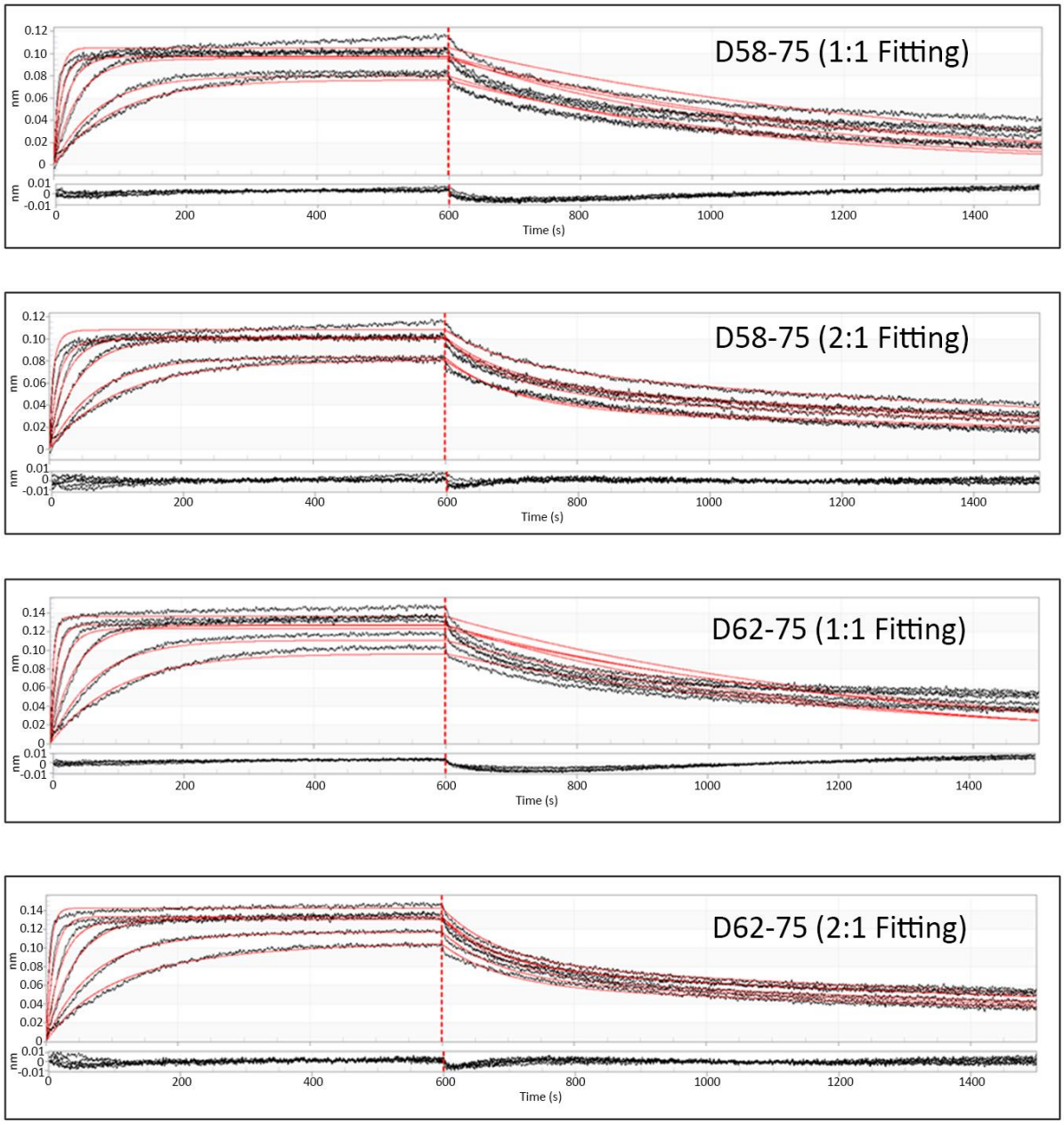

Figure S4.2. Comparison of BLI fitting results for ParD$_{peptides}$. Comparison of fitting results 1:1 vs. 2:1 for ParD$_{58-75}$ and ParD$_{62-75}$.

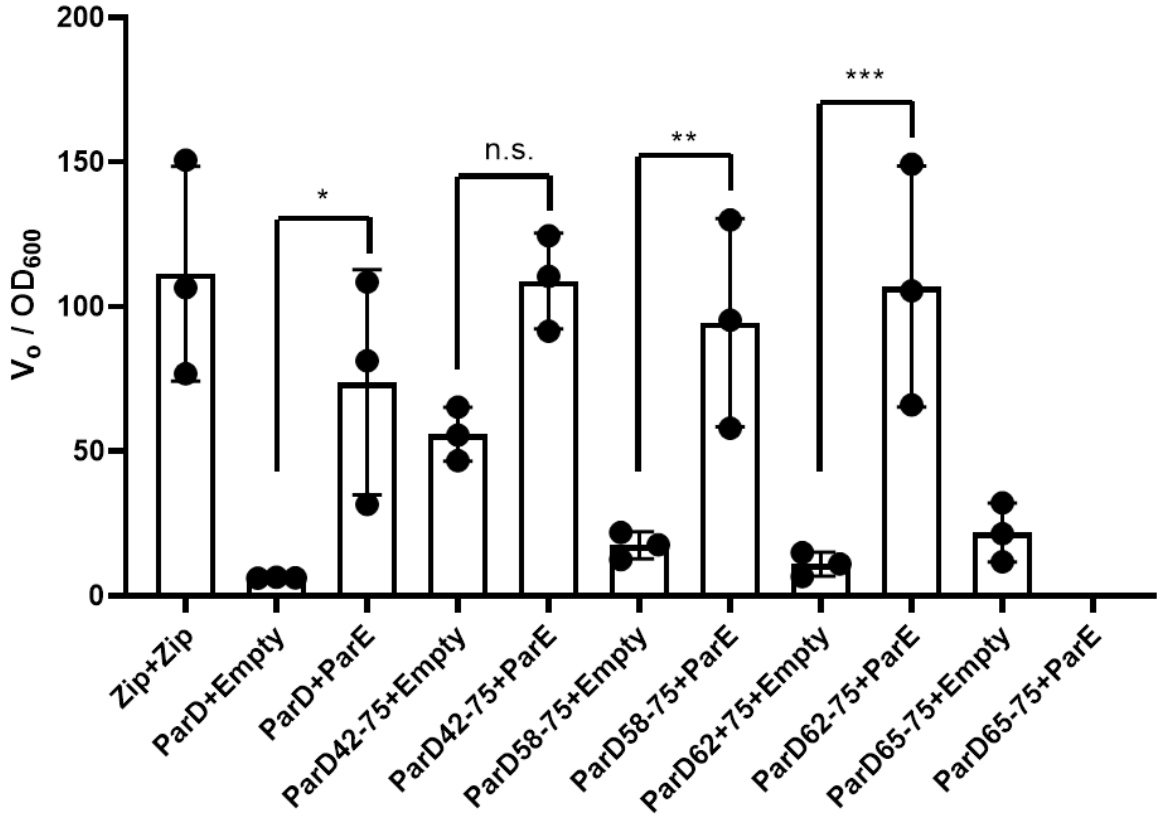

Figure S4.3. Biological Replicates of Kinetic Miller Assay. Additional biological replicate of kinetic miller assay (Fig 4.1). * denotes p-value ≤ 0.05, ** denotes p-value ≤ 0.01, *** denotes p-value ≤ 0.001. (additional biological replicate below)

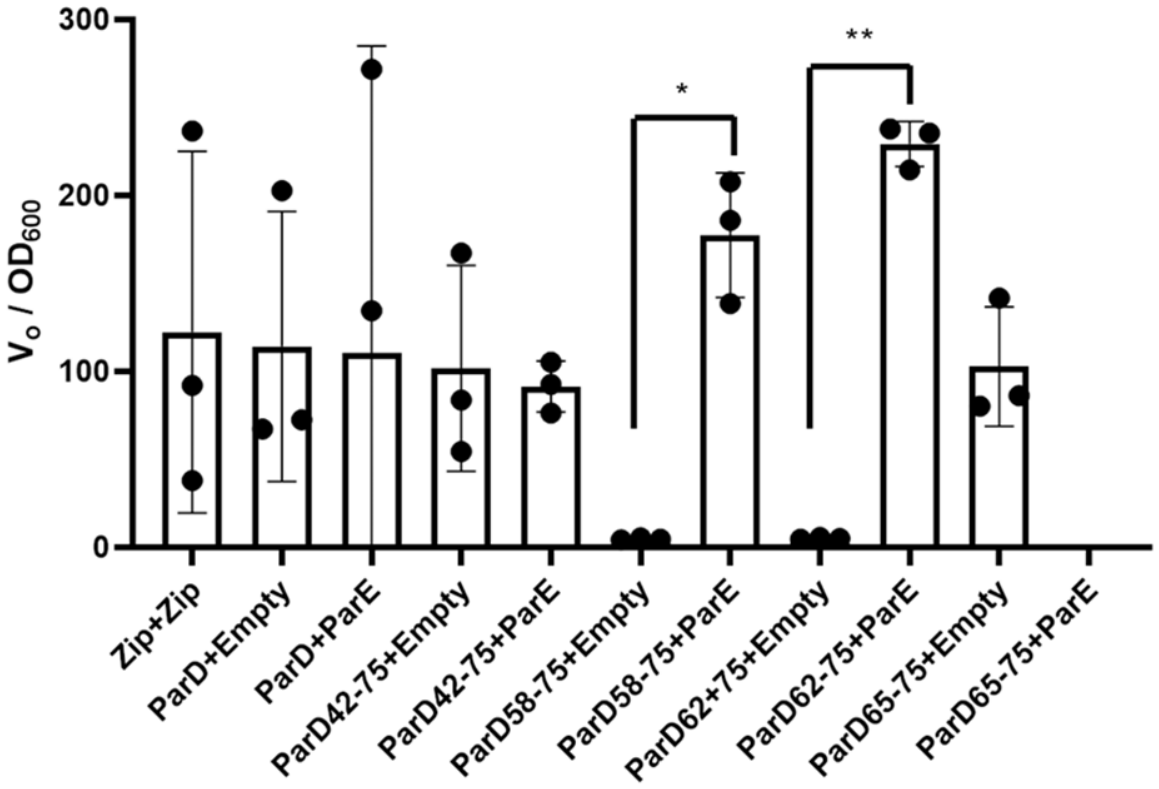

Fig. S4.3 (continued)